87

An X-Ray Spectrocopic Study of the SMC X-1/Sk 160 X-Ray Binary System

by

Patrick Stephen Wojdowski

A.B. Physics, University of California, Berkeley (1993)

Submitted to the Department of Physics
in partial fulfillment of the requirements for the degree of

Doctor of Philosophy

at the

MASSACHUSETTS INSTITUTE OF TECHNOLOGY

February 1999

Author .....
Department of Physics
November 19, 1998

Certified by .....
George W. Clark
Professor Emeritus
Thesis Supervisor

Accepted by .....
Thomas J. Greytak
Associate Department Head for Education

An X-Ray Spectrocopic Study of the SMC X-1/Sk 160 X-Ray Binary System

by

Patrick Stephen Wojdowski

Submitted to the Department of Physics
on November 19, 1998, in partial fulfillment of the
requirements for the degree of
Doctor of Philosophy

Abstract

In this thesis, the properties of the circumstellar environment of the high-mass X-ray binary system SMC X-1/Sk 160 are explored using observational data from several satellite X-ray observatories. First, we have investigated the cause of the quasi-periodic $\sim$ 60 day high-state low-state X-ray flux variation, previously suggested, and now clearly evident in extensive *BATSE* and *RXTE* monitoring data. Data from short-term pointed observations with the *Ginga*, *ROSAT*, *ASCA*, and *RXTE* observatories, show that while the uneclipsed flux varies by as much as a factor of 20 between high and low states, the eclipsed flux consists of approximately the same flux of reprocessed radiation in both states. From this we conclude that the high-low cycle is due to a quasi-periodic occultation of the source, most likely by a precessing tilted accretion disk around the neutron star.

Next, we investigate the composition and distribution of the wind of Sk 160, the supergiant companion of the X-ray star SMC X-1, by comparing an X-ray spectrum of the source, obtained with the *ASCA* observatory during an eclipse with the computed spectra of reprocessed radiation from circumstellar matter with various density distributions. We show that the metal abundance in the wind of SMC X-1 is no greater than a few tenths of solar, as has been determined for other objects in the Magellanic Clouds. We also show that the observed spectrum is not consistent with the density distributions of circumstellar matter of the spherically symmetric form derived for line-driven winds, nor the density distribution from a hydrodynamic simulation of the X-ray perturbed and line-driven wind by Blondin & Woo (1995). Essential properties of a density distribution that would yield aagreement with the observed spectrum are defined. Finally, we discuss prospects for futrure studies of this kind based on high-resolution spectroscopy data expected from the AXAF mission.

Thesis Supervisor: George W. Clark
Title: Professor Emeritus

ACKNOWLEDGMENTS

A great deal of credit for this thesis belongs to Tim Kallman of NASA/Goddard Space Flight Center, my technical advisor for the NASA Graduate Student Researchers Program. His knowledge and intuition in the field of X-ray photoionized plasmas was central to my original exploration of this project. I am further indebted to Tim for making modifications to his XSTAR spectral simulation program and for inviting me to spend January of 1998 working at Goddard, where I wrote the code for my spectral simulation program with his guidance.

I owe thanks to several other individuals at NASA/Goddard Space Flight Center. James Peachey provided me with critical assistance in programming. I owe a very large debt of gratitude to Keith Gendreau for his hospitality in opening his house to me during my month at Goddard. Many individuals deserve thanks for answering my questions about data reduction and analysis through the email help lines; Keith Arnaud deserves special mention in this regard.

I would like to thank my collaborators in the work regarding quasi-periodic occultation by a precessing accretion disk: Nan Zhang, Jonathan Woo, and Al Levine. Al Levine, in particular, contributed many useful ideas and had many discussions with me on that topic, and that work would have suffered greatly without his collaboration.

My advisor, Professor George Clark, has been a constant source of support and encouragement since my first year at the Massachusetts Institute of Technology and I have benefited much from being able to walk into his office and discuss science at any time. Although I often bemoaned George's constant advice to look at things more closely and to do things more meticulously, this advice stands as one of the most important lessons of my graduate study.

I owe great thanks to many of my fellow astrophysics graduate students at MIT for their friendship and support, as well as for the countless times I came to them with questions on computer programming, general computer trivia, data reduction, and analysis. My labmates Derek Fox, Jeff Kommers, and Bob Rutledge deserve particular thanks in all of these regards, as does Mike Pivovaroff, for helping me

understand the operation of the *ASCA* X-ray CCDs.

In addition, I am grateful for the support of many people outside of the Center for Space Research, and especially Mike Bradley, Robin Dennis, and Robb Wolfson. And, of course, without the love and support of my family I don't know how I could have gotten to the point where I started this thesis, much less finished it.

This research has made use of data obtained through the High Energy Astrophysics Science Archive Research Center Online Service, provided by the NASA/Goddard Space Flight Center.

To the memory of

Kevin Michael Slattery

Contents

List of Figures

List of Tables

Chapter 1

Introduction

The evidence that some of the first discovered cosmic X-ray sources were components of binary star systems included periodic variations of Doppler shifts of X-ray pulsar periods and periodic "low-states" which were recognized as eclipses by a companion star. Observations of Cen X-3 with *Uhuru* showed that the X-ray source pulsed with a 4.8 second period (Giacconi et al. 1971), that the pulse period varied sinusoidally with a 2.087 day period as it would for a body in a circular orbit, and that periodic X-ray "low-states" occurred at opposition of the Doppler delay orbit (Schreier et al. 1972). It was firmly established that this source is a magnetized neutron star in an eclipsing binary system with a massive B0-type star. Schreier et al. (1972) noticed, however, that during the X-ray eclipses, the X-ray flux from the system did not disappear and that an "additional source of X-rays must be postulated to exist" and speculated that the residual flux might be "the slow radiative cooling of the gas surrounding the system which is heated by the pulsating source". In observations with the GSFC Cosmic X-ray Spectroscopy experiment on board *OSO-8*, Becker et al. (1978) detected a significant flux of residual X-rays during three eclipses of the massive X-ray binary Vela X-1 and argued – on the grounds that the residual eclipse had, within limits, the same spectrum as the uneclipsed flux – that this eclipse flux was most likely due to X-ray scattering around the primary star. In addition to the periodic eclipse variations, some X-ray binaries were seen to vary on longer time scales. The X-ray flux from Her X-1, which has an orbital period of 1.7 days, also varies with a

period of 35 days. This flux variation has also been interpreted as occultation of the compact X-ray source but by a precessing accretion disk around that X-ray source (Priedhorsky & Holt 1987 and references therein). The residual flux seen during these types of occultations must also be due to reprocessing in the stellar wind.

Stellar winds driven by radiation pressure are a ubiquitous feature of massive stars which are the typical companions of pulsars in high mass X-ray binaries (HMXBs). Extensive theoretical work has been done on the ionization of these winds by the X-ray sources in them (Hatchett & McCray 1977 and references therein). Work was directed at explaining the variation with orbital phase of the X-ray absorption of the direct radiation from the compact object (e.g. Hatchett & McCray 1977) and the optical light variations (e.g. Pringle 1973). Hatchett, Buff, and McCray (1976) had made predictions of the spectra of X-ray photoionized plasmas. However, little, if any, work was directed at how, or if, reprocessing in the photoionized plasma could explain the residual eclipse flux seen in some of these eclipsing X-ray binaries.

The detectors of the early days of X-ray astronomy had very poor spectral resolution and were therefore insensitive to many of the effects of ionization, which may have been the reason for the lack of theoretical work in this area. For example, observations of Vela X-1 with *Tenma* (Sato et al. 1986) showed that a 6.4 keV Kα fluorescent line of iron, prominent in the uneclipsed spectrum, decreased in absolute intensity, but increased in relative intensity compared to the continuum in the eclipsed spectrum. The authors were able to explain the orbital phase variation of the iron line and the continuum by Thompson scattering and fluorescent line emission from neutral material of solar abundances in the stellar wind, atmosphere, and a small, dense region near the neutron star. Lewis, et al. (1992) studied the *Ginga* data of Vela X-1 over an entire orbit and found that ionization in the stellar wind would not have had an observable effect on that data.

A watershed development in X-ray astronomy occurred with the launch of the *ASCA* observatory in 1993. With its Solid-State Imaging Spectrometers (SIS), X-ray spectra of could be measured with moderately high resolution ($E/\Delta E \sim 15$ at 1 keV) over the entire 0.5–10 keV band simultaneously In an observation of Vela X-1 with

ASCA, approximately 10 emission features emerged in the spectrum of the system viewed during eclipse of the X-ray source when the much more intense, spectrally featureless radiation was occulted. Most of these features were identified as Kα emission lines from He-like ions of astrophysically abundant metals (Nagase et al. 1994). This observation, as well as other observations of X-ray binaries with *ASCA* demonstrated that ionization is very important to the understanding of high-spectral resolution X-ray observations of X-ray binaries.

In this thesis, long-term monitoring data from the all-sky monitor (ASM) on the *Rossi X-ray Timing Explorer* and the Burst and Transient Source Experiment on the Compton Gamma-Ray Observatory (CGRO) that confirm a previously suggested (Zhang et al. 1996; Levine et al. 1996) $\sim$ 60 day cyclic variability of the X-ray flux from SMC X-1. An analysis of the X-ray light curves and spectra derived from various pointed-mode observations by the *ASCA*, *ROSAT*, *Ginga*, and *RXTE* observatories is made to determine the cause of the cyclic variability.

The high resolution spectrum from *ASCA* of SMC X-1 in eclipse is compared to computed spectra of reprocessed radiation from gas at different levels of ionization. A procedure to simulate the spectrum of reprocessed radiation for a given point source of X-radiation and a given three-dimensional gas distribution is devised. This procedure allows one to combine and compare some of the results from the large body of work on stellar winds and photoionized plasmas with observational X-ray spectral data of X-ray binaries which undergo eclipses by their companions or other structures. This procedure is applied to test a model of the stellar wind from a hydrodynamic simulation by Blondin & Woo (1995). Given the known luminosity and spectrum of X-rays from the neutron star, it is found that the matter distribution from a hydrodynamic simulation of the system by Blondin & Woo (1995) would produce a large flux of recombination emission in the *ASCA* band below $\sim$1 keV which is not observed in the eclipse spectrum. The spectral simulation procedure should be useful in analysis of the data from high-resolution X-ray spectroscopy of X-ray binaries which has begun to emerge since the launch of *ASCA* in 1993 and will grow enormously with the launches of the *AXAF*, *XMM*, and *ASTRO-E* observatories all scheduled before

the end of the year 2000.

Chapter 2

Radiatively Driven Stellar Winds in Massive Stars and HMXBs

Rocket observations of the ultra-violet spectra of three massive early-type stars in Orion by Morton (1967) showed that strong winds are a ubiquitous feature of O and B-type giants and supergiants. The evidence for these winds lies in the so-called "P-Cygni" profiles of the UV resonance lines. Named after the star in which they were first observed, P-Cygni profiles are characterized by absorption to the blue and emission to the red of the line center. They are caused by absorption of stellar light by the wind in front of the star which flows towards the observer and emission from the limbs of the wind which moves transversely to the line of sight. Wind velocities can be derived from the widths of these P-Cygni profiles, and column densities can be derived from the equivalent widths. From these two quantities, one can be derived estimates on the mass loss rates of stars. Morton (1967) found that O & B type stars have wind velocities of order 1000 km/s and mass loss rates of order $10^{-6} M_{\odot}$/year.

To drive winds of such magnitude, strong radial forces are required. Castor, Abbott, and Klein (1975) developed the theory of line-driven winds with calculations that included thousands of transitions in the ionized atoms which make up the wind. In this theory, many lines are deplete the stellar radiation near their rest frame wavelengths in the slow moving material near the stellar surface. However, farther from the star, the wind is at higher velocities and therefore absorbs stellar continuum

photons to the blue of the rest frame wavelength and the lines continue to contribute to the acceleration of the wind. Using a force law derived from a fit to the sum of the many lines, they solved the equations of motion for an expanding atmosphere and showed that the only steady-state solution is a singular one in which the velocity and density, outside a certain critical point, vary with radial distance according to the equations:

$$v(r) = v_\infty(1 - R/r)^{1/2} \tag{2.1}$$

$$\rho(r) = \frac{\dot{M}}{4\pi r^2}(1 - R/r)^{1/2} \tag{2.2}$$

where R is the stellar radius and the terminal velocity v_∞ and the mass loss rate $\dot{M}$ depend on the summed opacity of the many lines. Abbott (1982) expanded the line list to include 250,000 lines. The early work made the approximation that that the stellar photons which propel the wind have only radially outward momenta, as if the star from which they were emitted were a point source. In further work (e.g. Pauldrach et al. 1986; Kudritzki et al. 1989) the effect of the finite size of the star is included. Approximate solutions which include this effect have the form:

$$v(r) = v_\infty((1 - v_1/v_\infty)(1 - R/r)^\beta + v_1/v_\infty) \tag{2.3}$$

$$\rho(r) = \frac{\dot{M}}{4\pi r^2 v(r)} \tag{2.4}$$

with β in the range from 0.7 to 1.0.

These power-law wind distributions have not been sufficient to explain the extended X-ray eclipse transitions observed in HMXBs. In observations of eclipse transitions, the X-ray spectrum shows increasingly more absorption of a direct component towards full eclipse where only a residual component is observed. Observations of Cen X-3 (Clark et al. 1988), Her X-1 (Day et al. 1988), Vela X-1 (Sato et al. 1986), and SMC X-1 (Woo et al. 1995a) require a stellar atmospheres which fall off exponentially from the star with a scale height of order 1/10 of the stellar radius.

The stellar wind in a massive X-ray binary must be significantly more complicated

than the spherically symmetric models described above. The presence of a compact object in orbit with the star perturbs the gravity, and the X-ray flux from the neutron star ionizes the wind which disrupts the line-driven acceleration. The X-ray flux from the compact object may also heat the exposed face of the star, causing a thermal wind to emanate from that side of the star. The three dimensional hydrodynamic simulation of Blondin & Woo (1995) was based on the geometry and X-ray luminosity of SMC X-1. This simulation included the radiatively driven wind and its disruption where the ionization parameter ($\xi = L/nr^2$, described in Chapter 6) is greater than 100, and a radiatively driven wind from the illuminated face of the companion star, but not the effect of gravity of the compact object. The simulation was carried out on only one side of the orbital plane, exploiting the symmetry about that plane. In these simulations (Figure 2-1), the radiative wind is emitted from the X-ray shadowed side of the star and the thermal wind from the X-ray illuminated side. However, the radiative wind is bent slightly into the X-ray illuminated region. These results are qualitatively similar to two-dimensional hydrodynamical simulations of high luminosity X-ray binaries previously carried out by Blondin (1994).

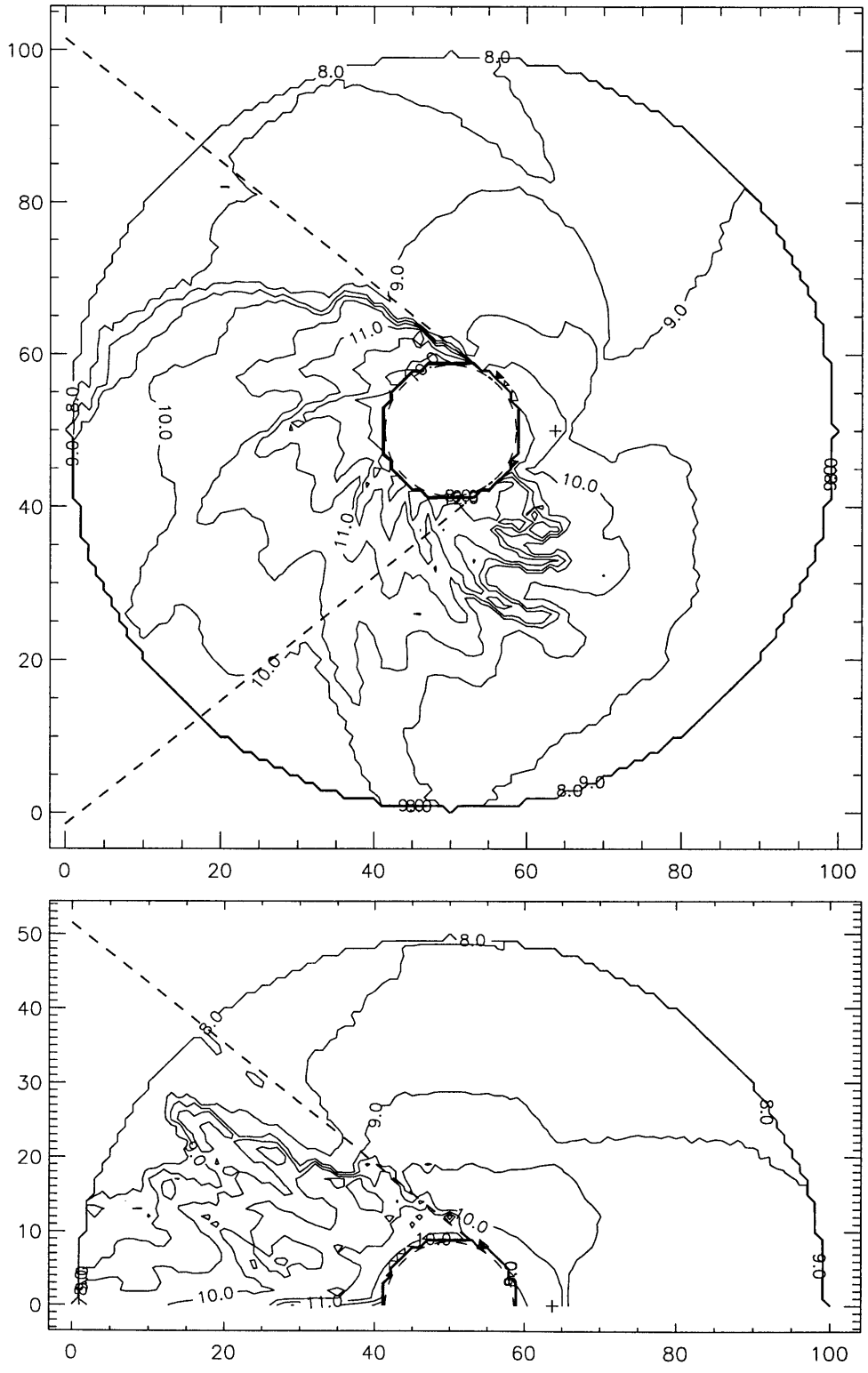

Figure 2-1: Contour plots of $\log_{10}(n)$, where n is the density of hydrogen, in the orbital plane (above) and the plane that includes the orbital axis and the compact object (below). The location of the neutron star is marked (+) and the X-ray shadowed/illuminated boundary is marked with a dashed line. The axes are labeled in pixels of the simulation and have size 1.43×10^{11}cm.

Chapter 3

The Magellanic Clouds and SMC X-1

3.1 The Magellanic Clouds

The Small and Large Magellanic Clouds (SMC and LMC) are two dwarf galaxies, distant from the sun by 60 and 50 kiloparsecs, respectively. They are located in the southern hemisphere at a declination of approximately $-73°$. Each is a few degrees in spatial extent, and the two are separated by approximately ten degrees. The SMC and the LMC are gravitationally bound to each other and to our own galaxy. Both of the MCs have irregular structure though the SMC is more irregular. The SMC is extended along the line of sight to it, by at least 7, but possibly as much as 20 kiloparsecs, and may be divided into near and far fragments, possibly the result of an interaction with the LMC (Westerlund 1997).

As in any galaxy, the metal abundances in the Magellanic Clouds are related to their evolutionary history. An example of this connection is given by Pagel & Tautvaišienė (1998). Metal abundances in the Magellanic clouds have been measured in HII regions and supernova remnants (e.g. Russell & Bessell 1989), supergiant stars (e.g. Russell & Dopita 1990), and main sequence stars (e.g. Rolleston et al. 1993). These and other abundance measurements have been reviewed by Westerlund (1997). The metal abundances in the clouds are less than solar by approximately -0.2 dex for the LMC and -0.6 dex for the SMC (i.e. the logarithm of the abundances are 0.2 and 0.6 less than in that that of solar), though some measurements give lower abundances

(< -1 dex) for carbon and nitrogen. Abundance measurement from different classes of objects do not always agree, and even measurements of the abundances in different objects of the same class do not always agree. Furthermore, abundance measurements in supergiant stars are often based on models with large uncertainties. Measurements of the abundances in the wind of an X-ray binary with a supergiant companion by X-ray reprocessing may help to constrain the abundances in the clouds, at least for this class of object. The radiation physics of optically thin winds are much simpler than that of stellar atmospheres and the interpretation of X-ray spectra depend on a different set of atomic data.

3.2 SMC X-1

X-rays from "an extended region or set of sources" in the SMC were discovered in a rocket observation by Price et al. (1971). Leong et al. (1971) identified a discrete source in the wing of the SMC in *Uhuru* observations and named it SMC X-1. Further analysis of these and additional *Uhuru* observations by Schreier et al. (1972) revealed the eclipse phenomena which established its binary nature. The identification of its optical counterpart as the B0I star Sk 160, suggested by Webster et al. (1972), was confirmed by Liller (1973) who observed an optical intensity variation with the same period as that of the X-ray eclipses. Lucke (1976) discovered the X-ray pulsations in rocket and Apollo satellite observations. Accurate values of the orbital elements of SMC X-1 and rates of spin-up due to accretion torque were derived by pulse-timing analysis of *SAS 3* data by Primini, Rappaport, & Joss (1977) and of *Ariel V* data by Davison (1977). Measurements of the velocity curve of Sk 160 by optical spectroscopy (Hutchings et al. 1977; Reynolds et al. 1993), combined with the velocity curve of the pulsar, yielded narrow limits on the masses of both components of the binary system. An X-ray burst lasting approximately 80 seconds and aperiodic variability on time scales ranging from tens of milliseconds to hours were reported from *EXOSAT* observations by Angelini, Stella, & White (1991). Levine et al. (1993) determined the rate of orbital decay in a comprehensive analysis of the eclipse center times derived

by pulse-timing analysis of data from various satellite observations through 1989, including their own observations with the *Ginga* satellite.

The circumstellar environment of the Sk 160/SMC X-1 system has been the subject of several investigations. Van Paradijs & Zuiderwijk (1977) attributed anomalies in five-color photometry of Sk 160 to the optical emission from an accretion disk around the neutron star, and Tjemkes, van Paradijs, & Zuiderwijk, (1986) interpreted the optical light curve in terms of ellipsoidal variations, disk emission, and X-ray heating effects. Hammerschlag-Hensberge, Kallman, & Howarth (1984) found evidence in UV spectra obtained from *IUE* of the influence of X-ray illumination on the stellar wind of Sk 160 in the form of a deviation from spherical symmetry of the outflow and an anomalously low terminal velocity compared to stars of similar spectral type. Blondin & Woo (1995) modeled the wind dynamics of the Sk 160/SMC X-1 system in three-dimensional hydrodynamical calculations which took account of the effects of X-ray ionization. Model light curves and spectra derived by Monte Carlo calculation of X-ray propagation through the stellar wind conformed well to the light curves and spectra of SMC X-1 derived from *Ginga* and *ROSAT* observations, and in particular with the data obtained during eclipse transitions when the X-ray line of sight passes close to the surface of Sk 160 (Woo et al. 1995a).

Extended periods of very low X-ray flux of the uneclipsed source have been reported in observations with *Uhuru* (Schreier et al. 1972), *Copernicus* (Tuohy & Rapley 1975), *Ariel V* (Cooke 1978), and *COS-B* (Bonnet-Bidaud & Van Der Klis 1981). An extended period of exceptionally high flux, beginning in 1970 September and lasting $\sim$ 100 days, was reported from a three-year record of observations by the *Vela 5B* monitor (Whitlock & Lochner 1994). Gruber & Rothschild (1984), in particular, reported a large amplitude high-low state variation in the X-ray flux in data from three $\sim$ 80 day observations with the UCSD/MIT instrument on *HEAO 1* in 1977 and 1978. They noted that the observed variations could be ascribed to either a quasi-periodic cycle with a duration of about sixty days or to a band-limited red noise process of unspecified origin.

SMC X-1 has a number of desirable qualities for the analysis in this thesis. Its

distance has been determined to be 45 ± 5 kpc (Howarth 1982) so its luminosity is derivable with good accuracy from its flux. The absorbing column of interstellar material between the solar system and SMC X-1 is small so its spectrum in the range 0.5–1 keV (which contains the K transtions of oxygen and many other important features) is not obscured. At least one very strong burst X-ray burst has been observed from SMC X-1 with *EXOSAT* and the persistent flux after the burst was 35% lower than before the burst (Angelini et al. 1991). However, most observations of SMC X-1 out of eclipse which last a few days or less show that its flux, averaged over the 0.71 second pulsation, is constant to within $\sim$10% (e.g. Angelini et al. 1991, Woo et al. 1995a). Of the eight pointed observations of SMC X-1 presented herein, the four observations in which SMC X-1 varied by more than 10%, other than the eclipse transitions, the variability was attributed to changes in the column density of absorbing material rather than changes in the intrinsic luminosity of the source. Thus, one can be reasonably confident that the intrinsic source spectrum and luminosity will not vary during a single eclipse observation while a spectrum of reprocessed radiation is being accumulated. The fact that the X-ray flux from SMC X-1 does not show variations due to absorption, except for the eclipse transitions, and that the flux from SMC X-1 drops by approximately a factor of 50 in eclipse demonstrate that most paths through the wind in the system are optically thin and that except possibly for the dense regions near the stellar surface, the approximations of the algorithm described in Chapter 7 are valid.

Chapter 4

Observations

Bright X-ray sources have been monitored with the BATSE instrument in the 20-100 keV range since April of 1991 and with the ASM instrument in the 1.5-12 keV range since 20 February 1996. The BATSE instrument has been described by Fishman et al. (1994), and the ASM instrument by Levine et al. (Levine et al. 1996). Source intensities are derived from BATSE data by fitting the predicted changes in count rates caused by earth occultations to the measured rates (Harmon 1992). Intensities of known sources are derived from ASM data by fitting predicted shadow patterns cast by coded masks to observed patterns recorded by position-sensitive proportional counters.

The *Ginga* data were obtained with the Large Area Counter (LAC) comprised of 8 proportional gas counters with a peak total effective area of 4000 cm^2, a mechanically-collimated field of view of $1.1° \times 2.0°$ FWHM, an energy range from 1.5 to 36 keV, and an energy resolution of 20% FWHM at 5.9 keV. The *Ginga* observatory has been described by Makino (1987) and details of the LAC by Turner et al. (Turner 1989).

Data from four *ROSAT* imaging observations were obtained with the Position Sensitive Proportional Counter (PSPC) in the focal plane of the X-ray telescope (XRT). The *ROSAT* mission has been described by Trümper (Trümper 1983) and the XRT-PSPC system by Pfeffermann et al. (1987) and Aschenbach (1988). The XRT-PSPC had an angular resolution of $\sim 25''$, and was sensitive in the energy range from 0.1 to 2.5 keV. We denote the four *ROSAT* observations with the labels "1",

"2", "3", and "C". In the numbered observations, SMC X-1 was close to the center of the imaged field of view. Observation "C" was part of a survey of the SMC (Kahabka & Pietsch 1996); in that observation SMC X-1 was $\sim 40'$ off axis.

The *ASCA* data were obtained with the two Solid-state Imaging Spectrometers (SIS) and the two Gas Imaging Spectrometers (GIS) on board. Each one of these detectors has an effective area of approximately 150 cm^2 in energy range from 0.3 to 12 keV. The *ASCA* observatory and the SIS detectors are described in more detail in Appendix A. The *ASCA* observation labeled "1", conducted while the source was uneclipsed, occurred soon after launch, during the performance verification phase. In this observation, *ASCA* was pointed at SMC X-1 over a period of approximately 90,000 seconds (25 hours). However, during the last 30,000 seconds of the pointing, the SIS detectors collected no data. During the remaining 60,000 seconds, the SIS detectors operated for 42,000 seconds. The data were screened according to the default criteria described in Section A.3 resulting in 17,769 seconds of SIS0 data and 17,573 seconds of SIS1 data. In the eclipsed observation, labeled "2", SMC X-1 was observed over a period of approximately 94,000 seconds resulting in 32,838 seconds of SIS0 data and 32,239 seconds of SIS1 data after screening by the default criteria.

The pointed-mode *RXTE* data were obtained during the in-orbit checkout (IOC) period of operation with the Proportional Counter Array (PCA) which has a peak effective area of 7000 cm^2, a mechanically-collimated 1° FWHM field of view, 18% energy resolution at 6 keV, and an energy range from 2 to 60 keV (Jahoda et al. 1996).

Table 4.1 summarizes the times and exposures of the pointed observations and the "state" of SMC X-1 in the high-low cycle as defined below.

4.1 Data Reduction for Pointed Observations

Background rates in the source region of the images produced by the *ROSAT* and *ASCA* observatories were estimated from the count rates in separate nearby regions. For *ROSAT* observations 1, 2, and 3 we chose the source region to be a circle of radius $150''$ and the background region to be an annulus of inner radius $150''$ and

Instrument and ID	Start Time-Stop Time	Phases[1]	Exposure (s)	State	ref
Ginga	1989 Jul 30.78-Aug 3.20[2]	0.34 – 0.21	74240	high	1
ROSAT 1	1991 Oct 7.17-8.13	0.48 – -0.29	16634	high	2
ROSAT C	1991 Oct 16.31-19.98	-0.18 – -0.24	22173	low	3
ROSAT 2	1992 Sep 30.71-Oct 2.59	-0.15 – 0.33	8932	low	2
ROSAT 3	1993 Jun 2.99-4.20	-0.13 – 0.18	11864	high	2
ASCA 1	1993 Apr 26.94-27.97	0.35 – -0.39	34507	high	
ASCA 2	1995 Oct 18.79-19.88	-0.17 – 0.11	30628	low	
RXTE	1996 Jan 11.00-11.23	0.47 – -0.47	14536	high	

Table 4.1: Summary of Pointed Observations. The exposures listed for the *ASCA* observations are for the GIS2. The exposures for GIS3 are the same within 200 seconds. The exposures of the SIS detectors are detailed in the text.
(1) Woo, et al. (1995a); (2) Clark, et al. (1997); (3) Kahabka & Pietsch (1996).

outer radius 300″. For the poorly focused *ROSAT* C observation, we chose the source region to be a circle of radius 262.5″ and the background region to be an annulus with radii of 262.5″ and 487.5″. We excluded from both the background and source regions a circular region of radius 150″ (188″ for the off-axis pointing) centered on the foreground coronal star HD 8191 - a weak soft X-ray source. Also, we excluded a circular region of radius 150″ around the transient source RX J0117.6-7330 (Clark et al. 1997) in the two observations (2 & 3) in which it appeared.

In the GIS image of the *ASCA* observations, we chose the source region to be a circle of radius 383″ and the background region to be an annulus of radii 383″ and 766″. In observation 2, a circular region of radius 150″ around HD 8191 was removed from both the source and background regions. In the SIS image, we chose the source region to be a square 380″ on a side centered on SMC X-1 and used the remainder of the chip as the background region. HD 8191 was not in the field of view of the SIS in these observations.

Background corrections to the *Ginga* data were made according to the algorithm of Hayashida et al. (1989). Background corrections to the *RXTE* data were derived from the earth-occulted count rates which are listed in Table 4.2 together with the on-target rates in seven energy ranges. We note that the *ROSAT* images show several faint and soft sources near SMC X-1 that were within the *Ginga* and *RXTE* fields

	Average Count Rates (counts s^{-1})	
Energy Range (keV)	SMC X-1 +Background	Earth Occulted
2.0-3.4	43.5	5.7
3.4-5.8	173	5.0
5.8-8.6	173	4.6
8.6-21	238	21
21-60	74	53

Table 4.2: Average Count Rates in Seven Energy Ranges of *RXTE* Data

of view. No corrections to the background rates were made for these sources because their total contribution to the *Ginga* count rate was less than a few percent of the SMC X-1 eclipsed count rate (Woo et al. 1995a), and less than one percent of the *RXTE* rates.

Chapter 5

Quasi-Periodic Occultation by a Precessing Accretion Disk

5.1 Long-Term Flux Behavior

Figure 5-1 displays the X-ray light curves of SMC X-1 measured by the ASM and BATSE instruments during times when the pulsar was uneclipsed and in the orbital phase range between 0.1 and 0.9 relative to eclipse center. The ASM data are binned in intervals of the 3.89-day orbital period, and the BATSE data in five-day intervals.

The cyclic flux variation on a time scale of $\sim$ 60 days, suggested by Gruber & Rothschild (1984) is clearly evident in the ASM light curve. To quantify the duration of each cycle, which appears to be variable, we defined times of the beginning and end of each high state to be when the count rate increased/decreased to 2 counts s^{-1}. We determined these times by interpolating between successive points with values below and above, or above and below, 2 counts s^{-1}. The times between successive rises and falls defined in this way are plotted against cycle number in Figure 5-2 where they are seen to range from below 50 to above 60 days with a generally decreasing trend. The ASM light curve shows that the flux often increased relatively quickly at the beginning of each high state and decreased more slowly at the end.

To test for the presence of cyclic variability in the BATSE data, we divided the

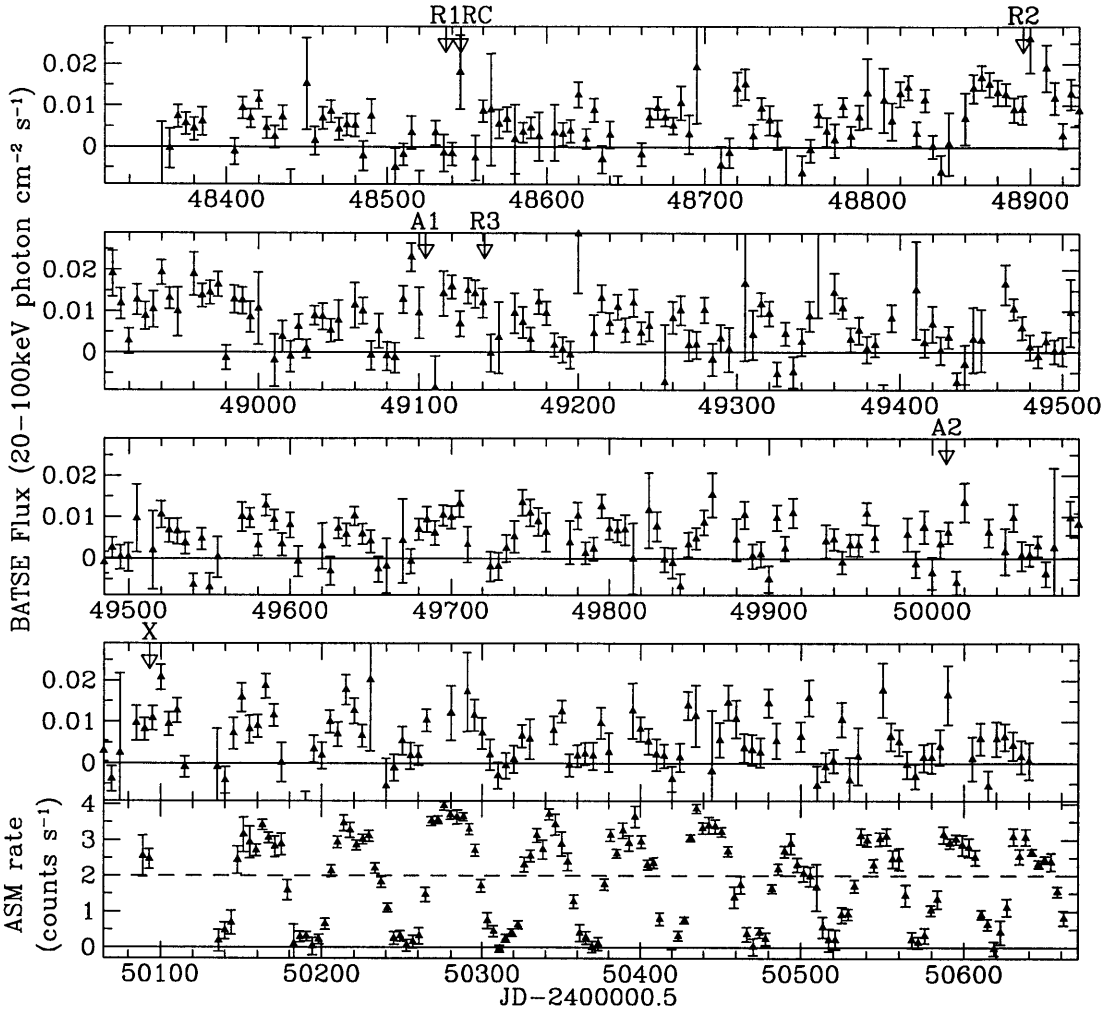

Figure 5-1: *CGRO* BATSE and *RXTE* ASM (1.5-12 keV)light curves of SMC X-1. The time of the start of each of the pointed observations is indicated on this figure by R for *ROSAT*, A for *ASCA*, and X for *RXTE*.

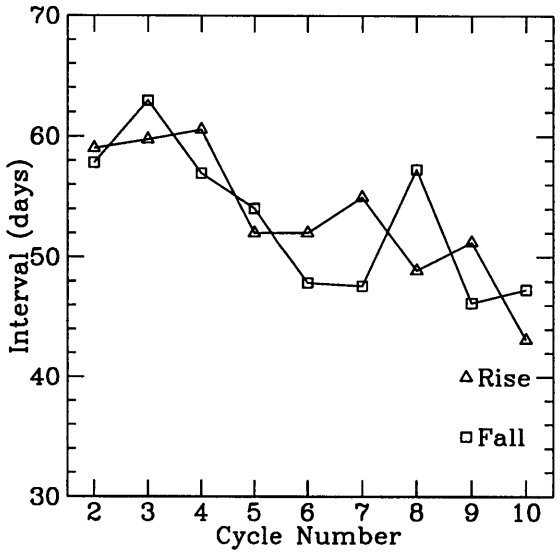

Figure 5-2: Deviations from the average count rates, given in terms of a reduced chi-squared statistic, of four sections of the BATSE light curve, of the entire BATSE light curve, and the ASM light curve when folded at various trial periods. The horizontal bars indicate the expected width (FWHM) of a peak corresponding to a sinusoidal variation with constant period.

data into four subsets of equal duration and folded each subset into 5 phase bins with trial periods between 30 and 100 days. In this process, the mean flux and its standard deviation in each phase bin were calculated using the inverses of the variances of the individual measurements as weights. At each trial period, we calculated the reduced χ^2 statistic of the light curve assuming that no signal was present. The values of the reduced χ^2 statistic are plotted in Figure 5-3 for each quarter of the BATSE light curve and for the entire BATSE light curve. Also shown are the results of the same analysis applied to the entire ASM light curve. Leahy et al. (1983) showed that if a sinusoidal signal with a fixed period, P, is present in the light curve, such a folding analysis will show a peak centered at that period with a FWHM of P^2/T, where T is the length of the observation. In Figure 5-3 the horizontal bars show the expected FWHM of a sinusoidal signal with a 55-day period. We note that the positions of the peaks shift and some of peaks are substantially wider than the horizontal bars. These features, together with the drift of the time since last increase/decrease in the ASM light curve (Figure 5-2), are strong evidence for the absence of a long-term

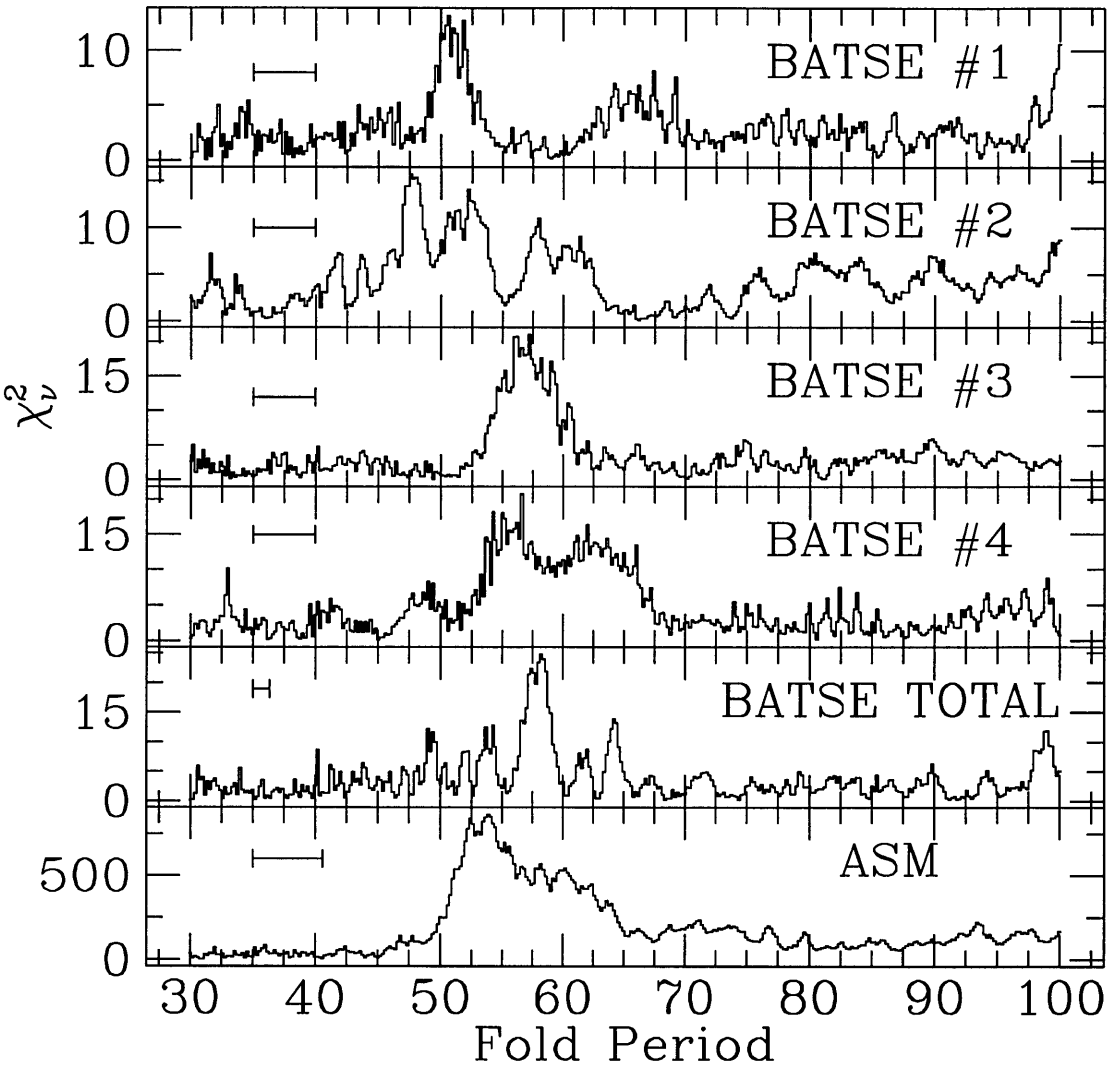

Figure 5-3: Deviations from the average count rates, given in terms of a reduced chi-squared statistic, of four sections of the BATSE light curve, of the entire BATSE light curve, and the ASM light curve when folded at various trial periods. The horizontal bars indicate the expected width (FWHM) of a peak corresponding to a sinusoidal variation with constant period.

coherent periodicity in these data sets. Instead, the observed cyclic variation can be best characterized as quasi-periodic with recurrence times that wander between ~50 and ~60 days. Attempts to examine the variation of the cycle more closely in the BATSE light curve by smoothing and by correlation with a sine wave were inconclusive, presumably due to the low signal-to-noise ratio in the data.

5.2 Short-Term Flux Behavior

Background-subtracted count rates, derived from the *Ginga*, *ROSAT*, *ASCA*, and *RXTE* PCA observations, are plotted in Figure 5-4 against orbital phase. We multiplied the background-subtracted count rates of the off-axis *ROSAT* observation by a factor of 1.7 to compensate for the reduction in effective area relative to the on-axis observation. So that the *Ginga* and *ASCA* count rates may be directly compared, we show the count rates from the pulse height channels which correspond to the energy range 1-10 keV. For the *ASCA* GIS, these are PI channels 85 through 850. For the *Ginga* LAC these are channels 3 through 18 in the MPC-2 mode data and 1 to 4 in the MPC-3 mode data.

With the exception of the *Ginga* observation, which occurred before the beginning of the BATSE light curve, all of the pointed observations discussed in this paper occurred during the time of the BATSE observations, and before the *RXTE* ASM observations. Unfortunately, the signal-to-noise ratio of the BATSE light curve is not large enough to allow certain determination of the phases in the flux cycle at which the individual pointed observations occurred. Furthermore, because of the quasi-periodic nature of the cycle, it is not possible to extrapolate backwards from the ASM light curve. However, the ASM light curve shows that the X-ray flux averaged over the uneclipsed portion of each binary orbit rises and falls smoothly over each cycle. Therefore, we are confident that the observed out-of-eclipse flux of the source, as it is revealed in the light curves, is a reliable indicator of the state of the source.

The contrast between the high and low states of SMC X-1 is most clearly demonstrated by the various *ROSAT* observations. Where observation 1 and the region C

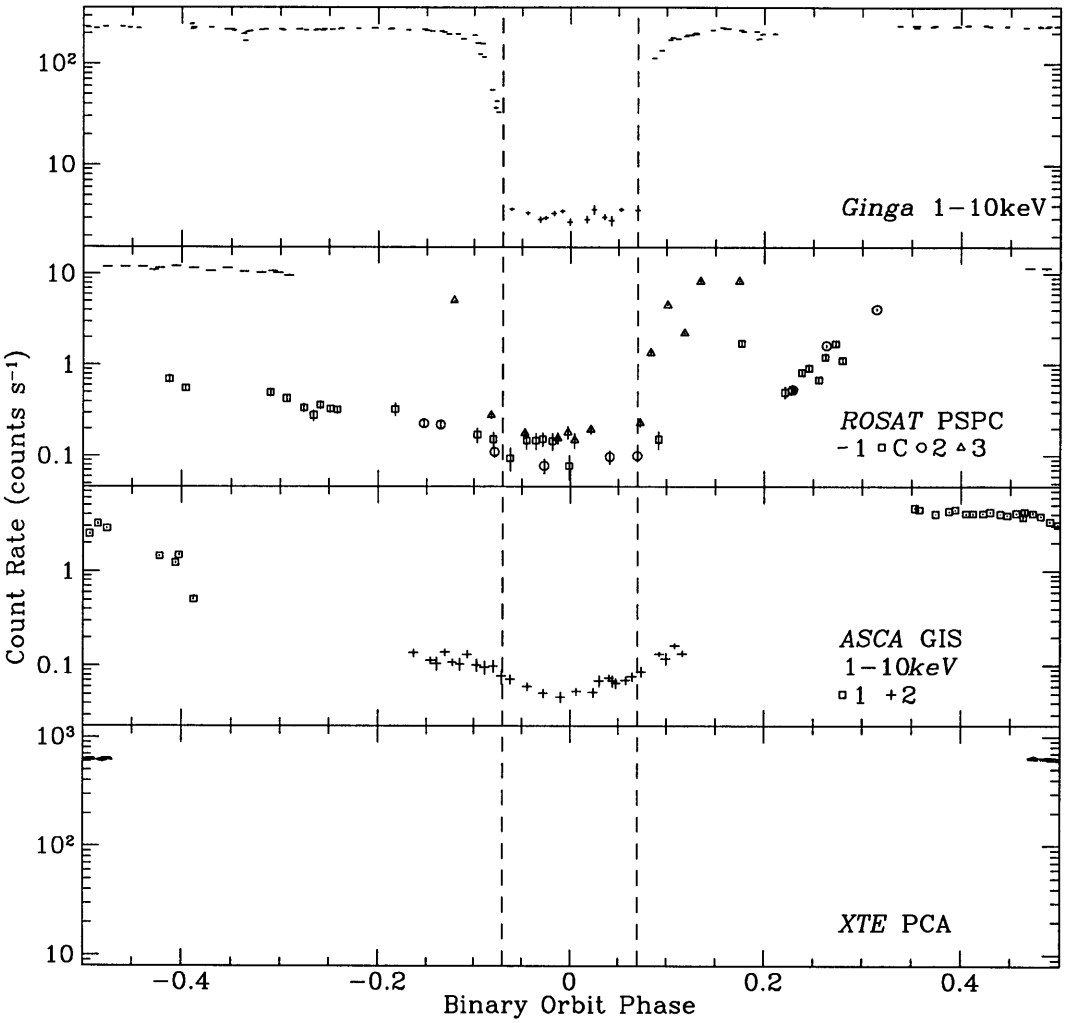

Figure 5-4: Count rates of SMC X-1 as a function of orbital phase for the pointed observations. The *ROSAT* PSPC region C count rates are corrected for off-axis vignetting. Dashed lines at orbital phase ± 0.07 indicate the end of immersion and beginning of emersion of the eclipse transitions observed in the high state.

observation overlap in orbital phase outside of eclipse, they differ in (corrected) count rate by a factor of at least 20. We therefore identify *ROSAT* observation 1 as having occurred during the high state and the region C observation as having occurred during the low state. The light curve of *ROSAT* observation 2 behaves like that of the region C observation where the two overlap so we identify this observation as having occurred during the low state as well. Outside of eclipse, *ROSAT* observation 3 shows a count rate comparable to that of observation 1, so we identify it as having occurred during the high state.

The two *ASCA* observations also differ by a factor of about twenty in their out-of-eclipse count rates, so we assume *ASCA* observation 1 occurred during the high state and *ASCA* observation 2 occurred during the low state. However, the decline in the count rate in observation 1 beginning near orbital phase 0.5 may be a transition to the low state. In the *Ginga* observation, the out-of-eclipse behavior and count rate is comparable to *ROSAT* observation 1 and *ASCA* observation 1, so we conclude it also occurred during the high state. The brief *RXTE* PCA observation near orbit phase 0.5 clearly occurred during a high state.

Interesting features of the low-state light curves derived from the *ROSAT* observations 2 and C are the increases in the count rates near orbital phase 0.25. In both cases, 0.71 second pulsations are present during the increase. A similar turn-on may be seen in the light curve (not shown herein) derived from the *ROSAT* All-Sky Survey (Kahabka & Pietsch 1996), although those data do not have sufficient time resolution to permit a test for the presence of pulsations. *ROSAT* observation 2 ends near phase 0.3 with this increase. The *ROSAT* C observation has a gap from phase 0.3, where the count rate is increasing, to phase 0.58 (plotted at phase -0.42), where the count rate is lower than before.

In Figure 5-5 we plot the photon number spectra of SMC X-1 from all the observations during the in-eclipse portions of the binary orbit (orbital phase -0.07 to +0.07). For the purpose of comparing these spectra, we fitted all of them simultaneously with the following model spectrum that consists of the sum of a black-body spectrum and

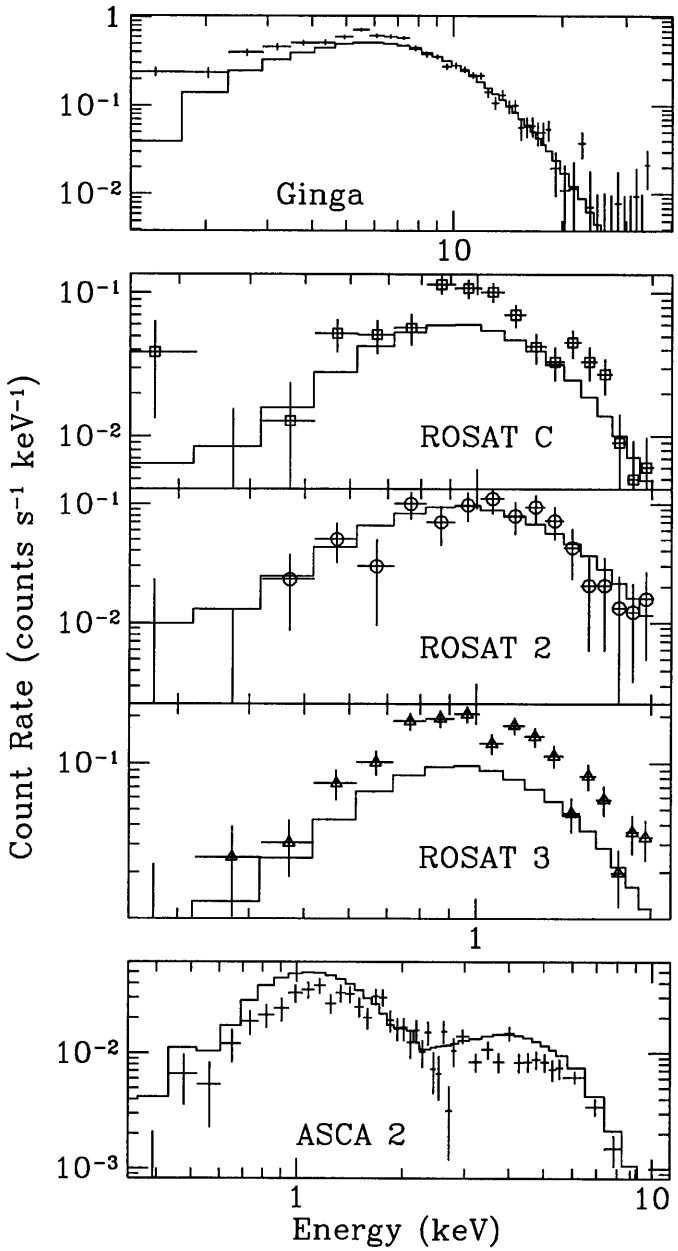

Figure 5-5: Observed photon number spectra during eclipses (orbital phase in the range -0.07 to +0.07) and the computed spectra (solid lines) for a single fitted model.

a power law with a high energy cutoff together with interstellar absorption:

$$I(E) = \exp[-\sigma(E)N_{\rm H}][f_{\rm bb}(E) + f_{\rm pl}(E)], \tag{5.1}$$

where

$$\begin{aligned} f_{\rm bb}(E) &= I_{\rm bb}(E/E_{\rm bb})^2(e-1)[\exp(E/E_{\rm bb})-1]^{-1}, \\ f_{\rm pl}(E) &= I_{\rm pl}(E/1{\rm keV})^{-\alpha} \times \left\{ \begin{array}{ll} 1, & E < E_{\rm c} \\ \exp\left[-\frac{E-E_{\rm c}}{E_{\rm f}}\right], & E \geq E_{\rm c} \end{array} \right\}. \end{aligned}$$

$I_{\rm bb}$ is the the intensity of the blackbody component at $E = E_{\rm bb}$, $I_{\rm pl}$ is the intensity of the power law component at $E = 1$ keV, and $\sigma(E)$ is the photoelectric absorption cross section of cold matter (Morrison & McCammon 1983). The results of the fit are given in Table 5.1. The convolutions of this model with each of the instrument responses are plotted in Figure 5-5 along with the corresponding observed spectra. The instrument response for the *ROSAT* C observation includes the reduced efficiency at the off-axis location.

The high-low state identifications we have inferred from the observed fluxes leave no doubt that the spectra displayed in Figure 5-5 include instances from both the high and low states during the eclipse when the only X-rays detected are those that have been scattered from circumsource matter. Since these five spectra show no more than a factor of two difference in flux at any X-ray energy, we conclude that the average illumination of the circumsource matter varied little between the high and low states. Moreover, all five spectra have similar shapes. Thus, the cause of the cyclic variation cannot be either a variation in the intrinsic luminosity of SMC X-1 or a redistribution of the luminosity across the spectrum. We conclude that the cause of the cyclic variation between states of high and low flux is a quasi-periodic blockage of the line of sight. The same conclusion regarding the cause of the long-term cyclic variation in the X-ray flux of LMC X-4 has been drawn on the basis of similar evidence (Woo et al. 1995b).

5.2.1 Motions of the Accretion Disk

Shortly after discovery of the 35-day high-low state variation in Her X-1, Katz (1973) suggested that if the rim of the neutron star's accretion disc does not lie in the plane of the binary orbit, then the plane of the rim will precess due to the gravitational force of the companion star. Katz argued that if the rim is sufficiently tilted, it will periodically block the line of sight to the neutron star, causing the observed cyclic high-low variation. His expression for the forced precession period, $P_{\rm f}$, of a ring of non-interacting particles can be written in the form

$$P_{\rm f} = \frac{4}{3} P_{\rm b} \left(\frac{R_{\rm L}}{R_{\rm r}}\right)^{3/2} \left[\frac{0.6q^{2/3} + \ln(1+q^{1/3})}{0.49q^{2/3}}\right]^{3/2} (q+q^2)^{1/2} (\cos\beta)^{-1}, \qquad (5.2)$$

where $P_{\rm b}$ is the binary orbital period, $R_{\rm L}$ is the volume-averaged radius of the Roche lobe, $R_{\rm r}$ is the ring radius, q is the ratio of the neutron star mass to the companion star mass, and β is the tilt angle of the ring with respect to the plane of the binary orbit. The quantity in square brackets is an approximate expression for the ratio of the binary separation to the Roche lobe radius (Eggleton 1983).

Analyses of the optical light curves of Sk 160/SMC X-1 indicate that the accretion disk radius is $\sim$ 0.7 to 1.0 times the Roche lobe radius (Howarth 1982; Tjemkes et al. 1986; Khruzina & Cherepashchuk 1987). Setting $R_{\rm r}/R_{\rm L} = 0.7$, $q = 0.0909$ (Reynolds et al. 1993), $P_{\rm b} = 3.892$ days, and $\cos\beta \approx 1$, we find the precession period predicted by equation 5.2 is 31 days or 0.56 times the typical observed cycle time of 55 days. The optical light curves of the two other X-ray binaries with clear quasi-periodic high-low state cycles, Her X-1 and LMC X-4, also indicate that their accretion disks nearly fill the Roche lobes of their neutron stars (Gerend & Boynton 1976; Ilovaisky et al. 1984; Heemskerk & Van Paradijs 1989). The corresponding precession periods (assuming $R_{\rm r}/R_{\rm L} = 0.7$ and $\cos\beta \approx 1$) are 0.56 and 0.35 times the observed high-low cycle periods of Her X-1 and LMC X-4, respectively. Thus, in all three cases a simple model of an occulting rim of non-interacting particles predicts precession periods substantially less than the observed high-low cycle times.

Numerous theoretical investigations of the effects of the accretion rate, viscosity,

and X-ray illumination on the creation of warp and tilt in the disk and on the precession rate have been carried out. Among these investigations we note in particular the work of Iping & Petterson (1990). They made numerical simulations with results that showed stable precessing disks with quasi-periods that could be adjusted to fit observations by appropriate choices of the accretion rate, the conversion efficiency with which accretion energy is converted into X-rays, and the viscosity parameters. Pringle (1996) confirmed their results with a more rigorous treatment, and showed that a warp instability due to radiation pressure will develop outside a critical radius which is $\approx 3 \times 10^8$ cm for a neutron star. The radius of the Roche lobe in SMC X-1 is $\approx 2.9 \times 10^{11}$cm so the accretion disk is clearly large enough to be unstable to warping. Thus it appears that a detailed model of a precessing tilted accretion disk could provide a quantitative explanation for the observed high-low cycle of SMC X-1.

It is unlikely that random flares were the cause of the short-term flux increases observed near orbital phase 0.25 in the three low-states observations. The presence of 0.71 second pulses in the *ROSAT* 2 and C observations shows that the increased flux came directly from the neutron star. It is also unlikely that the increase in the *ROSAT* C observation was the beginning of a high-state because a decrease followed soon after, and because the observation occurred only ten days after the source was observed to be in a high state in *ROSAT* observation 1. The ASM light curve shows that low states typically last for 15-20 days. Thus the *ROSAT* C observation probably occurred in the early part of a low state. These increases are reminiscent of the low-state turn-ons in Her X-1 which occur near orbital phases 0.2 and 0.7 (cf. Fig. 2 of Priedhorsky & Holt 1987), and which have been attributed (Levine & Jernigan 1982) to a wobble which may be a common feature of precessing accretion disks. Further observations of SMC X-1 are needed to determine the regularity and nature of its low-state turn-ons.

Parameter	Value(1σ error)	
$N_{\rm H}(10^{20}$ cm$^{-2})$	5.9	(4.2)
$E_{\rm bb}$ (keV)	0.25	(0.02)
$I_{\rm bb}$ (10^{-3} photons cm^{-2} s^{-1} keV^{-1})	9.	(3)
α	-0.2	(0.1)
$I_{\rm pl}(10^{-5}$ photons cm^{-2} s^{-1} keV^{-1})	9.8	(3.1)
$E_{\rm c}$ (keV)	6.5	(0.4)
$E_{\rm f}$ (keV)	5.9	(0.4)
χ^2_ν	3.96	

Table 5.1: Fitted Values of the Spectral Function Parameters

Chapter 6

Photoionized Plasmas

As previously mentioned, bright X-ray sources in X-ray binaries ionize the wind of their companion star. This photoionized wind scatters and re-emits X-rays. While the compact X-ray source is eclipsed, only this reprocessed flux is visible. This chapter explains some of the important details of this photoionization and reprocessing.

The situation of a diffuse cloud of gas (a nebula), heated and ionized by one or more sources of intense radiation, occurs in a variety of astrophysical contexts. In star-forming regions, the optical and UV radiation from bright, young O and B type stars heat and ionize the cloud of material from which they formed. In "planetary" nebula, an old star heats and ionizes a cloud of material which was ejected in an earlier stage in the star's evolution. In active galactic nuclei, an accretion-powered super-massive black hole heats and ionizes nearby clouds of material.

The heating and ionization of a nebula are accompanied by cooling and recombination which results in continuum and line emission. Since the continuum and line emission depend on the state of the gas, the spectrum of the reprocessed radiation is a diagnostic of the conditions in the gas.

In section 6.1, the fundamental physics which determines the state of a gas and the reprocessed radiation from it under the influence of an intense source of radiation are explained. In section 6.2, a short review of calculations and results on photoionized plasmas in the literature which are relevant to this work is given.

6.1 Physics

6.1.1 The State of the Gas

The local state of a gas under the influence of a radiation field, may reach a steady state if this radiation field does not change with time. However, if the mean free path of photons or particles is longer than other length scales of the gas, the local steady state may not resemble thermodynamic equilibrium. In a diffuse photoionized gas, photons from the radiation source, which dominate the heating and ionization, travel far through the gas. Computing the local state of the gas under such conditions is, in general, more difficult than in local thermodynamic equilibrium. In local thermodynamic equilibrium, the Boltzmann equation describes the population of excited states and the Saha equation describes ionization state of all of the atoms. To apply these equations, one needs only to know the energy levels and statistical weights of the various atomic levels. In a photoionized plasma however, it is necessary to explicitly balance all of the various atomic transitions with their inverse processes to calculate the nature of the steady-state making it necessary to know all of the relevant atomic rates and cross-sections.

There are two approximations, however, which are valid over a large range of parameter space and can greatly simplify the rate balance calculations in a diffuse photoionized gas. The first is that the probability that a free electron will collide with another free electron is much larger than the probability that it will interact with an ion. In this approximation, a newly ionized electron quickly becomes thermalized and, for purposes of calculating the rate of any electron-ion interaction, the velocities of the electrons may be assumed to be described by a Maxwell-Boltzmann distribution with a single temperature T. The balance of the free electrons may, in this approximation, be set by requiring that the total ionization rate equal the total recombination rate and that the heating rate of the electrons be equal to their cooling rate.

In general, the populations of the various levels and the free electron distribution are given by the balance of the following processes:

- photoexcitations and de-excitations $\propto Jn_i$

- spontaneous de-excitations $\propto n_i$
- photoionizations $\propto Jn_i$
- collisional excitations and de-excitations $\propto n_i n_e$
- recombinations $\propto n_i n_e$
- free-free emission $\propto n_i n_e$
- Compton heating $\propto Jn_e$

where J is the radiation density for a given spectrum of radiation and n_i is the density of the initial state ion. Explicit expressions for these process rates have been given by Osterbrock, et al. (1989). The rates of the collisional processes depend on the electron temperature T and the photon processes depend on the frequency spectrum of the radiation field. Since n_i and n_e are related to the number density of atoms, n, by a coefficient which depends on the local state of the gas, they may be replaced by n in the list above. All of the processes which determine the local state of the gas, except spontaneous de-excitations, are thus proportional to either Jn or n^2. However, most spontaneous decays are very fast and, in diffuse gases, it is often valid to make a second approximation — excited atoms always decay before undergoing any interaction. This approximation, known as the nebular approximation, greatly simplifies calculations because it allows one not to consider excited states explicitly. For example, instead of considering recombination to a number of available shells, one considers recombination to the ground state through a number of pathways: recombination directly to the ground state, recombination to the first excited level followed by spontaneous decay, etc. In this approximation, for a given spectrum of the radiation field and elemental composition of the gas, the local state of a gas is a function of the ratio J/n.

In a steady state, the energy radiated from a plasma is balanced by energy input from the external sources of radiation. In an optically thin plasma, by definition, the fraction of the input radiation absorbed and re-radiated by the plasma is much smaller than one. Therefore, the radiation field everywhere is dominated by the point

source and is proportional to the luminosity, L, of the point source divided by the square of the distance from the source, r. Therefore, in the nebular approximation, the local state of the gas is a function of the ratio L/nr^2, which, with L in ergs/s and n and r in the appropriate powers of centimeters, is defined to be the ionization parameter ξ[1] (Tarter et al. 1969).

6.1.2 X-ray Reprocessing in Photoionized Plasmas

Any process which results in a photon being produced or scattered has an effect on the state of the plasma, and therefore belongs in the itemized list of processes above. Therefore, an accurate accounting of all of the transition rates also determines the reprocessed radiation. It must be kept in mind, however, that certain processes may not always produce the same radiation. For example, when a free electron recombines with an ion, the energy difference between the initial and final states may be carried away by a photon (radiative recombination), or some of that energy may go to the excitation of another bound electron (dielectronic recombination).

The most important scattering and re-emission processes in an X-ray photoionized plasma are recombination, fluorescence, and bremsstrahlung and electron scattering. Free electrons may recombine to any vacant level in an ion. The energy given up in a recombination is equal to the ionization energy of the level recombined to plus the kinetic energy of the free electron. As mentioned above, the velocity distribution of the free electrons is thermal with temperature T. The spectrum of a macroscopic volume of gas undergoing recombination to a particular level, is an emission feature starting abruptly at the ionization energy (I) up to approximately $I + kT$. In some cases, kT may be much smaller than I and so the emission feature will appear narrow and line-like in spectra of moderate resolution. In the nebular approximation, recombination to excited states is immediately followed by spontaneous de-excitation and so the spectral signatures of recombination include emission lines as well as the recombination continua. The magnitude of the emission features, like the recombination

[1]The parameter ξ is taken to be unitless

rates are proportional to n^2.

When an electron from an inner shell is removed from the ion, an electron from an outer shell will fall into its place in a fluorescent cascade. The spectrum resulting from this process consists of one or more emission lines. After the ionization, but before the cascade, the ion is in an excited state and in the nebular approximation, the cascade follows the ionization immediately. Therefore, the strengths of the emission lines from this process are proportional to Jn.

Bremsstrahlung radiation has a well-known flat continuum energy spectrum at low energies and cuts off exponentially at approximately kT. The magnitude of bremsstrahlung radiation is proportional to n^2.

The scattering of photons much lower in energy than $m_e c^2 = 511$ keV can be described by the Thompson approximation to Compton scattering. Photons scatter from free electrons with little change in frequency with the cross-section

$$\sigma_T = 8\pi r_e^2/3 = 6.65 \times 10^{-25}\text{cm}^2 \tag{6.1}$$

where $r_e = e^2/m_e c^2$ is the classical electron radius. Photons may also scatter from bound electrons as if the electrons were free if the binding energies are much less than the photon energies. In gases of astrophysical interest, approximately 98% of the electrons are contributed by hydrogen and helium. Since the greatest binding energy in either of these two elements is 54.4 eV, for purposes of Compton scattering of X-rays of greater than approximately 0.5 keV, it is a very good approximation to assume that the electron density is a constant fraction of the hydrogen density. For the solar abundance of helium relative to hydrogen, this constant, F_e is approximately equal to 1.15. For X-rays in the energy range 0.5–50 keV then, the spectrum of Compton scattered radiation is nearly identical to the spectrum of input radiation and does not depend on the ionization state or temperature of the plasma.

For a gas with elemental abundances $\mathbf{X}$, illuminated by a point source with specific luminosity L_ν, the local volume emission coefficient is:

$$
\begin{aligned}
j_\nu &= [f_{\nu,\mathrm{recomb}}(\xi, L_\nu/L, \mathbf{X}) + f_{\nu,\mathrm{brem}}(\xi, L_\nu/L, \mathbf{X})]n^2 \\
&\quad + f_{\nu,\mathrm{fluor}}(\xi, L_\nu/L, \mathbf{X})\frac{Ln}{r^2} + \frac{L_\nu}{4\pi r^2} F_e n_e \sigma_T
\end{aligned} \tag{6.2}
$$

where $L = \int L_\nu d\nu$. However, the electron density is a function of ξ, the spectrum of the point source radiation L_ν/L, and $\mathbf{X}$, so the Compton scattering term can be written as $\frac{L_\nu}{L}\frac{\sigma_T}{4\pi}F_e\frac{Ln}{r^2}$. Therefore, the fluorescence and Compton scattering terms can, like the recombination and bremsstrahlung terms, be described as functions of ξ, L_ν/L, and $\mathbf{X}$ but scaling with Ln/r^2 instead of with n^2. However, $Ln/r^2 = \xi n^2$ so all of the re-emission can be described as a function of ξ, L_ν/L, and $\mathbf{X}$ scaled by n^2.

6.2 Review

Astrophysical ionized nebulae have been studied since the 1930's (Stromgren 1939). Until the detection of cosmic X-ray sources in the 1960's, however, most of this work centered on diffuse gases ionized by optical and UV radiation (such as in planetary nebulae and star forming regions) and the interpretation of the optical and UV spectra. Much of this physics is described in the textbook of Osterbrock (1989) and references therein. When the spectrum of the radiation extends to higher energies, different physical processes become important. High energy photons can ionize the most tightly bound electrons from the metals, in some cases resulting in bare and hydrogenic ions, and processes involving metals are much more important relative to hydrogen and helium than in cases of low-energy radiation sources.

Before it was known with certainty what the recently detected cosmic X-ray sources were, it was speculated that some of them might be embedded in a cloud of gas which would be ionized by the X-ray source. In this spirit, Tarter, Tucker, and Salpeter (1969) calculated numerically the ionization structure of spherically symmetric, constant density clouds of gas — with densities of 10^3, 10^6, and 10^9 cm^{-3} — containing astrophysical quantities of hydrogen, helium, carbon, nitrogen, oxygen,

and neon with a point sources of bremsstrahlung radiation — with temperatures of 10^6, 10^7, and 10^8 K — at the center. In this work, excited metastable states were considered explicitly. However, it was found that the electron temperature was a strict function of the ionization parameter except at the lowest ionization parameters considered ($\log \xi \lesssim 0$), where the heavy elements were only a few times ionized. Another notable result: in the calculations where the temperature of the input bremsstrahlung radiation was 10^7 and 10^8, the electron temperature T changed rapidly as a function of $\log \xi$ in a narrow range of $\log \xi$ near $\log \xi = 2.5$. The change was more rapid for the higher temperature input bremsstrahlung spectra. In this narrow range of $\log \xi$, the heavy elements lost their last few electrons. At ionization parameters above the region of rapid change, T changed very little. These calculations were expanded to include optically thick gas by Tarter and Salpeter (1969). They showed that in optically thick media, ionization fronts form — across a very narrow spatial zone, electron temperatures and ionization states changed drastically. Tarter and Salpeter (1969) also calculated continuum and emission line spectra emergent from some of their models.

Buff and McCray (1974) calculated the structure of optically thin, spherically symmetric plasmas using a simple model for the gas. The gas consisted of astrophysically abundant quantities of H, He, C, N, and O but the C, N, and O were considered to have only two ionization states: hydrogenic and fully ionized. In these calculations, for input spectra which are deficient in photons of energy less than 2 keV, they found that over a certain range of ξ, the thermal and ionization balance equations have two stable (and one unstable) equilibrium. The high temperature solution connects continuously with the single solution at large ξ and the low temperature solution connects continuously with the single solution at low ξ. Gas in the bistable region, therefore, exhibits hysteresis. This bistability continued to be seen in later calculations using more realistic models of the gas.

Hatchett, Buff, and McCray (1976) conducted calculations which improved on those of Tarter and Salpeter (1969) by including Si, S, and Fe in the gas, Compton heating of the electrons, and Auger processes in the atomic transitions. This work was

further improved by Kallman and McCray (1982) to include more of the ionization stages (Hatchett, Buff, and McCray (1976) neglected many lower ionization stages in Si, S, and Fe) and calculated emission spectra with 530 lines in the optical, UV, and X-ray. The computer code of Kallman and McCray (1982) (with significant revisions) is publicly available as the XSTAR program which is used in this thesis as the basis of the spectral calculations. At the time of writing, the XSTAR program includes 1700 lines.

Other work on high energy photoionized gases, mostly oriented towards the interpretation of spectra of active galactic nuclei is described in the last two chapters of Osterbrock (1989) and a review by Davidson and Netzer (1979). More recent work includes that of Netzer (1996) and references therein. The CLOUDY (Ferland & Rees 1988) code is another photoionization code, similar in concept to XSTAR, but oriented more toward synthesizing optical spectra.

6.3 XSTAR Calculations

To demonstrate the capabilities of XSTAR, which forms the basis of the spectral simulations in this thesis, results of some XSTAR test calculations are shown here. XSTAR calculates the effect of a point source of radiation at the center of a spherically symmetric volume of gas. The gas is divided into a number of zones — abutting spherical shells with finite thickness. Though the zones have finite thickness, the conditions within a single zone are assumed to be uniform. The radiation incident on the innermost zone is the radiation from the central point source. The radiation incident on outer zones is the sum of the source radiation and the emission from zones inside, both modified by absorption in intervening zones.

The results of XSTAR runs are presented here for central radiation sources with specific luminosities of the form

$$L_E \propto E^{-\alpha} \left\{ \begin{array}{ll} 1 & E \leq 10\mathrm{keV} \\ e^{\frac{E-10\mathrm{keV}}{15\mathrm{keV}}} & E > 10\mathrm{keV} \end{array} \right\} \tag{6.3}$$

H	1.00	Si	3.55×10^{-5}
He	9.77×10^{-2}	S	1.62×10^{-5}
C	3.63×10^{-4}	Ar	3.63×10^{-6}
N	1.12×10^{-4}	Ca	2.29×10^{-6}
O	8.51×10^{-4}	Fe	4.68×10^{-5}
Ne	1.23×10^{-4}	Ni	1.78×10^{-6}
Mg	3.80×10^{-5}		

Table 6.1: Relative Solar Abundances

with α equal to -0.5, 0, and 0.5. The elemental abundances in the gas, relative to hydrogen, were taken to be solar for helium and one-tenth of solar for all of the other elements included in XSTAR, where solar abundances are taken to be those of Anders & Grevesse (1989) (Table 6.1).

In the test simulations, the gas was divided into 100 logarithmically spaced zones ranging in ionization parameter from 10^7 to 10^{-1}. The gas had a constant density of $10^{-3}\mathrm{cm}^{-3}$ and the central source had a luminosity of 10^{33} ergs/sec[2]. The density was chosen to be smaller by several orders of magnitude than the stellar wind densities studied in this thesis and the luminosity was chosen to be smaller than the accreting neutron star luminosity of SMC X-1. This choice of parameters was made to assure that absorption of the source spectrum would be negligible and that the flux of re-emitted radiation would be negligible relative to the flux from the source spectrum even at the outermost zone — i.e. so that the entire gas would be optically thin. Of course, in the optically thin limit, only the ionization parameter is important. The absolute values of the luminosity and the density are not.

The calculated electron temperature as a function of the ionization parameter is plotted in Figure 6-1. For α=-0.5, the hardest spectrum, the hysteresis from the instability of Buff and McCray (1974) is demonstrated. In its normal mode of operation, XSTAR starts the calculation at the innermost zone — which has the highest ionization parameter — and as it moves moves outward, the conditions of the last zone are chosen as the first guess for the solution of the current zone. Therefore,

[2]In XSTAR the luminosity is defined over the interval from 13.6 eV to 13.6 keV.

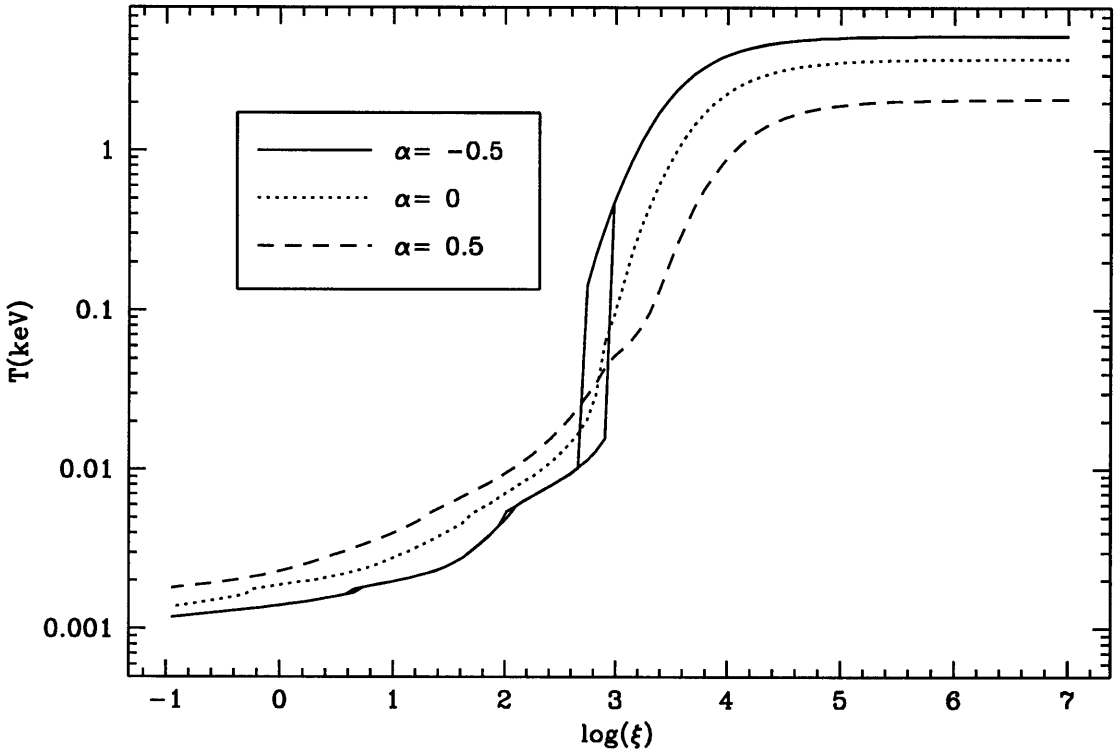

Figure 6-1: Electron Temperature vs. Ionization Parameter for compact source spectra $L_E \propto E^{-\alpha}$ with cutoff at E=10 keV (described in text).

XSTAR follows the high temperature solution through the bistable region until the end of the bistable region is reached, at which point the electron temperature jumps discontinuously down to the low temperature branch. The hot solution was obtained in this way. The cold solution was obtained by modifying the XSTAR source code to use a single very low temperature as a first guess for the conditions at each zone.

In Figure 6-2 are plotted the specific emissivities of plasmas at selected zones of the $\alpha = 0$ run. The variation of the spectra with ionization parameter may be understood by considering the spectrum to be a sum of electron-ion processes (recombination and bremsstrahlung) and photon-matter processes (Compton scattering and fluorescence). The emission due to recombination, bremsstrahlung, and fluorescence are calculated by XSTAR. Compton scattering, which dominates the continuum at most energies at all of the ionization parameters, is added after the XSTAR run using the last term in Equation 6.2. The absolute normalization of the spectra is arbitrary but the relative normalizations are chosen such that the quantity $Ln/r^2 = \xi n^2$, is constant between the panels. At the highest ionization parameters, all of the elements considered are nearly fully ionized and the emission from recombination to these highly ionized atoms (which is proportional to n^2) is very small compared to the Compton scattered radiation (which is proportional to $n^2\xi$) and the spectrum of the reprocessed radiation is the same as that of the incident radiation. As the ionization parameter is lowered, recombination features become visible because of the increase of the ratio of the recombination scaling factor relative to the Compton scattering factor as well as an increase in the efficiency of recombination with decreased electron temperature. The recombination features which are visible at $\log \xi = 3$ include the Kα lines of helium-like iron around 6.68 keV, the Kα line of hydrogen-like iron at 6.9 keV, and the K series of hydrogen-like oxygen: Kα at 0.654 keV, Kβ at 0.774 keV, Kγ at 0.817 keV, Kδ at 0.837 keV, and the K continua beginning at 0.871 keV. At $\log \xi$=2.5 down to $\log \xi$=1.1, many other emission features become visible. Also in this range, the recombination continua become narrower as the electron temperature decreases with ξ. This effect is particularly conspicuous for the hydrogen-like oxygen K shell recombination continuum. In the energy range plotted in Figure 6-2, the emission

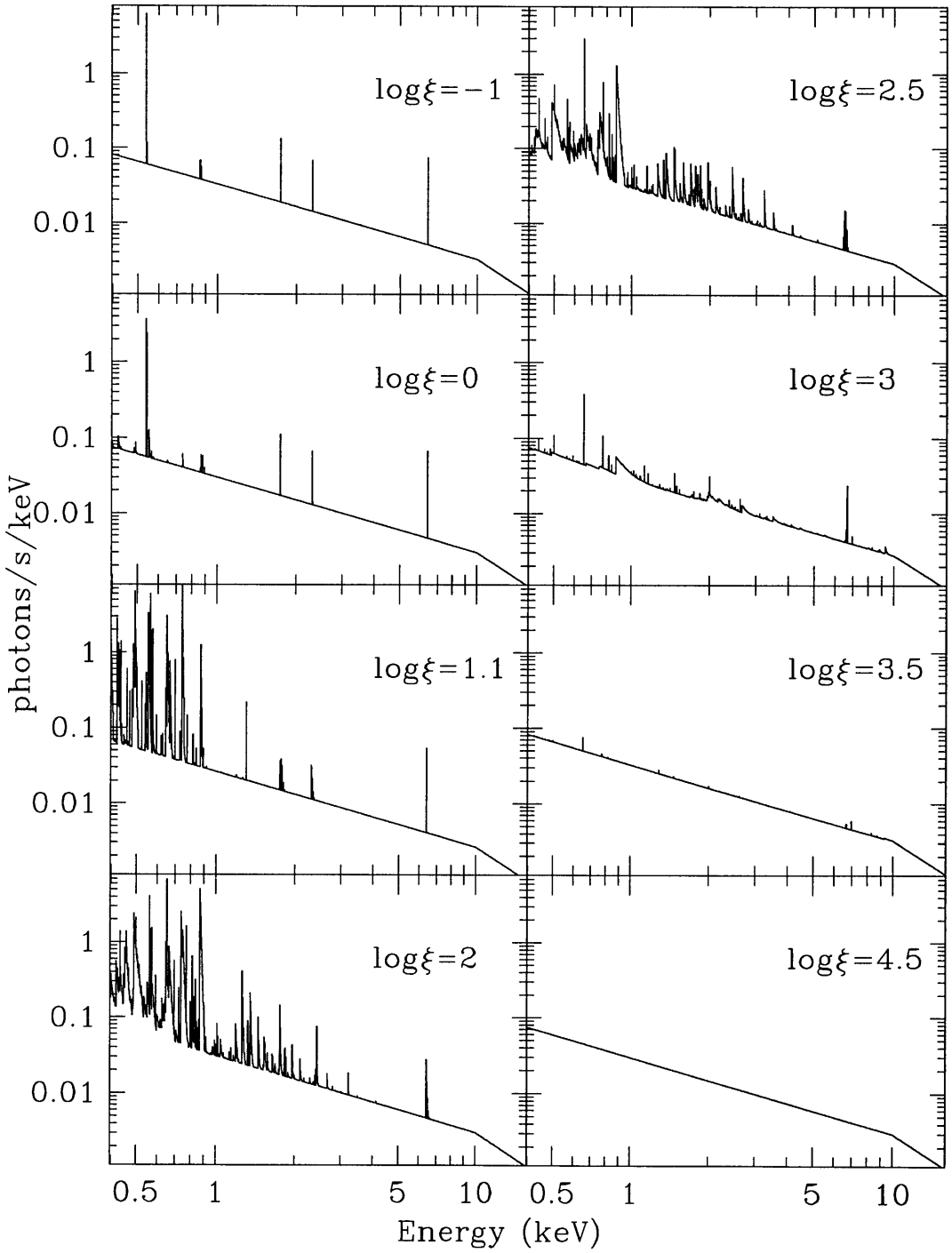

Figure 6-2: The total spectrum of reprocessed (Compton scattered, bremsstrahlung, recombination, and fluorescent) radiation for plasmas at various values of the ionization parameter plotted at 1340 bins per decade. The relative normalization is chosen such that $n^2\xi$, which determines the magnitude of the Compton scattered continuum is constant between the panels.

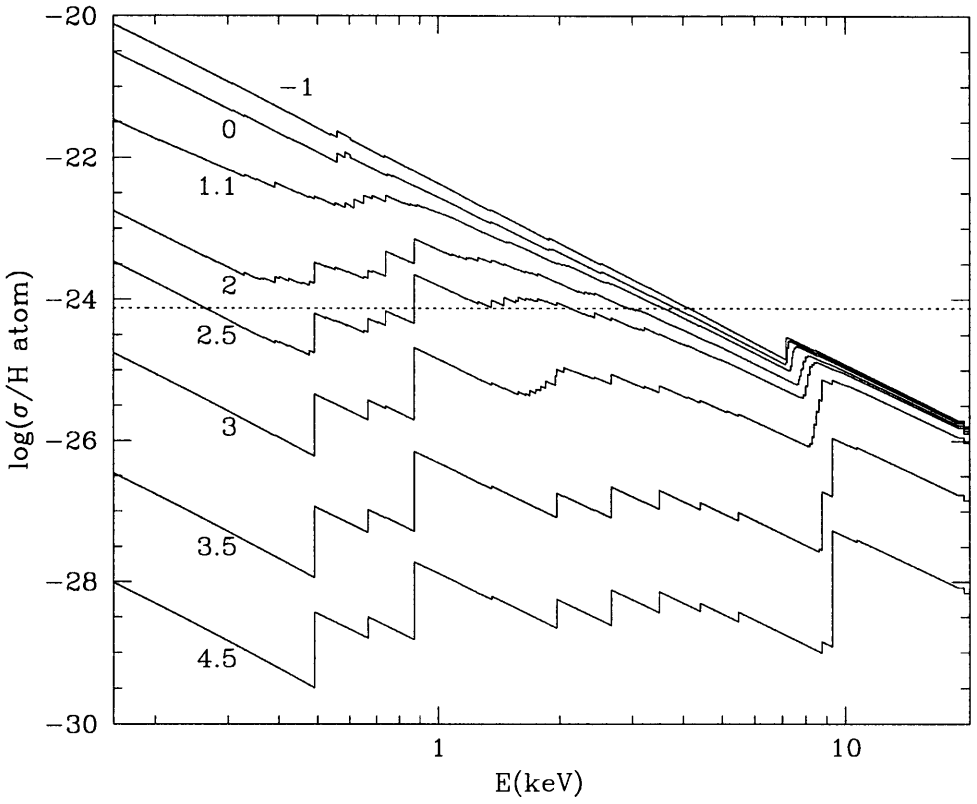

Figure 6-3: Absorption cross section per hydrogen atom for gas at various values of $\log \xi$. The dashed line is the Thompson cross-section multiplied by the number of electrons per hydrogen atom.

features may come from K shell transitions in carbon and heavier elements as well as L shell transitions in silicon and heavier elements. At values of $\log \xi$ much below 1, the metals are nearly neutral and do not undergo K or L shell transitions except by inner-shell ionization and resulting fluorescence. At $\log \xi = -1$ the only lines visible in this plot are an iron Kα lines at 6.4 keV, sulfur Kα lines at 2.3 keV, silicon Kα lines at 1.74 keV, and neon Kα lines at 0.86 keV.

In Figure 6-3 are plotted the absorption cross-sections per hydrogen atom for various ionization parameters calculated by XSTAR.

6.4 *ASCA* AND PHOTO-IONIZED PLASMAS

In order to demonstrate the capabilities of the *ASCA* SIS for diagnosing the conditions of photo-ionized plasmas, absorption by a small column (10^{21} cm^{-2}) of cold interstellar

material was applied to the spectra in Figure 6-2 and the resultant spectra were convolved with the response function for SIS 0 chip 1 in bright mode. The results are plotted in Figure 6-4 These spectra represent the spectral resolution that might be achieved in a very long exposure time. For any real observation, the quality of the data is degraded by Poisson statistics. What appears to be an emission feature at approximately 2.0 keV (but does not correspond to any emission feature in the spectral model) is an instrumental feature due to photo-electric absorption at the K edge of silicon (1.84 keV) and the M edge of gold (2.2 keV). A very slight bump can be seen in the high-ionization spectra at 1.74 keV though the input spectra have no extra emission there. The bump in the low-ionization spectra is due to silicon fluorescence in the detector plus the silicon line from the input spectrum.

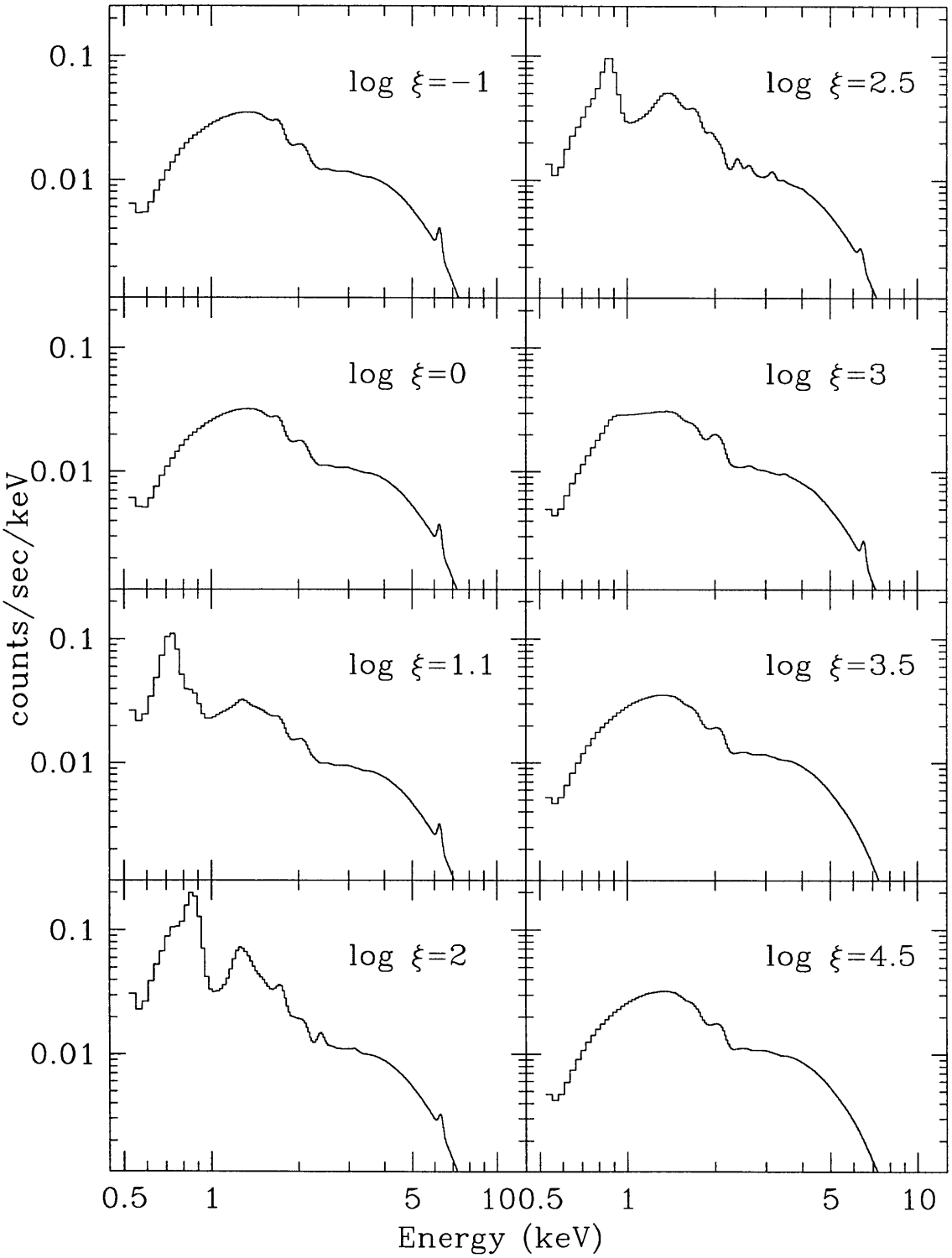

Figure 6-4: The spectra of reprocessed radiation in Figure 6-2 absorbed and folded through the SIS response.

Chapter 7

The Spectral Simulation Algorithm

In this chapter, we describe the procedure we devised to calculate the spectrum of X-rays from a central point source reprocessed in a 3-D matter distribution. The flux received by an observer at a distance d from a diffuse source can be written as

$$\mathcal{F}_\nu = \frac{1}{4\pi d^2} \int j_\nu(\mathbf{x}) e^{-\tau_\nu(\mathbf{x})} dV \tag{7.1}$$

Here, j_ν is the volume emission coefficient — the energy output of the gas per unit volume, frequency, time, and solid angle in the direction of the observer. The optical depth, $\tau_\nu(\mathbf{x})$, between the point of emission and the observer, defined by the equation

$$\tau_\nu(\mathbf{x}) = \int_{\mathbf{x}}^{\mathbf{x}_{\text{observer}}} \sigma_\nu(\mathbf{x}) n(\mathbf{x}) dx \tag{7.2}$$

where σ_ν, is the cross-section for absorption or scattering out of the line of sight per proton (neutral or ionized hydrogen atom), and $n(\mathbf{x})$ is the density of protons at position $\mathbf{x}$. A photon received by the observer is said to be "emitted" at the place where it last interacted with the gas, whether it was actually emitted or merely scattered.

In general, the emission and absorption depend on the various internal variables (density, temperature, etc.) as well as the intensity and frequency spectrum of the radiation field which it is subject to. In this procedure, it is assumed that the heat-

ing and ionization of the gas is due only to the radiation from the compact X-ray source (and not, for example, mechanical compression) and that this radiation is not significantly attenuated in the diffuse gas. Furthermore, it is assumed that the gas is optically thin along the lines from the X-ray source which are not blocked by a companion star or some other object that is assumed to be opaque. With these assumptions, for a given spectrum of X-rays from the compact object, the emission is a function of the ionization parameter $\xi = L/nr^2$ (as in Figure 6.2) scaled by n^2 and the absorption cross-section per hydrogen atom is a function of ξ only (as in Figure 6-3).

The simulations begin with a choice of the spectrum of a point source of radiation. Next, an XSTAR simulation such as described in Section 6.3 is performed to create a table of emission coefficients and absorption cross-sections as a function of ξ. To the emission coefficients from XSTAR are added the emission from Compton scattering. Next, a three-dimensional gas density distribution and is chosen. The density distribution is mapped onto a rectilinear grid such that the line of sight to the observer is parallel to one of the axes. The ionization parameter is computed at each grid point which can be connected to the compact X-ray source with a straight line which does not pass through an opaque object (such as a companion star) using the assumed luminosity L of the point radiation source, the density n at the grid point, and the distance r of the grid point from the radiation source. The integrals above are then computed over the entire volume of the density distribution using the emission and absorption coefficients from the XSTAR table. The radiation intensity emitted in the direction of the observer is computed by summing the emission over the grid points, attenuated in intermediate grid points along the line of sight. The computation begins at a grid point on the far side of the gas distribution relative to the observer and proceeds in the direction of the observer. At each grid point, absorption from the current grid point is applied to the summed emission from the previous grid points and then emission from the current grid point is added to the running total emission. The total emission from each column is summed to determine the total radiation intensity. Emission is assumed to come only from gas which is illuminated by the point radiation source. Absorption in unilluminated material

is taken to be equal to absorption from gas with the lowest ionization parameter in the XSTAR table. Emission from points of gas which are not visible to the observer (such as those which are behind the normal star in an X-ray binary) is not included in the summation. This algorithm is described graphically in Figure 7-1. The C code which was used to carry out the summation of the flux is included in Appendix B.

The specific flux received by an observer is equal to the specific intensity emitted by the gas divided by 4π times the distance squared. The specific intensity is thereby converted to a flux using some fiducial distance and this flux is output to a FITS format XSPEC Table Model (Arnaud 1995). The XSPEC table model allows a model for the flux to be easily imported to the XSPEC spectral fitting program (Arnaud 1996). With the XSPEC program, spectral models can easily be convolved with instrument response matrices for comparison with observed spectral data and the values of χ^2 determined as measures of the fits for particular models of the density distribution and source spectrum and luminosity. In XSPEC, the distance to the source can be adjusted with the model normalization parameter. If spectra are computed for a range of wind models, elemental abundances, or input spectra, the best fit model can be determined.

This algorithm is particularly well suited to the study of eclipsing X-ray binary pulsars in circular orbits. Pulse timing of the X-ray pulsar and Doppler spectroscopy of the companion star can yield precise information on the geometry of the system. If the orbit is circular, then in a frame that co-rotates with the orbit, the system is quasi-static. By observing at different orbital phases, one can view the same system from a range of directions, a luxury not often available in astrophysics. If the system eclipses, the direct radiation can be measured while the system is uneclipsed and the reprocessed radiation can be observed independently of the direct radiation during eclipse.

Clearly, the assumption that the radiation from the compact object is not significantly attenuated may cause an overestimate of the radiation from material with significant optical depth. The cross-sections plotted in Figure 6-3 are of order as large as $10^{-21}\mathrm{cm}^2$ per hydrogen atom. Therefore, this algorithm will begin to be-

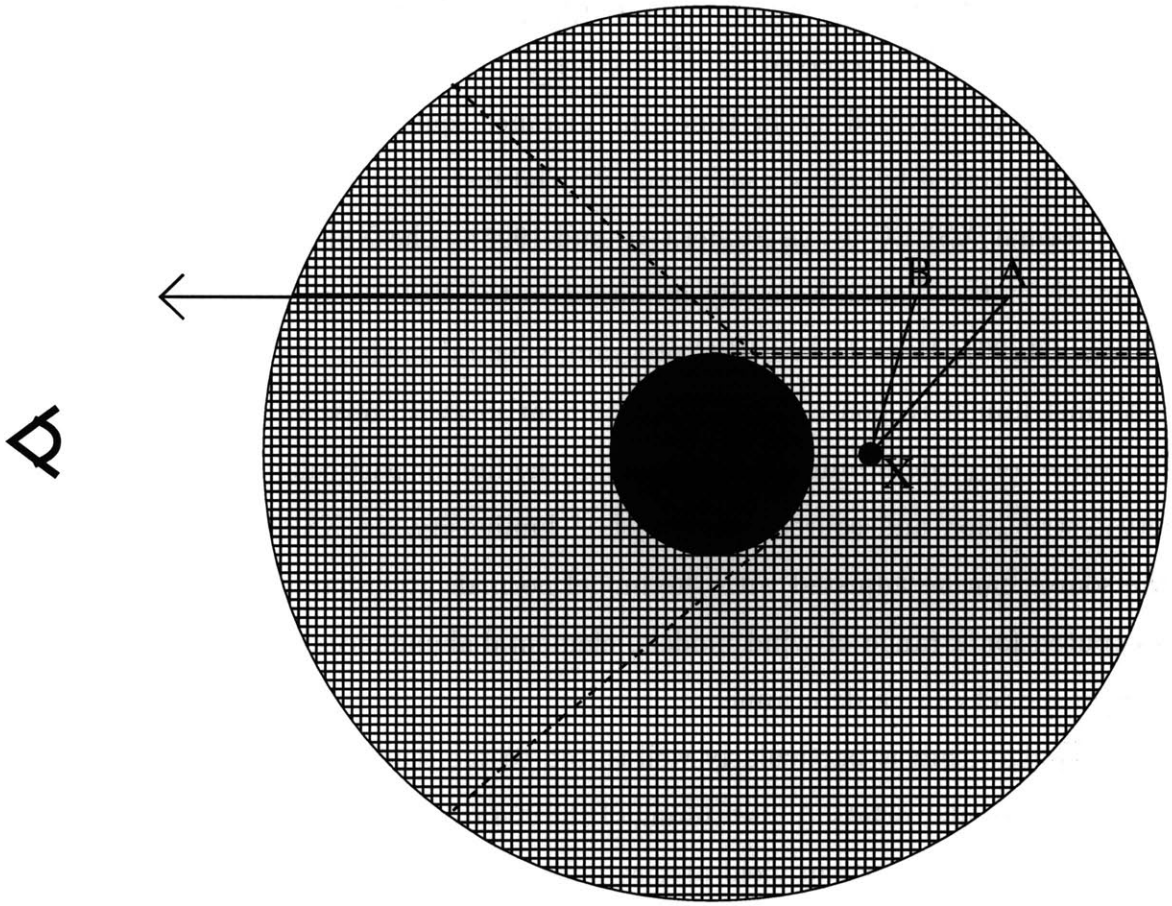

Figure 7-1: The spectral simulation algorithm is illustrated here. The X-ray source is the small dark circle labeled "X". The emission at point A is taken to be that of the zone from the XSTAR simulation with the same ionization parameter as at A; $\xi = L/nr^2$, where L is luminosity of the X-ray source at X, n is the density at A, and r is the length of the path $\overline{XA}$; absorption along the path $\overline{XA}$ is not considered. Absorption of the reprocessed radiation from A in cells along the line of sight to the observer (such as B) is calculated. The absorption at B is taken to be a function of ξ at B. Dashed lines indicate the X-ray shadowed region and the eclipsed region.

come invalid for column densities of order $10^{21}\mathrm{cm}^{-2}$ or greater. The fact that this algorithm does consider absorption of the reprocessed radiation on its way from the reprocessing sites to the observer does help significantly however. Consider a uniform clump of matter with large optical depth. The only reprocessed radiation that will be seen from such a clump is from the part of its surface which is both exposed to the radiation source and visible to the observer. This algorithm would find emission from the entire volume of the clump. However, since the clump is optically thick, all of the radiation calculated to be produced inside the clump except for a thin region along the surface of the clump will be absorbed before exiting the cloud and will therefore, not contribute to the total simulated spectrum. This algorithm would not be accurate in a situation in which there is a large amount of optically thin gas but where the radiation source is surrounded by a small, nearby region of optically thick gas. In this case, the algorithm would calculate emission from a large amount of gas which was actually shadowed by the dense shell. However, if the optically thick material does not subtend a large solid angle about the radiation source, the error due to shadowing of the thin material by thicker material should be small. In regions where the density is so high that single pixels are optically thick, the neglect of absorption by material within the same pixel in which it was produced, will cause the emission from those optically thick pixels to be overestimated by approximately the optical depth of the pixels. If the optically thick material subtends only a small solid angle from the radiation source and is not optically thick on length scales much less than one pixel, the algorithm should calculate the spectrum accurately except that the emission from the dense material will be overestimated by a factor of no more than a few. The effect of absorption for densities and path lengths similar to those found in the Blondin & Woo (Blondin & Woo 1995) hydrodynamic model are explored in Chapter 8.

Chapter 8

Spectral Simulations and Comparison to Data

8.1 *ASCA* Spectra

An uneclipsed spectrum of SMC X-1 was obtained from *ASCA* observation 1 and an uneclipsed spectrum from *ASCA* observation 2. The beginning of the decline in flux at the end of this observation seen with the GIS detectors (Figure 5-4), was observed with SIS detectors and the data after phase 0.5, where the SIS count rate began to decline was rejected. The resulting exposure times for the spectra are 17,226 seconds for SIS0 and 17,026 seconds for SIS1. Spectra were extracted from the entire time of observation 2 though the observation extends beyond the time of nominal eclipse. Since that observation occurred during a low state when, as we have demonstrated, the neutron star is occulted by the accretion disc, the X-rays detected out of eclipse during that observation were also reprocessed in the stellar wind. To further improve the signal-to-noise ratio, the energy channels, which oversample the detector resolution, were grouped so that each channel has at least 50 counts.

Due to the high count rate in the uneclipsed observation, the statistical errors due to counting statistics were small compared to the systematic errors due to the instrument calibration. For this reason, only the data from the SIS0 detector, which may be better calibrated, were used in spectral fits for this observation. The spectrum

derived from the uneclipsed observation was well fit by a model which consists of a power-law plus two broad Gaussian components — one near 0.9 keV and one near 6 keV — absorbed by a small column of cold interstellar material. The specific form of the model for the photon flux is given by

$$\mathcal{F}(E) = e^{-\sigma(E)N_{\rm H}}[f_{\rm pl}(E) + f_{\rm ga1}(E) + f_{\rm ga2}(E)] \times \begin{cases} 1 & E \leq 10{\rm keV} \\ \frac{E-10{\rm keV}}{15{\rm keV}} & E > 10{\rm keV} \end{cases} \tag{8.1}$$

where

$$f_{\rm pl}(E) = K_{\rm pl}(E/1keV)^{-\alpha} \tag{8.2}$$

$$f_{{\rm ga}i}(E) = \frac{K_{{\rm ga}i}}{\sigma_i\sqrt{2\pi}} \exp \frac{-(E-E_i)^2}{2\sigma_i^2} \tag{8.3}$$

and $\sigma(E)$ is the cross-section of interstellar absorption of Morrison & McCammon (1983). While the *ASCA* detectors are not sensitive to the high energy cut-off, it has been measured with *Ginga* (Woo et al. 1995a) and is included here for consistency with the XSTAR calculations. The observed spectra and best fit model are plotted in Figure 8-1. Though they were not used in the spectral fits, the data from the SIS1 detector are included in this plot. There appears to be a discrepancy between the two detectors near 1.3 keV but this discrepancy is comparable to the channel-to-channel variations in observations of the supernova remnant 3C273 (Orr et al. 1998) which were used for calibration. The best fit values of the parameters for this and the two fits described below are tabulated in Table 8.1. Approximately the same result was obtained by Stahle et al. (1997) for this data set. The fitted value for the column of neutral hydrogen is of the same order of magnitude as values obtained for the position of SMC X-1 by extrapolation from neighboring points in 21-cm emission surveys: 4.6×10^{20} cm^{-2} for a galactic survey with 1° resolution (Dickey & Lockman 1990) and 4.5×10^{21} cm^{-2} for a survey of the SMC with 98″ resolution (Stanimirovic et al. 1998). The flux of this model spectrum in the 13.6 eV–13.6 keV band (the band in which luminosity is defined in XSTAR) is 6.44×10^{-10} erg cm^{-2}s^{-1}. For isotropic emission, this corresponds to a luminosity of 1.9×10^{38} erg/s. A source with this spectrum

would give an on-axis count rate of 1.1 counts/second[1] in the *RXTE* All-Sky Monitor whereas the observed count rate of SMC X-1 in the All-Sky Monitor, at the peak of the high state is approximately 3 counts/sec (Figure 5-1) which implies that the luminosity of SMC X-1 in the high state is approximately 5×10^{38} erg/s.

In the eclipse observation, the systematic calibration errors are much smaller than the statistical errors due to the low count rate. Therefore, spectral models were fit simultaneously to both the SIS0 and the SIS1 detectors. To fit the spectrum derived from the observation during eclipse, the same model that fit the out-of-eclipse data, scaled down in intensity, was tried. This is the spectrum that would be expected if the intrinsic spectrum of the accreting neutron star did not change between the two observations and the eclipse spectrum were due only to Thompson scattering of the X-rays from the source. Relative to the rescaled, best fit uneclipsed spectrum, the eclipse data show a large excess at energies greater than 4 keV and a small, narrow excess near 1.8 keV, the approximate location of the fluorescence line of nearly-neutral silicon (Figure 8-2). An acceptable fit for the eclipse data can be obtained by allowing the parameters of the broad 6 keV feature to vary from their values scaled from the uneclipsed spectrum (Figure 8-3).

A separate fit to the data points in the 1.5–2.0 keV range was done using a power law continuum and a narrow emission feature. The energy of this emission feature was found to be 1.775 ± 0.020 keV and the flux was $1.5 \pm 0.5 \times 10^{-5}$ photon $s^{-1} cm^{-2}$. Though this feature is near the location of the detector's fluorescence peak, it is probably real. The SIS0 screened event list has 4769 photons with energies greater than 1.84 keV. If the fluorescence event probability is 1%, approximately 50 fluorescence events should have occurred during that observation. A line flux of 1.5×10^{-5} photon $s^{-1} cm^{-2}$ corresponds to 74 photons in this spectrum. A miscalibration of the probability of fluorescence events of order 100% would be necessary to result in a spurious detection of this magnitude. Furthermore, in the data from the uneclipsed observation, in which the source has nearly the same spectrum, there is no deviation from the smooth

[1]This count rate was computed by comparing the model flux to the flux of the Crab (Toor & Seward 1974) in each of the 2–3, 3–5, and 5–10 keV bands and assuming that the count rate of the Crab is 25 counts/second in each of these bands.

	Uneclipsed	Eclipsed	
$n_H(10^{20}cm^{-2})$	7.0(1.0)	7.0(frozen)	7.0(frozen)
α	0.94(0.02)	0.94(frozen)	0.94(frozen)
$K_{\rm pl}$	$2.67(0.07) \times 10^{-2}$	$4.9(0.1) \times 10^{-4}$	3.77(0.20)
E_1(keV)	0.93(0.04)	0.93(frozen)	0.93(frozen)
σ_1	0.16(0.03)	0.16(frozen)	0.16(frozen)
$K_{\rm ga1}$	3.4(0.9)	6.1×10^{-5} (tied to $K_{\rm pl}$)	4.3×10^{-5} (tied to $K_{\rm pl}$)
E_2	6.0(0.1)	6.0(frozen)	6.8(0.3)
σ_2	1.0(0.2)	1.0(frozen)	2.0(0.3)
$K_{\rm ga2}$	$2.2(0.8) \times 10^{-3}$	3.9×10^{-5} (tied to $K_{\rm pl}$)	$5.1(0.7) \times 10^{-4}$
χ^2/d.o.f.	70/62	376/141	139/138
probability	21%	$< 10^{-32}$	46%

Table 8.1: Best fit spectral parameters and 1-sigma errors.

spectral model at this energy. Still, a detection of this feature by an instrument not susceptible to this fluorescence effect would be reassuring.

8.2 Single Zone Spectra

XSTAR runs similar to those described in Section 6.3 were made — gas density equal to 10^{-3}cm^{-3} with 100 zones, equally spaced in $\log \xi$ from 7 to -1. The spectrum of input radiation was taken to be the model used to fit the *ASCA* observation out of eclipse with the column of absorbing material set to zero. Five runs were made with metal abundances equal to solar, 0.316, 0.1, 0.0316, and 0.01 of solar. Similar runs were also done with $\log \xi$ in the range 5 to -3. Before adding the spectra of reprocessed emission from the many zones of these XSTAR calculations as described in the spectral simulation algorithm, the eclipse spectra were first compared to the spectra of reprocessed emission from single zones — i.e. model spectra of reprocessed emission from material at single ionization parameters.

The high-energy excess in the eclipse spectrum cannot be produced by any of the emission processes considered in this work (i.e. not by bremsstrahlung or by a recombination continuum and certainly not by fluorescence or recombination line emission). It may be due to a very highly absorbed component ($n_H \sim 10^{23}$ cm^{-2}).

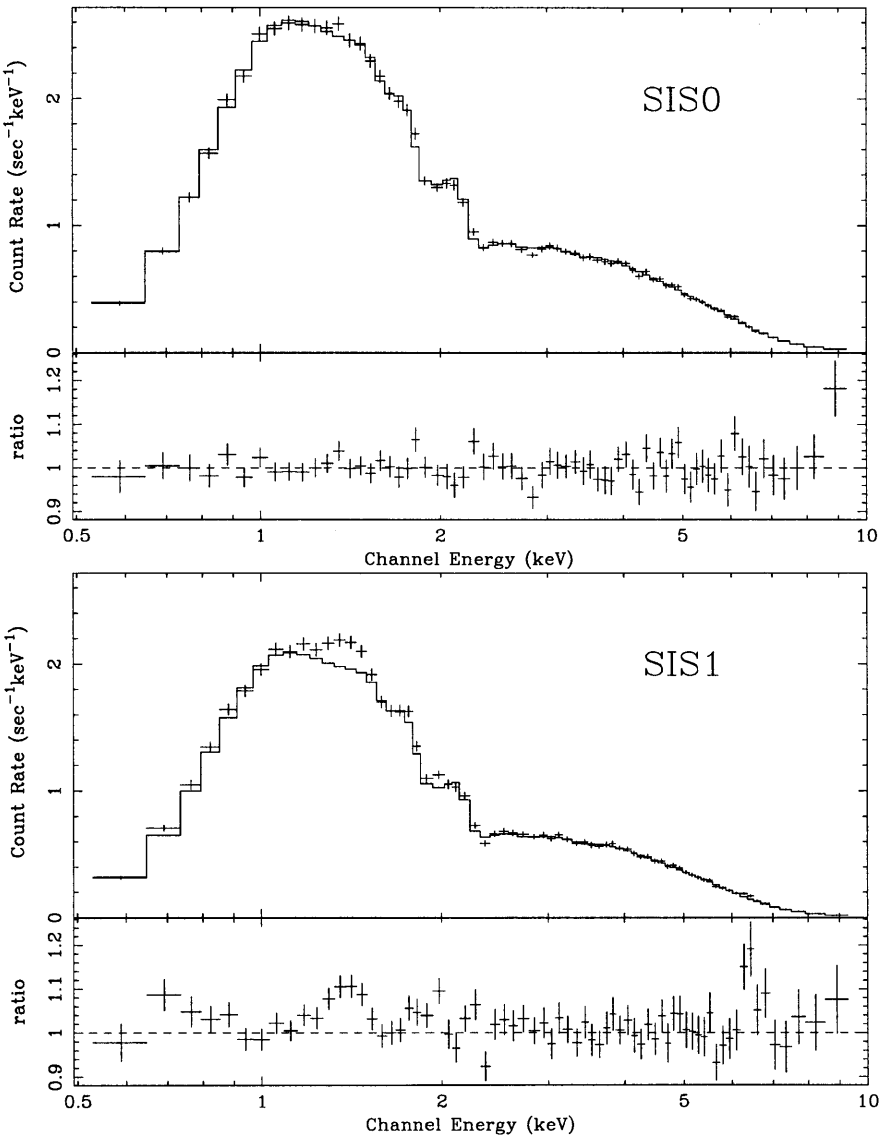

Figure 8-1: Spectrum of SMC X-1 out of eclipse as measured by the two SIS detectors. The data points are marked by a crosses and an empirical spectral model (Equation 8.1, Table 8.1) convolved with the response functions of the instruments is plotted with histograms.

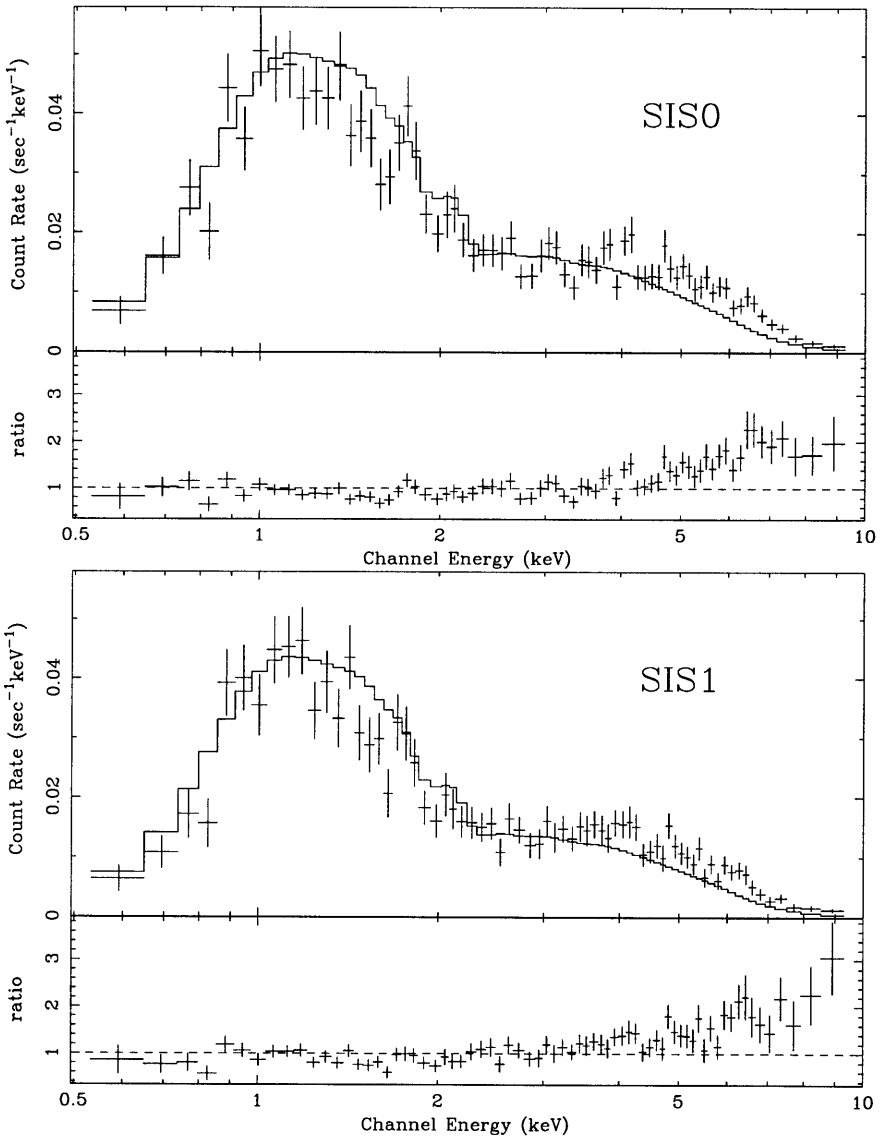

Figure 8-2: Eclipse Spectrum of SMC X-1 with the rescaled spectral model from the uneclipsed spectrum. This is the spectrum that would be expected for pure Thompson scattering.

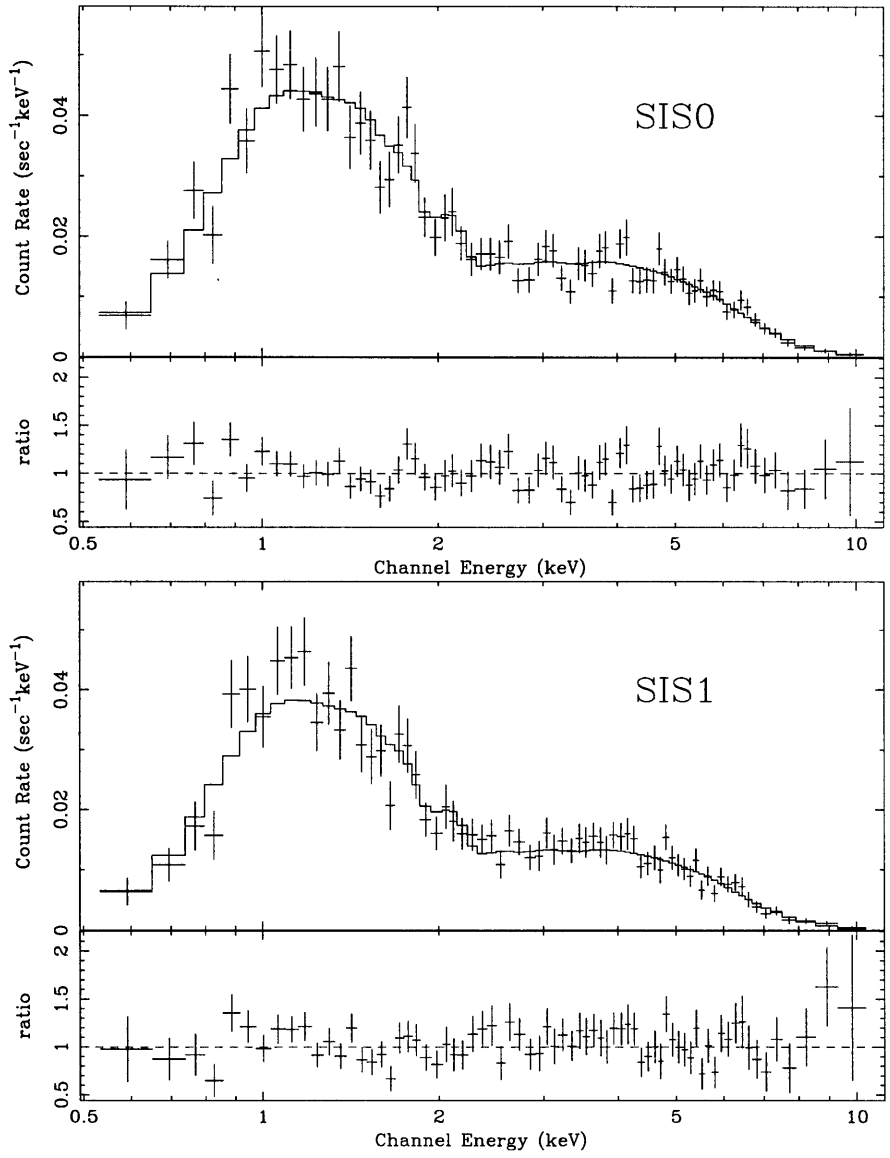

Figure 8-3: The eclipse spectrum of SMC X-1. The parameters of the 6 keV broad Gaussian component of the spectral model have been allowed to vary. This allows the spectrum above 4 keV to be fit.

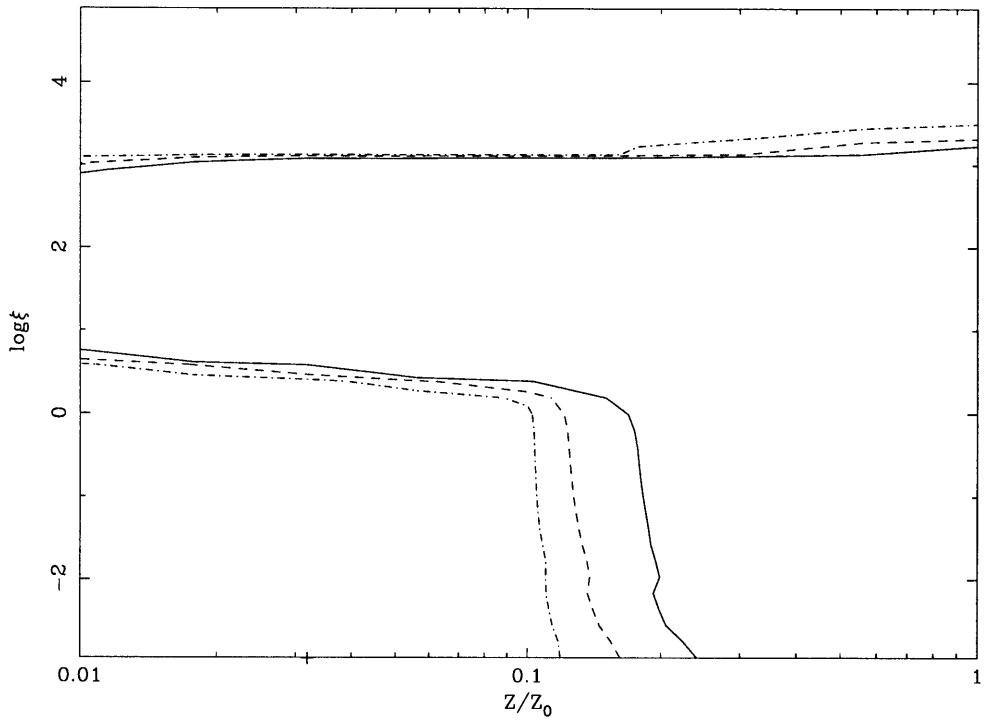

Figure 8-4: Contours of χ^2 for fits of the eclipse spectrum to single zone models. The eclipse spectrum can be fit by single zone models with $\log \xi$ greater than approximately 3 (top) and by single zone models with $\log \xi$ approximately 1 and with metal abundances less than approximately one-tenth of solar (bottom left). The contours mark $\Delta\chi^2$ =2.3 (dot-dash), 4.61 (dash), and 9.21 (solid) from the best fit (marked with "+") which has $\chi^2 = 112$ with 85 degrees of freedom.

However, it may also be due to a variation in the intrinsic X-ray spectrum of the neutron star and lacking a better understanding of this component, the data from energy channels above 4.0 keV is neglected in the fits to X-ray reprocessing models described in this chapter.

The eclipse spectrum of SMC X-1 was compared to the single zone model spectra, over the range of ionization parameter and abundance. Absorption by a fixed column of interstellar matter equal to that obtained for the uneclipsed spectral fit ($7 \times 10^{20}\mathrm{cm}^{-2}$) was applied to the model spectra and the normalization of the spectral models was allowed to vary to fit the data. The eclipse spectra can be fit by single zone spectral models with $\log \xi \gtrsim 3$ or by models with $\log \xi \lesssim 1$ and metal abundance less than approximately 1/10 of solar (Figure 8-4). The spectrum of reprocessed emission with $\log \xi$ between 1 and 3 contains a large number of strong emission lines and

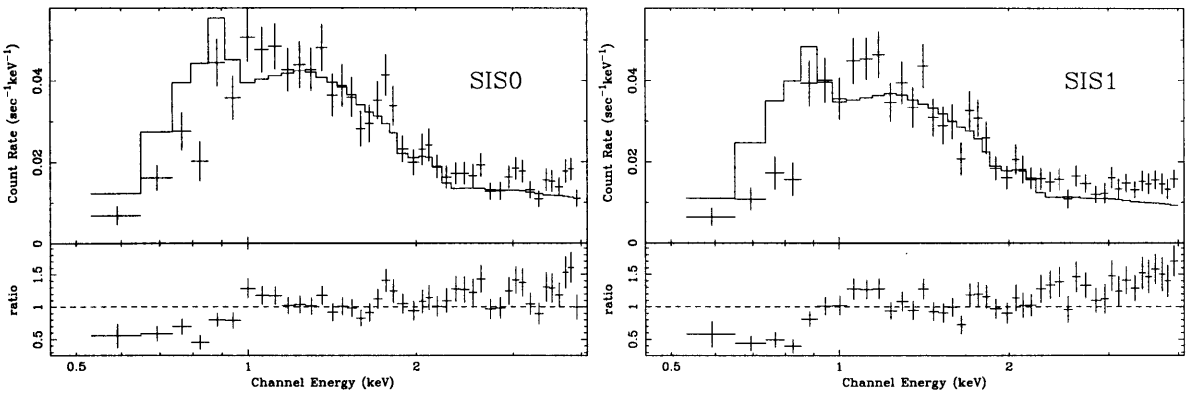

Figure 8-5: Observed eclipse spectrum (crosses) and single zone model with $\log \xi = 1.8$ and $Z/Z_{\odot}$=0.01 (histogram). Even at this very low abundance, the spectrum of reprocessed emission from gas at intermediate ionization parameter contains a recombination feature below 1 keV, due mostly to oxygen, that is excluded by the data. $\chi^2 = 281$ for 85 degrees of freedom.

narrow continua from recombination (Figures 6-2 & 6-4) which produce a large flux below 1 keV which is not present in the eclipse spectrum. In the range $1 < \log \xi < 3$, even for a metal abundance as low as 1/100 of solar, the calculations predict a flux below 1 keV from recombination features that is excluded by the observed spectrum (Figure 8-5). For $\log \xi > 3$ recombination is very weak relative to Thompson scattering so the spectrum is insensitive to metal abundance and so satisfactory fits may be obtained for abundance as large as solar (Figure 8-6). For $\log \xi < 1$, good fits are obtained because the material is not highly ionized enough to produce recombination in the ASCA band and the spectrum is dominated by the Thompson continuum (Figure 8-7). In contrast to the $\log \xi > 3$ regime however, the spectrum of reprocessed X-rays contains fluorescent emission lines.

The emission line detected at 1.775 ± 0.020 keV may be the fluorescent Kα line of Si II (neutral before inner shell ionization) or some combination of this line and the fluorescent Kα lines of Si III–V all of which have Kα lines at 1.74 keV. It may also be due, in part or whole, to a higher ion, such as Si VIII which has a fluorescent Kα line at 1.77 keV. The feature cannot be due to recombination to helium-like silicon (which would produce an emission line at 1.84 keV) because under conditions necessary to produce that line, recombination radiation from oxygen and other elements would produce a large flux below 1 keV which is not seen. The presence of this fluorescence

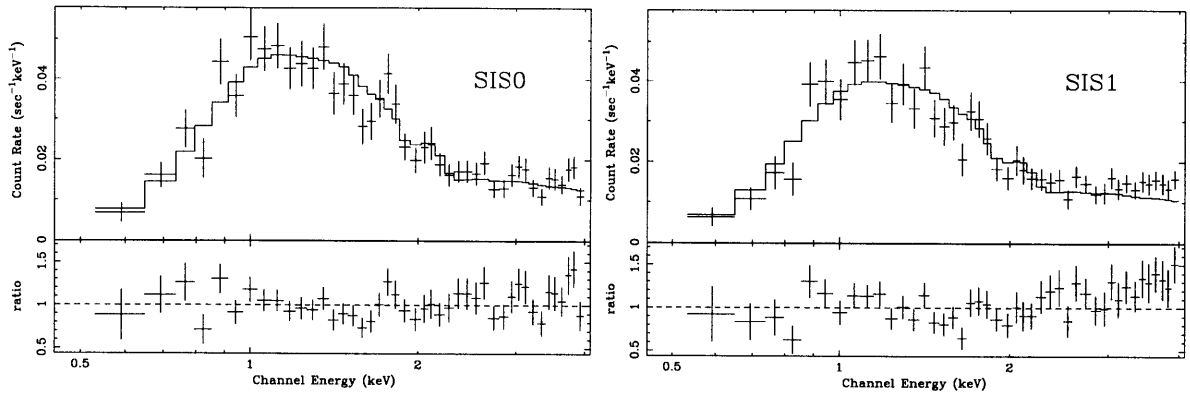

Figure 8-6: Observed eclipse spectrum and single zone model with $\log \xi = 4.0$ and $Z/Z_\odot = 1.0$. The spectrum of reprocessed emission at large ionization parameter is due almost completely to Thompson scattering. The observed spectrum is consistent with this model spectrum except for a silicon fluorescence feature near 1.74 keV apparent in the data. spectrum. $\chi^2 = 113$ for 85 degrees of freedom.

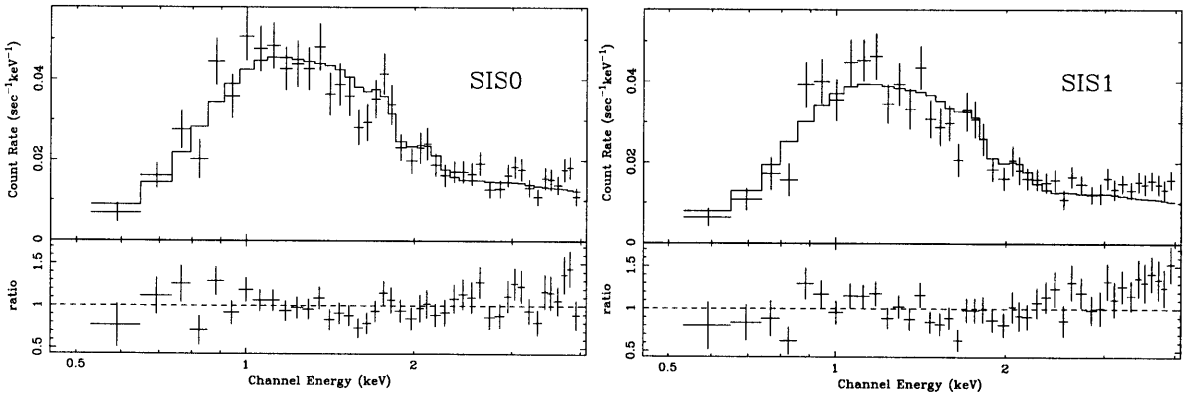

Figure 8-7: Observed eclipse spectrum and single zone model with $\log \xi = 0$ and $Z/Z_\odot = 0.1$. The spectrum of reprocessed emission at small ionization parameter is due to Thompson scattering plus fluorescence. This model contains the feature near 1.74 keV that appears in the data. $\chi^2 = 114$ for for 85 degrees of freedom.

line and the lack of strong recombination features indicate that a significant fraction of the emission comes from gas with $\log \xi < 1$. The single zone spectral model with $\log \xi = 0$ and metal abundance equal to one-tenth of solar has a single emission line at 1.740 keV. With the model normalization fit to the SMC X-1 eclipse spectrum, this line has a flux of 5.2×10^{-6} photon $s^{-1}cm^{-2}$. The flux of the observed feature is $1.5 \pm 0.5 \times 10^{-5}$ photon $s^{-1}cm^{-2}$.

Except in the range $1 < \log \xi < 3$, the flux from the reprocessing models is dominated by Thompson scattering. As such, the emission measure (n^2V) necessary to reproduce a given luminosity with a single zone reprocessing model should be proportional to the inverse of the ionization parameter. To confirm this, the best-fit value of χ^2 was computed on a grid of values of $\log \xi$ and the normalization parameter ($K \equiv (n^2V/4\pi D^2) \times 10^{-14}cm^5$). Contours from these fits are plotted in Figure 8-8. Indeed, the best fits are in a narrow region of parameter space around the line defined by ($K\xi = 1.7$).

To determine what amount of material with $1 < \log \xi < 3$ is allowed by the observed spectra, fits were done to model spectra consisting of two single zone models. Both of the single zone models had metal abundances fixed at one tenth of solar. The first component had an ionization parameter fixed at the the lowest calculated value ($\log \xi = -2.95$). The ionization parameter and the normalization of the second component were stepped through a grid of values and the normalization of the first component was varied to minimize χ^2. Contours of the minimized $\Delta\chi^2$ relative to the best fit are plotted in Figure 8-9. As noted above, model spectra for $\log \xi > 3$ and for $\log \xi < 1$ have the same shape as the reprocessing is dominated by Thompson scattering at almost all energies. For these values of the ionization parameter, good fits can be obtained for normalizations up to a value such that $K\xi \sim 1.7$ as above. For $1 < \log \xi < 3$ however smaller normalizations are allowed. For $\log \xi = 2$, $K \lesssim 3 \times 10^{-4}$. For a distance of 50kpc, this corresponds to an emission measure $n^2V \lesssim 9 \times 10^{57}$.

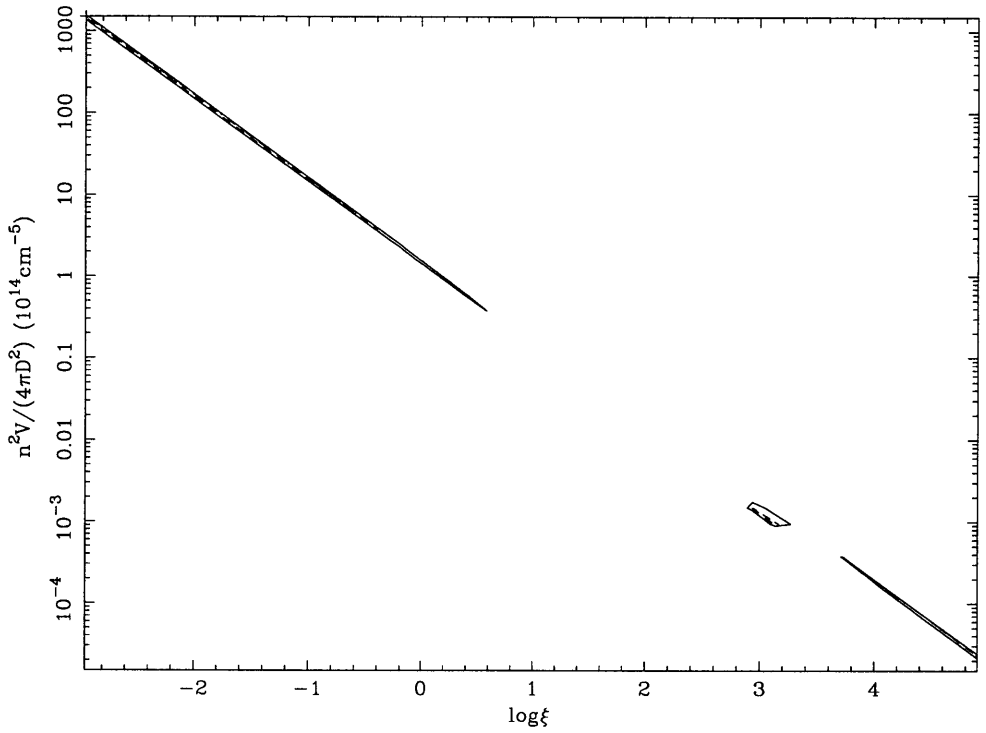

Figure 8-8: Confidence contours of ξ and the normalization K for the single zone fits to the eclipse spectrum. In the region where good fits can be obtained, K is proportional to the inverse of ξ as expected for Thompson scattering. The solid contour marks $\Delta\chi^2 = 100$ relative to the best fit (marked by "+").

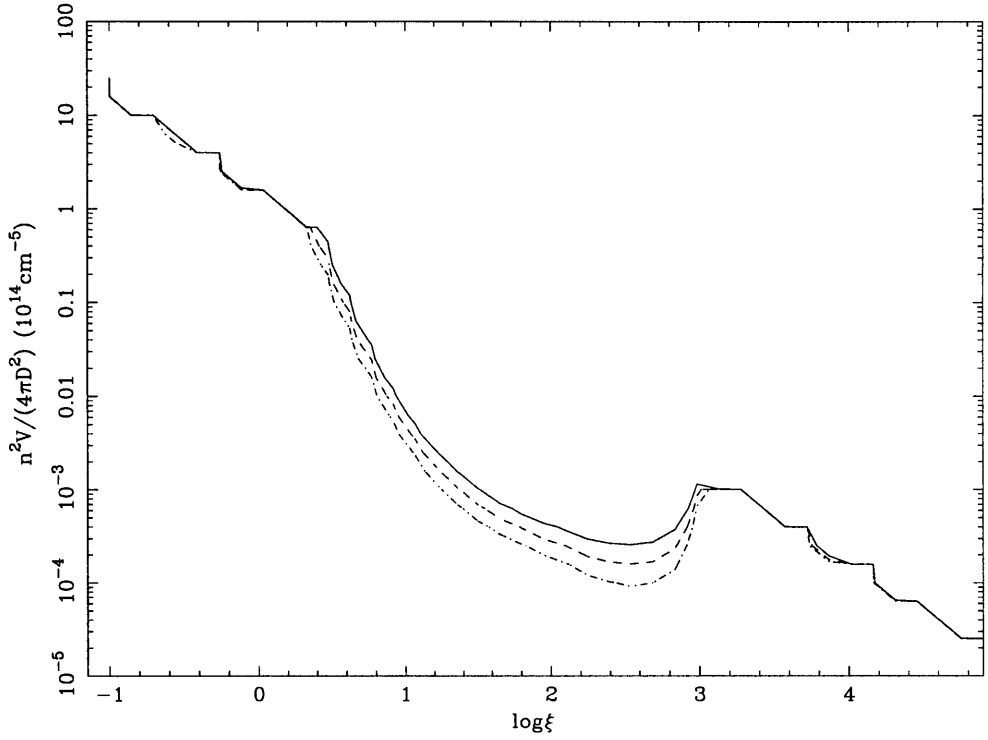

Figure 8-9: Upper limits on gas at intermediate ionization parameter in SMC X-1. A spectral model consisting of two single zone components was fit to the eclipse spectrum. The abundances for both components were fixed at one-tenth of solar abundance. The ionization parameter of the first component was fixed at $\log \xi = -2.95$ and it normalization was allowed to vary. The ionization parameter and normalization of the second component were stepped along the values in the plot. Contours of $\Delta\chi^2$ for a K and $\log \xi$ of a second component. The contours mark $\Delta\chi^2$ =2.3(dot-dash), 4.6(dash), and 9.2(solid) relative to the best fit (marked by "+").

8.3 Spectra From Reprocessing in Model Winds

8.3.1 Hydrodynamic Simulation

The spectrum of reprocessed emission the wind in the Blondin & Woo (1995) hydrodynamic simulation was synthesized using the algorithm described in Chapter 7. The density distribution on the spherical grid from the hydrodynamic simulation was interpolated onto a rectilinear grid with similar resolution: 50 grid steps along the radius of the simulation; 1.43×10^{11}cm per pixel. Points in the hydrodynamic simulation had densities no larger than approximately $3 \times 10^{11}\mathrm{cm}^{-3}$ so no pixel had an optical depth significantly greater than 1. Therefore, the overestimate of the contribution from dense regions should not have been greater than a factor of a few. While the gas distribution does have regions of high density near the radiation source, the high density material subtends a small angle in the orbital plane and is mostly confined to the orbital plane so the error in the simulated spectra due to this gas should not be large. The spectral simulation was carried out for X-ray luminosities of 1, 1.7, 3, 6, 10, 17, and 30 times 10^{38}erg/s for metal abundances relative to solar equal to 0.01, 0.0316, 0.1, 0.316, and 1. The distribution of ξ in this model is shown in Figure 8-10 for an X-ray luminosity equal to 3×10^{38} erg/s.

The SMC X-1 eclipse spectrum was fit by interpolation on this grid of models. With the distance to SMC X-1 fixed at 50 kpc, reasonable fits are obtained for the luminosity in narrow range around 6.4×10^{38} erg/s and for abundances less than a few hundredths of solar (Figure 8-11). Though a reasonable fit to the global spectrum can be obtained (Figure 8-12), the lack of a silicon line in the model spectrum indicates that the model is deficient. Furthermore, the best fit metal abundance is very low compared to other measurements of the abundances in the SMC (Westerlund 1997). Both the reason for the low abundance and for the lack of the silicon feature can be seen in the differential emission measure, plotted in Figure 8-13. For an X-ray luminosity of 6×10^{38} erg/s, the hydrodynamic simulation contains gas with $\log \xi > 3$ and also some gas with $1 < \log \xi < 3$ but no gas with $1 < \log \xi < 3$. Only because not all of the gas has $1 < \log \xi < 3$ can adequate fits be obtained with even the lowest

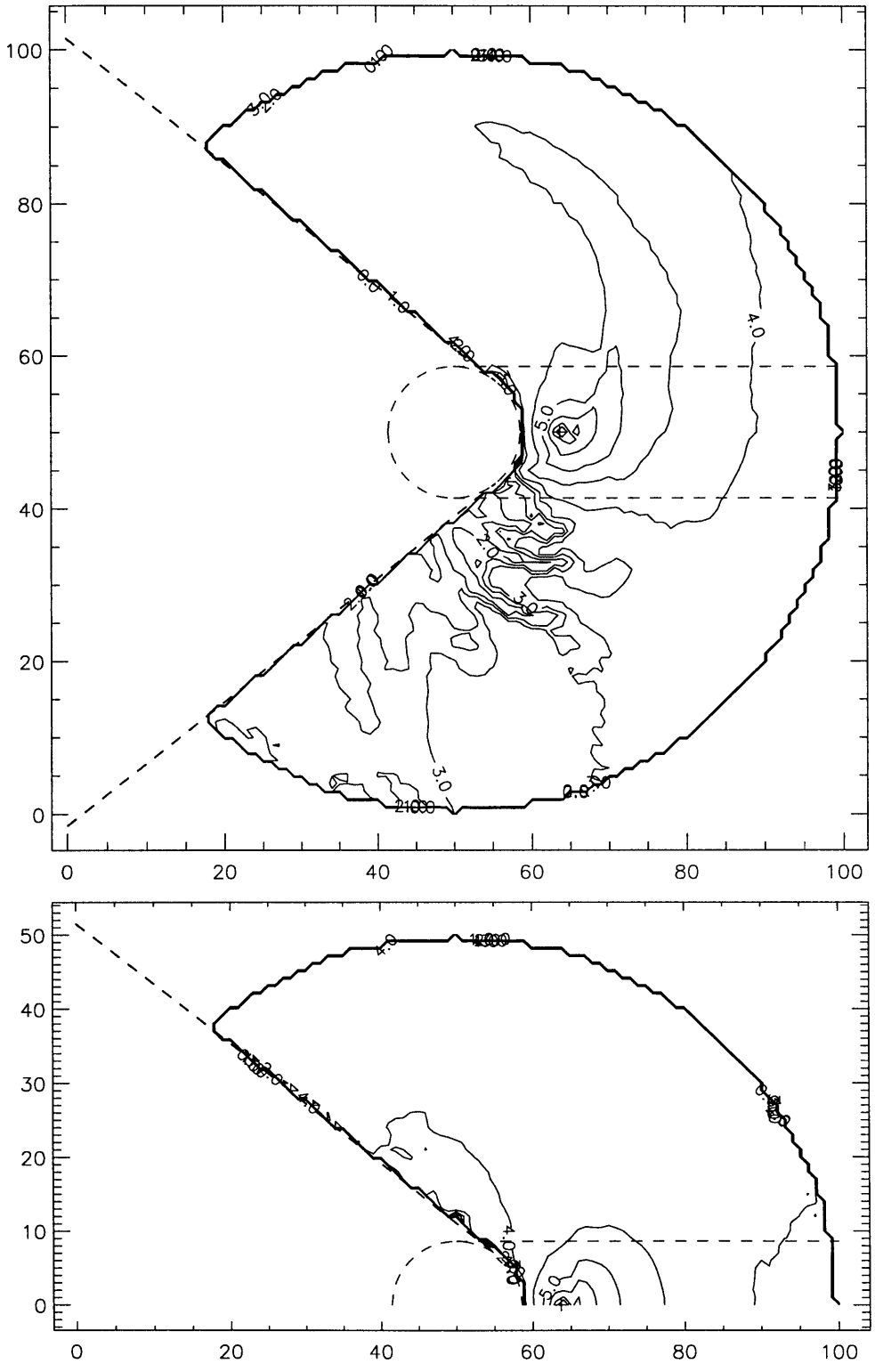

Figure 8-10: Contours of $\log \xi$ in the orbital plane (above) and the plane perpendicular to the orbital plane and including the compact object (below) for the hydrodynamic simulation of Blondin & Woo (1995).

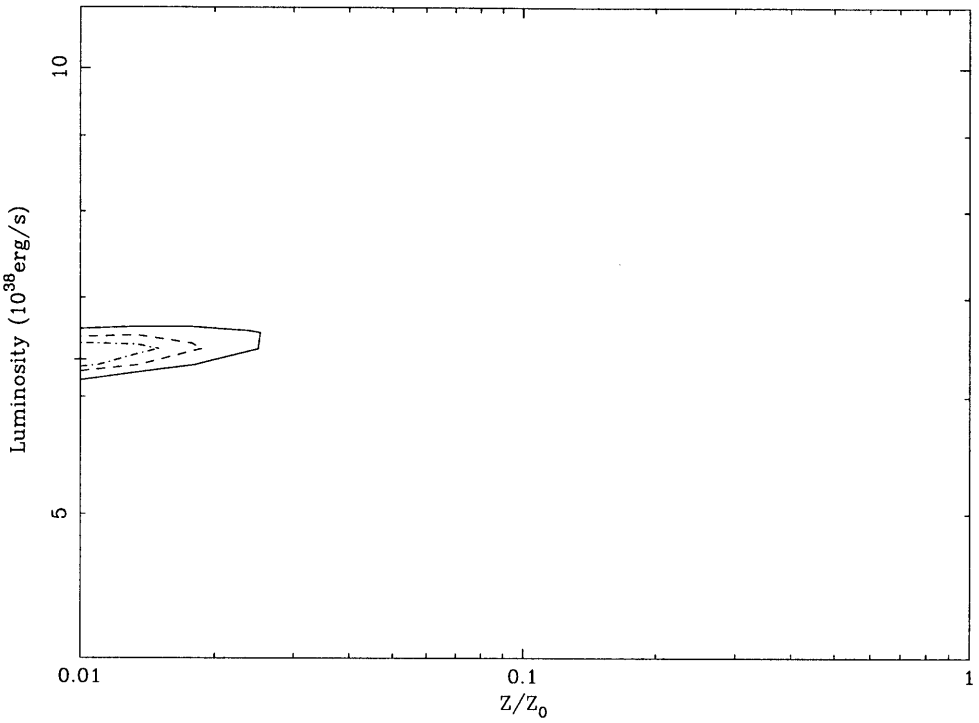

Figure 8-11: Contours of fit for the spectral simulation of the hydrodynamical simulation. The contours mark $\Delta\chi^2$ =2.3 (dot-dash), 4.61 (dash), and 9.21 (solid) from the best fit (marked with "+") which has $\chi^2 = 111$ with 86 degrees of freedom.

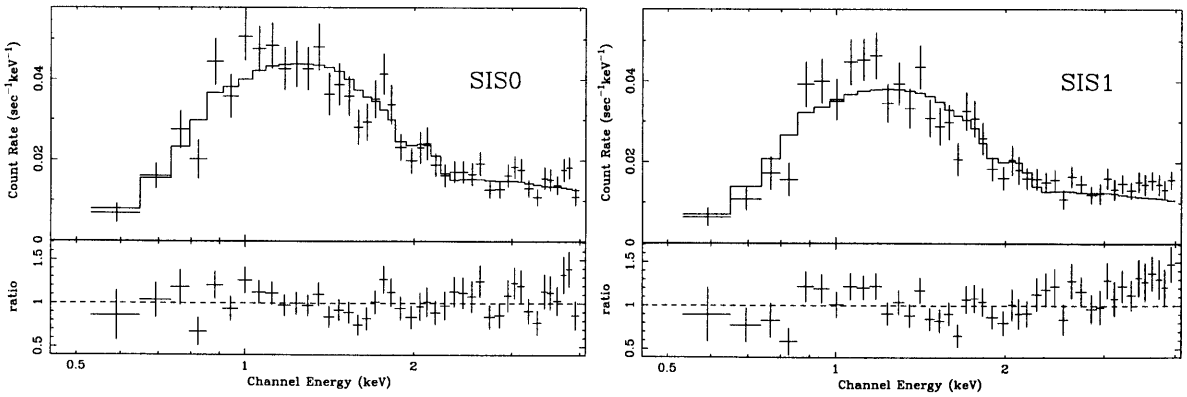

Figure 8-12: Best fit synthetic spectrum for the hydrodynamic simulation (L_X = 6.4×10^{38}erg/s, $Z/Z_\odot = 0.01$, $\chi^2 = 112$ for 86 degrees of freedom).

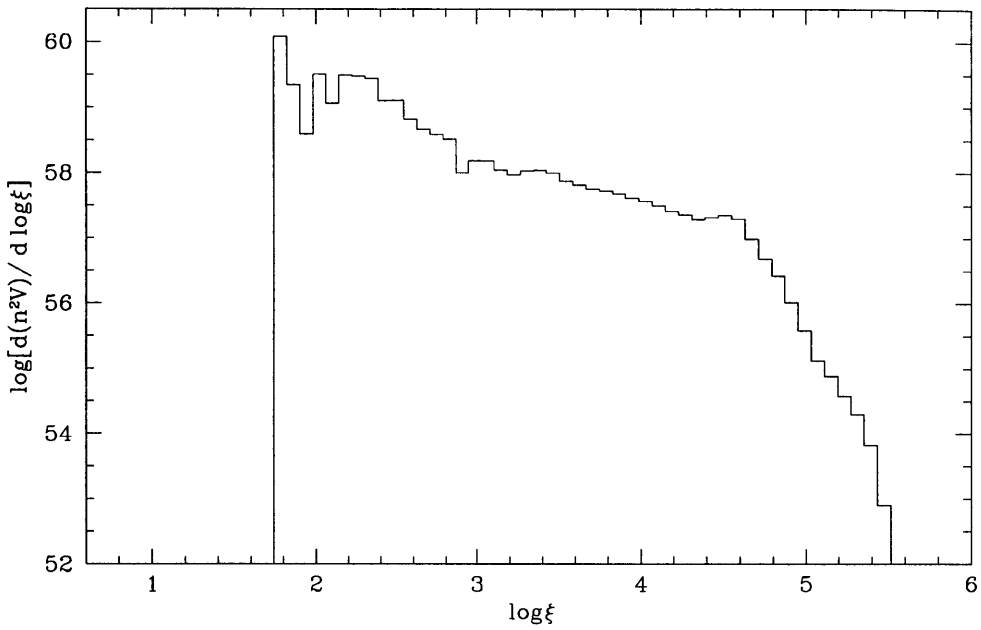

Figure 8-13: The Differential emission measure of the hydrodynamically simulated wind for an luminosity equal to 6×10^{38} erg/s.

abundances. The presence of gas with $1 < \log \xi < 3$ produces strong recombination emission which drives the abundance to very low values. While the neglect in the algorithm of absorption between the X-ray source and the reprocessing point may have caused an overestimate of the recombination emission by a factor of a few, the total emission measure of material with $2 < \log \xi < 3$ in the Blondin & Woo (1995) model is 1.33×10^{59} cm^{-3} compared to the lower limit of 9×10^{57} cm^{-3} for single components with $\log \xi$ in that range derived in the previous Section (Figure 8-9). The lack of a silicon emission feature in the model can be explained by the absence of material at low ionization. The presence of the silicon fluorescence feature in the observed spectrum indicates that there exists gas in the wind of SMC X-1 that is more dense than any of the gas in the hydrodynamic simulations. A hydrodynamic simulation with higher spatial resolution might resolve the gas distribution into smaller, denser clumps and move the peak of the emission measure distribution below 1 where it would fluoresce but not emit recombination radiation in the *ASCA* band.

8.3.2 Absorption of the Direct Radiation

By examination of the density distribution of Figure 2-1, it can be seen that the largest column densities occur in dense clumps. Since the densest material has the lowest ionization parameter and material at lower ionization has greater opacity, the effects of absorption of the direct radiation from the source should be most important in the densest clumps. The contour denoting the highest density in Figure 2-1 denotes a density of 10^{12} cm^{-3}. To explore the importance of absorption at the largest densities encountered in that distribution, XSTAR runs were conducted with densities equal to 10^{12} cm^{-3} and X-ray luminosities equal to 6.4×10^{38} ergs/s. The distance from the neutron star to the first clump of this density is 13 pixels which is equal to 1.86×10^{12} cm which implies $\log \xi = 2.26$. Two XSTAR runs were made with these parameters.

In the first run, a column density of 7.15×10^{23} cm^{-2}, equivalent to a path length of 7.15×10^{11} cm was used. The spectrum of reprocessed radiation from the last zone, which had $\log \xi = 1.98$, is plotted in Figure 8-14 along with the spectrum of reprocessed radiation computed in the optically thin XSTAR run for $\log \xi = 1.98$. The effect of absorption can be seen here. In the second run, a column density of 1.0×10^{23} cm^{-2}, equivalent to a path length of 1.0×10^{11} cm was used. The spectrum of reprocessed radiation from the last zone, which had $\log \xi = 2.22$, is plotted in Figure 8-15 along with the spectrum of reprocessed radiation computed in the optically thin XSTAR run for $\log \xi = 2.22$. This spectrum, in contrast, is almost completely unaffected by the presence of the absorbing material in between. Though the absorbing column is one-seventh of that in the first run, this spectrum shows the effect of very much less than one-seventh of the absorption of the first spectrum. The reason for this is that in the first run, an ionization front like those in the simulations of Kallman & McCray (1982) formed at a point in the matter such that the column density was approximately 2×10^{23} cm^{-2}. Inside of the ionization front, hydrogen was mostly ionized and the heavy elements were at high stages of ionization. Outside of the ionization front, hydrogen had recombined and the heavy elements were at lower stages of ionization. Therefore, the opacity was very low before the ionization front and very large after the ionization front.

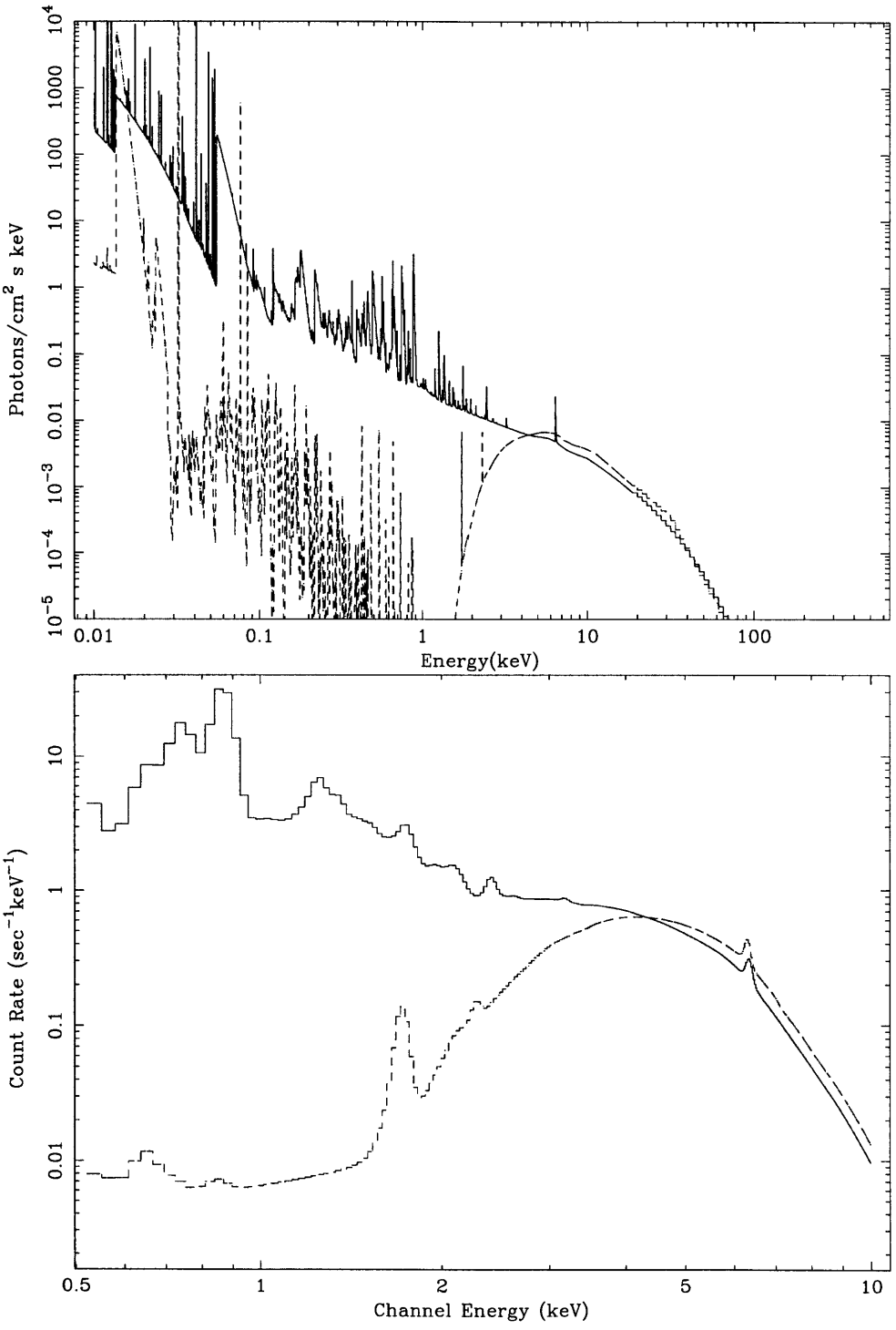

Figure 8-14: The spectrum of reprocessed radiation at $\log \xi = 1.98$ with an absorbing column of 7.15×10^{23} cm^{-2} between the radiation source and the reprocessing site (dashed line), and the spectrum of reprocessed radiation for $\log \xi = 1.98$ from the optically thin run (solid line). In the top panel is output from XSTAR and in the bottom panel are the spectra convolved with the *ASCA* SIS response is in the panel.

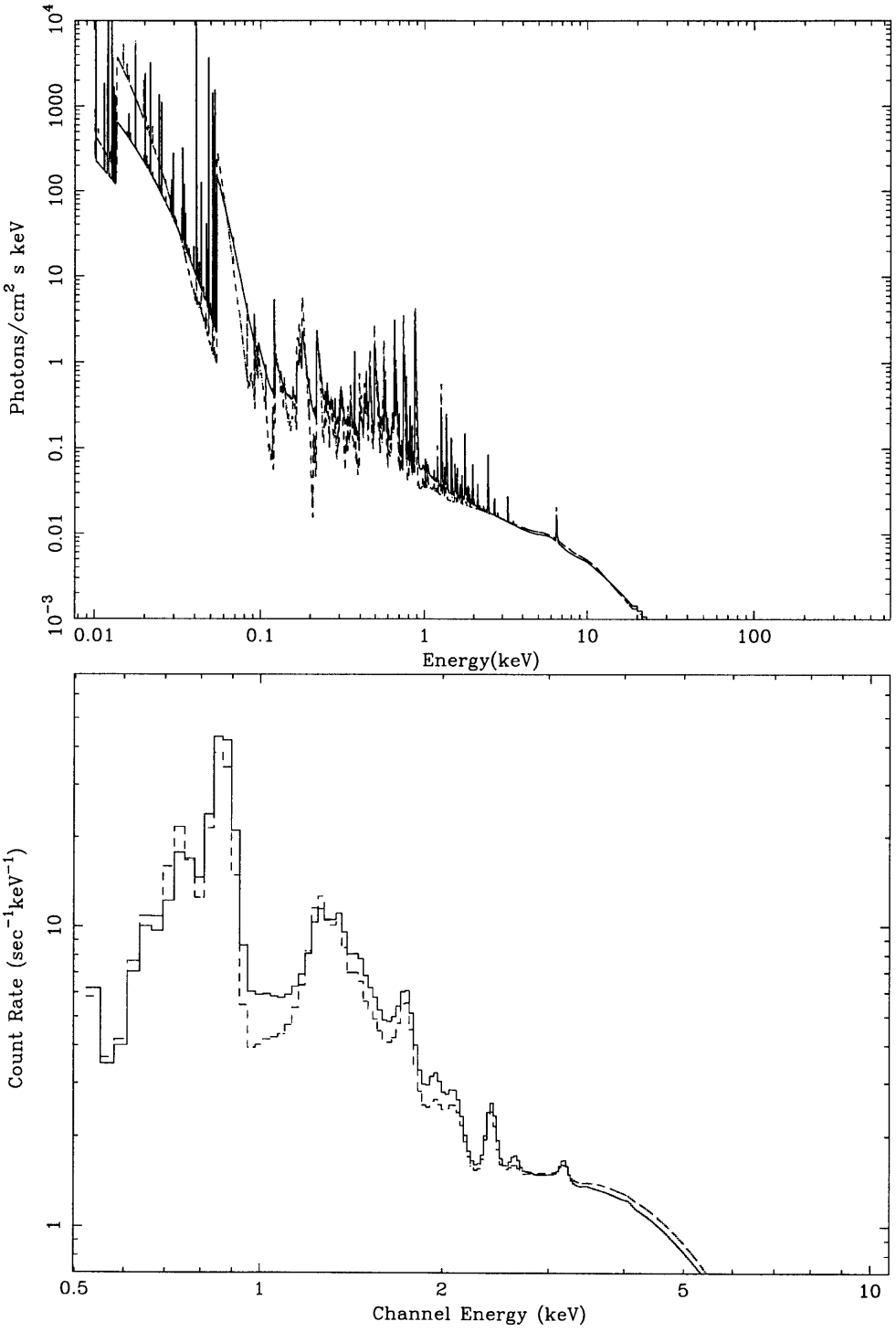

Figure 8-15: The spectrum of reprocessed radiation at $\log \xi = 2.22$ with an absorbing column of 1.0×10^{23} cm^{-2} between the radiation source and the reprocessing site (dashed line), and the spectrum of reprocessed radiation for $\log \xi = 2.22$ from the optically thin run (solid line). In the top panel is output from XSTAR and in the bottom panel are the spectra convolved with the *ASCA* SIS response is in the panel.

These calculations show that for column depth less than 2×10^{23} cm^{-2}, ignoring absorption along the paths from the radiation source to the reprocessing sites is a good approximation. Of the paths which begin at the neutron star, only those which go through the largest, densest clumps have column densities of this magnitude and therefore the error due to the unaccounted for absorption is small. Furthermore, for columns much larger than 2×10^{23}, the effect on the spectrum of reprocessed radiation is that all radiation less than a few keV is absorbed and so inclusion of absorption will not change the spectrum of reprocessed radiation to that of the pure Thompson scattered appearance of the observed eclipse spectrum of SMC X-1.

8.3.3 Spherically Symmetric Winds

A spherically symmetric power-law wind distribution of the type derived by Castor, et al. (1975) provides another model to test against the observed spectrum. These models have several free parameters (as seen in Chapter 2) and so rather than run the spectral simulation on a wind model given by one set of parameter values or on a number of models derived from a grid in parameter value space, a discussion of what parameter values might reproduce the observed eclipse spectrum is given.

In this theory, at distances from the star much greater than the stellar radius, the wind velocity approaches its asymptotic velocity (v_∞) and the density becomes nearly proportional to r^{-2}. Therefore, if the X-ray source is not far from the star compared to the bulk of the wind material, the ionization parameter is nearly constant over a large part of the wind (Figure 8-16). To estimate the intensity of the reprocessed radiation, which is mostly due to Thompson scattered radiation, the wind may be approximated to have a density distribution centered on the X-ray source, in which case the ionization parameter has exactly the same value (ξ_0) everywhere and the density may be written as:

$$n(r) = \frac{L}{\xi_0 r^2} \text{erg}^{-1}\text{s cm}^{-1} \tag{8.4}$$

To account for the observed eclipse flux, the relationship for the spectral normalization

obtained above ($K\xi = 1.7$) must be satisfied.

$$K = \frac{1}{4\pi D^2} \int n^2 dV \times 10^{-14} \mathrm{erg}^{-2}\mathrm{s}^2\mathrm{cm}^{-2} \tag{8.5}$$

and using Equation 8.4,

$$\begin{aligned} K &= 10^{-14}(4\pi D^2)^{-1} \int_{R_*}^{\infty} n^2 dV \mathrm{erg}^{-2}\mathrm{s}^2\mathrm{cm}^{-2} \\ &= 10^{-14}(4\pi D^2)^{-1} \xi_0^{-2} L^2 \int_{R_*}^{\infty} r^{-4} 4\pi r^2 dr \, \mathrm{erg}^{-2}\mathrm{s}^2\mathrm{cm}^{-2} \qquad (8.6) \\ &= 10^{-14} D^{-2} \xi_0^{-2} L^2 {R_*}^{-1} \mathrm{erg}^{-2}\mathrm{s}^2\mathrm{cm}^{-2} \qquad (8.7) \end{aligned}$$

Then $K\xi_0 = 1.7$ implies

$$\xi_0 = 3.2 \times 10^3 \left(\frac{D}{50\,\mathrm{kpc}}\right)^{-2} \left(\frac{L}{10^{38}\mathrm{erg/s}}\right)^{2} \left(\frac{R_*}{10^{12}\mathrm{cm}}\right)^{-1} \tag{8.8}$$

or less if only part of the flux is due to the extended wind. The approximation of a density distribution proportional to r^{-2} wind is equivalent to the approximation of a constant velocity wind. The density in this type of wind is related to the mass loss rate ($\dot{M}$) and this asymptotic velocity (v_∞) by:

$$n(r) = \frac{\dot{M}}{4\pi r^2 v_\infty \mu} \tag{8.9}$$

where μ is the gas mass per hydrogen atom ($\sim 1.34 m_H$), also known as the mean molecular weight. Substituting this expression for the density with that of Equation 8.4, the ionization parameter of the wind is

$$\begin{aligned} \xi_0 &= 4\pi L \mu v_\infty / \dot{M} \, \mathrm{erg}^{-1}\mathrm{s}\,\mathrm{cm}^{-1} \qquad (8.10) \\ &= 4.5 \times 10^3 \left(\frac{L}{10^{38}\mathrm{erg/s}}\right) \left(\frac{\dot{M}}{10^{-6} M_\odot/yr}\right) \left(\frac{v_\infty}{10^3 \mathrm{km/s}}\right) \qquad (8.11) \end{aligned}$$

So for $\log \xi \sim 4$, wind parameters of typical B-type stars (10^{-7}–$10^{-6} \dot{M}_\odot$/yr, $v_t \sim 1500$ km/s) can be accommodated.

Although a power-law type wind can produce Thompson scattered radiation in an

amount that can provide a global fit to the observed eclipse spectrum, a power-law type wind with $\log \xi > 3$ cannot produce the silicon emission feature. A component with $\log \xi < 1$ is necessary. An exponential atmosphere observed by absorption in eclipse transitions may be a good candidate for this low ionization region. An atmosphere with a scale height much less than the stellar radius would be illuminated and visible in only a small region. This region has the same distance from the compact object as does the center of the neutron star (1.95×10^{12}cm for SMC X-1). For this region to have $\log \xi < 1$, a density of approximately 10^{14} cm^{-3} is required for an X-ray luminosity of 5×10^{38} erg/s. Woo (1993) fit *Ginga* spectra during eclipse transitions to absorption by hybrid models. At the minimum radius of illumination and visibility, these models have densities no greater than 5×10^{12} cm^{-3}. At the stellar surface these models have densities no greater than 6×10^{13}cm^{-3}. However, only very near eclipse transitions can material at the stellar surface be both illuminated by the X-ray source and visible to the observer. The distribution of $\log \xi$ for the best fit parameters to one of the eclipse transitions is plotted in Figure 8-16 for an X-ray luminosity of 3×10^{38} erg/s. As for the Blondin & Woo (1995) hydrodynamic simulation, the *ASCA* spectrum requires more low-ionization (dense) material than spherically symmetric models contain.

8.4 *AXAF* Simulations

Simulations of a 40,000 second (about the duration of one eclipse) *AXAF* observation were done using the MARX *AXAF* simulation software. For each spectral model a simulation was done with the the High Energy Transmission Grating (HETG) assembly in place and one with the Low Energy Transmission Grating (LETG) in place. The HETG actually contains two sets of gratings — the Medium Energy Grating (MEG) and the High Energy Grating (HEG) — and the LETG contains only the Low Energy Grating (LEG). One set of simulations used a single zone spectral model with the lowest calculated value of the ionization parameter ($\log \xi = -2.95$, Figure 8-17) and one set of simulations used a $\log \xi = -2.95$ component and a component at

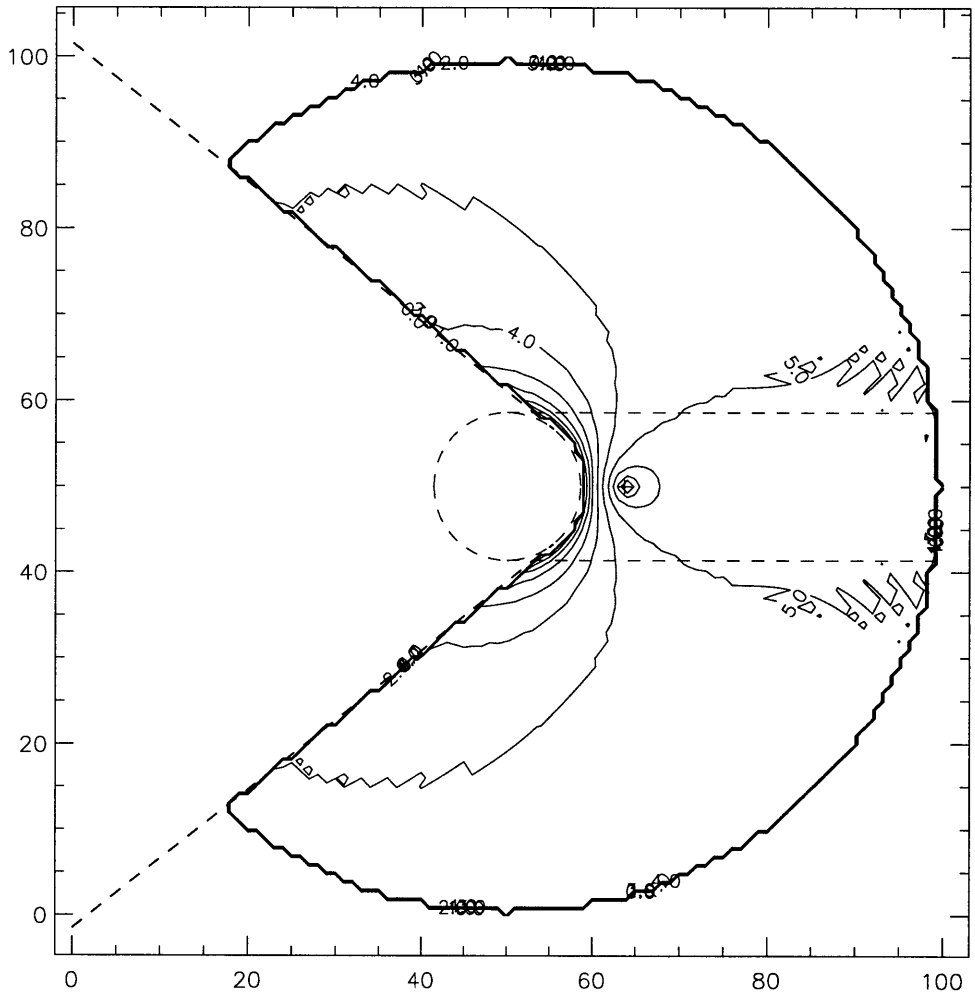

Figure 8-16: Contours of $\log \xi$ for a hybrid power-law wind. The ragged edges are an artifact.

$\log \xi = 1.8$ (Figure 8-18). The $\log \xi = 1.8$ component had the maximum normalization allowed by the *ASCA* data ($K = 3 \times 10^{-4}$, Figure 8-9). Due to the poor counting statistics, it does not appear that the high resolving power of the *AXAF* gratings will allow detection of recombination emission from SMC X-1 at a level which has not already been excluded with *ASCA*. However, they will allow the flux and energy of the silicon emission line to be better constrained. This would allow the nature of the dense, low-ionization regions to be better understood.

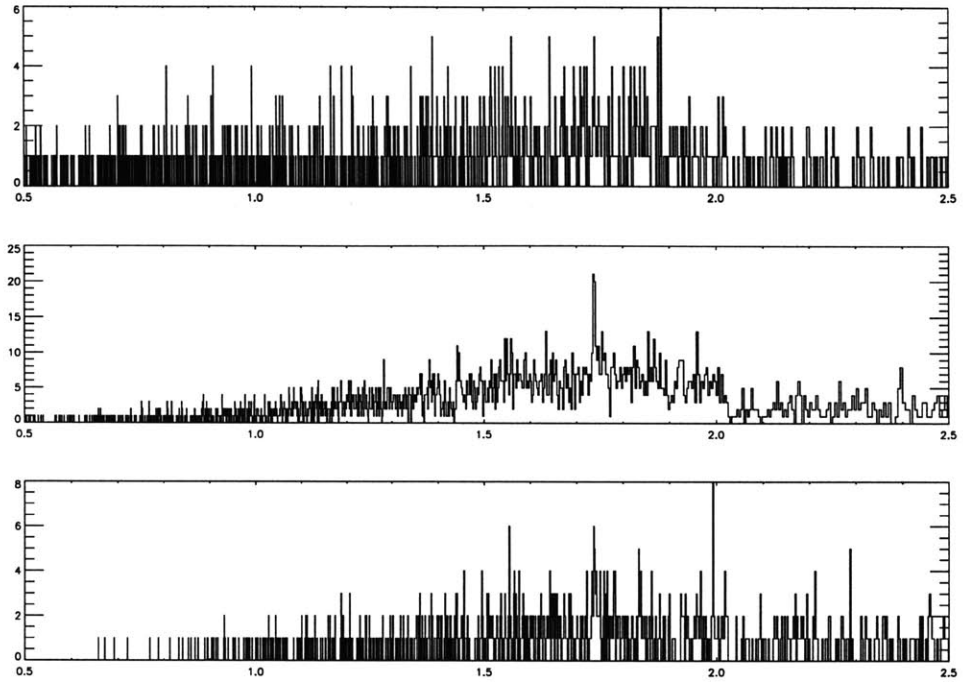

Figure 8-17: Simulations of 40,000 second observation of SMC X-1 with the spectrum of a single zone $\log \xi = -2.95$ model. The panels from top to bottom are the LEG, MEG, and HEG.

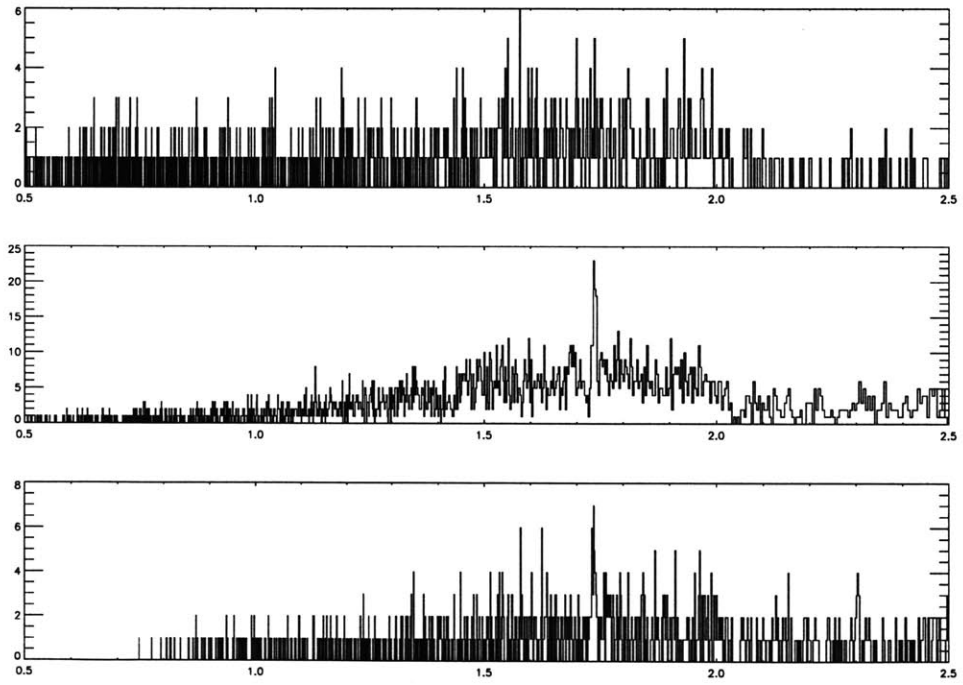

Figure 8-18: Simulations with a $\log \xi = -2.95$ component plus a $\log \xi = 1.8$ component.

Chapter 9

Summary

The conclusions of this work are listed here.

1. The *ASCA* SIS spectrum of SMC X-1 in eclipse has approximately the same form in eclipse as out of eclipse. This indicates that most of the X-ray reprocessing is due to Thompson scattering.

2. The lack of strong recombination features in the observed eclipse spectrum indicates that most of the gas in the wind of SMC X-1 is either very highly ionized ($\log \xi > 3$) or at very low ionization ($\log \xi < 1$) but there is very little material at intermediate ionization.

3. The presence of a small but significant silicon Kα fluorescence feature near the energy of the fluorescence line of neutral silicon (1.74 keV) is detected with a significance of 3σ. The presence of this emission line feature indicates that a significant amount of gas must have very low ionization though a better meausurement of this feature with a high resolution spectrometer such as on *AXAF* or *XMM* would be desirable. The magnitude of this feature indicates that the silicon abundance must be less than a few tenths of the solar value unless a large part of the spectrum is due to reprocessing in highly ionized gas.

4. The Blondin & Woo (1995) model of the density distribution derived by 3-D hydrodynamic simulation cannot reproduce the observed eclipse spectrum. It

contains a large amount of material with $1 < \log \xi < 3$. This material would produce a large flux of recobination radiation which does not appear in the *ASCA* spectra. Also, this model does not any material at low enough ionization to produce the observed silicon fluorescence line. A hydrodynamic simulation with higher spatial resolution might resolve smaller, denser clumps and produce an emission measure distribution which would reproduce the observed eclipse spectrum.

5. While a smooth, spherically symmetric wind could be highly ionized enough not to emit recombination radiation, it is difficult to construct such a wind, consistent with observations of X-ray eclipse transitions that would produce a silicon fluoresence line.

Appendix A

The ASCA Observatory

The Japanese observatory *ASCA* (Advanced Satellite for Cosmology and Astrophysics) (Tanaka et al. 1994) was launched in February of 1993. On board *ASCA* are four nested foil mirror X-ray telescopes (Serlemitsos et al. 1995). At the focal planes of two of these telescopes are X-ray CCD (charge coupled device) detectors, the Solid State Imaging Spectrometers (SIS) (Gendreau 1995). At the focal planes of the two other telescopes are proportional counter detectors, the Gas Imaging Spectrometers (GIS) (Ohashi et al. 1996). In this chapter, the properties and operation of the instruments are described in so far as they are relevant to the data and analysis in this thesis. In particular, no data from either of the GIS detectors is used in this work, so these are not described here.

A.1 The X-ray Telescopes

Each of the four X-ray telescopes on *ASCA* consists of two sets of 120 concentric conical aluminum foils. Each of the foils is coated with a reflecting surface of 10 to 20 microns of acrylic and 60 nm of gold. The foils are oriented so that X-rays strike the reflecting surface at grazing incidence, an angle of less than one degree between the reflecting surface and the path of the X-ray.

The focusing power of the X-ray telescopes is such that 50% of the X-rays with energies less than 12 keV from a point source near the center of the field of view is

focused onto a region in the focal plane with a diameter which corresponds to 3 arc minutes on the sky. For each telescope, the on-axis effective area varies from 325 cm^2 at 1 keV to 150 cm^2 at 6 keV. The focusing power of these telescopes is poor compared to that of X-ray telescopes on previously launched missions. For example, the *ROSAT* X-ray observatory focuses 50% of the flux into a diameter of 15 arc seconds. However, the X-ray telescopes on *ASCA* are unique in their capability to focus high energy X-rays. The *ROSAT* response drops off at 2.5 keV and the *Einstein* response drops off at 4 keV. Because X-rays only reflect at very sharp grazing angles, the response of the telescopes falls off quickly away from the optical axis. At 20′ from the optical axis, the telescope response is reduced by approximately a factor of three. Also, the point spread function becomes distorted away from the optical axis.

Even for unresolvable sources, focusing optics provide an advantage over the collimation techniques of other X-ray observatories in the rejection and subtraction of background. A collimated detector does not determine from where in its field of view (typically about a degree in diameter) X-rays come from. Thus, focusing optics allow the diffuse cosmic X-ray background as well as X-rays from any nearby sources, to be accurately separated in analysis. Also, focusing optics collect X-rays incident from over a large area and deposit them onto a small detector region — with *ASCA*, X-rays from a few hundred square centimeters of collecting area are focused on to a few square millimeters of detector — which greatly reduces the background from cosmic rays. In collimated detectors, the effective collecting area can be no larger than the geometrical detector area. Furthermore, in an imaging detector, the detector pixels away from the source's point spread provide a contemporaneous estimate of the background within the point spread.

A.2 The Solid State Imaging Spectrometers

Each of the two SIS detectors on *ASCA* (designated "SIS0" and "SIS1") consists of 4 adjacent 420×422 pixel X-ray CCDs arranged in a square. The *ASCA* observatory was the first X-ray observatory to employ CCD detectors, and these detectors are

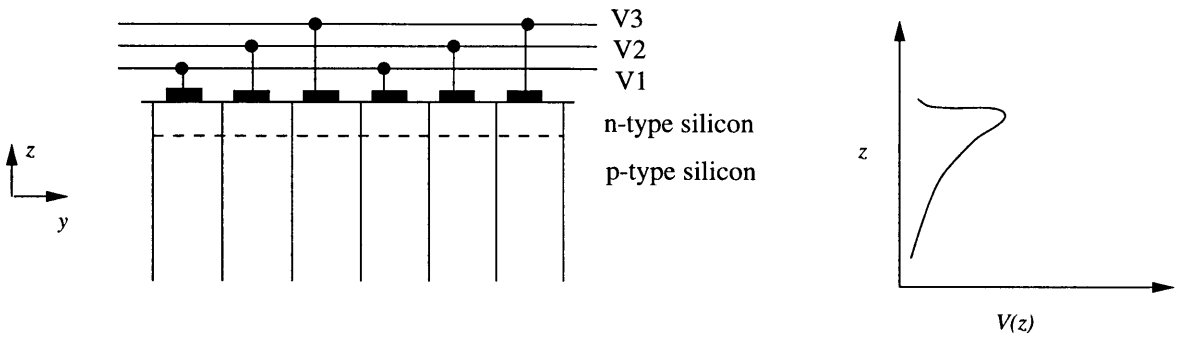

Figure A-1: The left panel is a schematic cross-section of 2 CCD pixels in the y-z plane showing the three phases in each pixel. The right panel is a schematic graph of the electrostatic potential along the z direction. The p-n junction creates a local maximum in the potential which confines conduction electrons in the n-type silicon region.

responsible for the superior energy resolution, relative to previous missions, possible with *ASCA*. For this reason, the theory of operation of X-ray CCDs, especially as it relates to the energy resolution is presented here in some detail.

A.2.1 Theory of Operation

A CCD consists of a two-dimensional array of pixels. In this description, the directions along the pixels will be referred to here as the x and y directions while the direction normal to the CCD array will be referred to as the z direction. Each pixel consists of three (in the case of the *ASCA* SIS) phases which are aligned linearly along the y direction (which, for reasons described below, is known as the clocking direction). A gate structure of deposited layers of conducting polysilicon and insulating silicon dioxide allows an independent bias voltage to be applied to each phase.

In Figure A-1, the structure of the CCD in the y-z plane is shown schematically for two pixels along with the potential along the z direction. X-rays are focused onto the CCD in the downward z direction. Those with energies greater than a few hundred eV penetrate the optical/UV light shields in front of the detector as well as the gate structure on top of the CCD. The reduced detection efficiency for low energy X-rays causes the effective area of one XRT+SIS to peak near 200 cm^2 at approximately 1.5 keV though the effective area of the XRT continues to increase towards lower

energy. If an X-ray arrives at the silicon layers, it may be absorbed by a silicon atom resulting in the ionization of an inner shell electron. This electron is highly energetic and ionizes other silicon atoms as it slows. On average, one conduction electron per 3.65 eV of X-ray photon energy is produced. The variance in the number of conduction electrons produced by an X-ray of a given energy is equal to the mean number multiplied by an empirical "Fano factor", which for silicon is approximately 0.1. That is, the probability distribution for the number of conduction electrons produced resembles a Poisson distribution but with a smaller variance.

The *p*-*n* junction, even with no bias voltage applied, causes a local maximum in the electrostatic potential — a potential energy minimum for electrons — near the junction. The volume of the *p*-type silicon into which the potential gradient extends is known as the depleted region because the potential gradient removes conduction electrons and holes from this volume. If the X-ray interacts within this volume, the conduction electrons migrate in the z direction to the potential minimum near the *p*-*n* junction. The extent of the depletion region into the *p*-type layer, the "depletion depth" — about 30μ in the SIS, is highly sensitive to the amount of doping in the silicon, and determines the sensitivity of the detector to high-energy photons, which penetrate deep into the silicon. The conduction electrons are confined in the x direction by "channel stops", insulators which prevent transfer of charge between the rows of pixels. In the y direction, the electrons are confined by adjusting the phase voltages (V1, V2, V3 in Figure A-1) so that the potential minimum in one of the phases is higher than its neighbors and so electrons do not enter that phase.

An X-ray CCD is exposed for a time that, preferably, is short enough so that it is unlikely that more than one X-ray will land on any one pixel. When multiple X-rays land on a pixel during a single exposure, each produces a number of conduction electrons proportional to its energy and the result is indistinguishable from a single electron with energy equal to the sum of the individual X-rays. This phenomenon is known as "pile up" and can limit the observability of bright sources with CCD detectors.

After an exposure is completed, the charge is "clocked" in the y direction. In

clocking, the phase voltages are varied up and down so that the electrons are moved from one phase to next, along the row of pixels to the edge of the array. In the SIS, the electrons are moved in a few milliseconds onto a "frame store array" which has the same number of pixels in both dimensions as the "imaging array" but is shielded from X-rays. In the few seconds that the imaging array undergoes another exposure, the charge packets are moved from the frame store chip, row by row, onto a single row of pixels called the output register. One by one, the packets of charge from the output register are moved onto an output node which acts like a capacitor. The charge placed on the output node produces a voltage which is then amplified and processed through analog-to-digital electronics to the on-board data system. A few electrons in each of the charge packets may be gained or lost in this process and this read-out noise is the other most important limit in the ability of an X-ray CCD to measure X-ray energies precisely. The use of a frame store array allows the charge packets to be read slowly over an exposure time which minimizes the read out noise. The read-out noise for the *ASCA* SIS is about 5 electrons.

The expression for the full-width half-maximum spectral resolution for a CCD detector is then

$$\Delta E = 2.35 \times 3.65\text{eV}\sqrt{\text{RON}^2 + F\left(\frac{E}{3.65\text{eV}}\right)^2} \tag{A.1}$$

where RON is the read-out noise and F is the Fano factor. The spectral resolution of the SIS has degraded with time in a way that can be described as a secular increase in the Fano factor. A plot from the *ASCA* technical manual showing the energy resolution of the SIS for various times is reproduced here as figure A-2.

When an X-ray interacts on the silicon of a CCD, conduction electrons may be produced not only on a single pixel but also into a few nearby pixels. This is especially true for high energy X-rays which produce a larger charge cloud. Therefore, when a single pixel has a signal larger than a certain "event threshold", the 3×3 pixel area around it is checked to see if any of those pixels have a signal larger than a smaller "split event threshold" and the events are classified according to the pattern of pixels

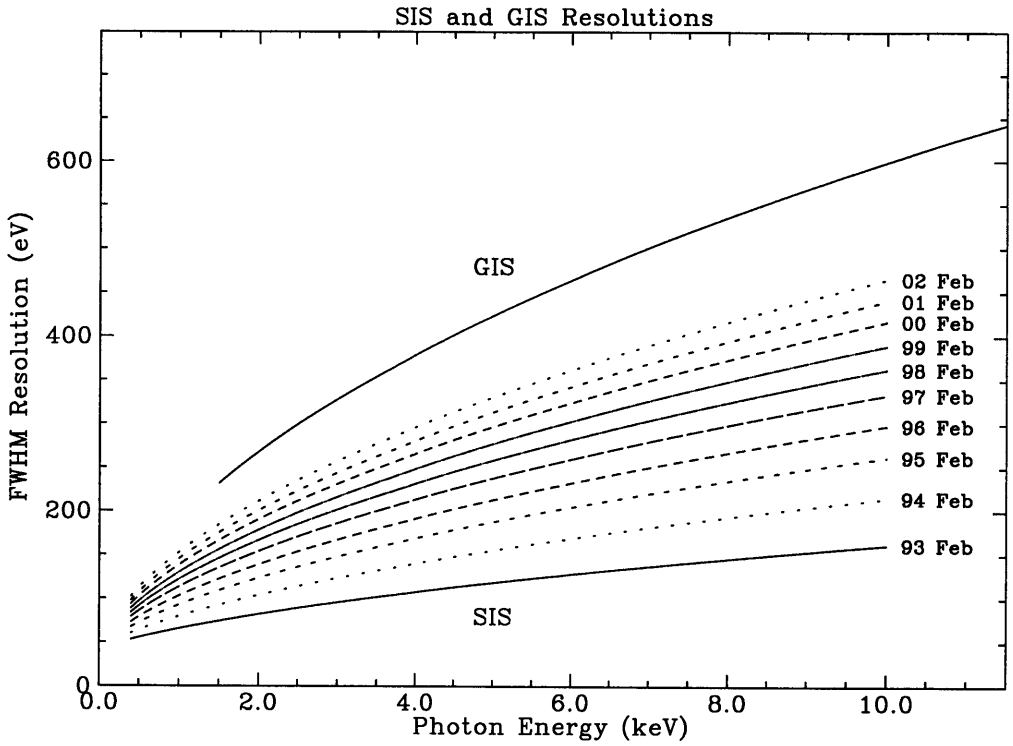

Figure A-2: The energy resolution of the SIS for various times for the observed secular increase in the Fano factor.

with significant charge. Cosmic rays tend to produce charge in several adjacent pixels. Also, some high-energy X-rays interact past the depleted region and only a fraction of the electrons fall into the potential well. These events, which are also considered to be background because their X-ray energies are not resolved, also tend to produce charge in several adjacent pixels. So while including split events increases the sensitivity to high energy X-rays, it also increases the unrejected background. Typically, one includes grade "0" — single pixel events — as well as grade "2", "3", and "4" events — in which one of the four adjacent pixels exceeds the split event threshold. The signal from the adjacent pixel is summed with the central pixel in order to obtain the X-ray energy.

Incident photons with energies greater than 1.84 keV may ionize K-shell electrons from the silicon in the detector. As described in Chapter 6, a 1.74 keV Kα photon may be produced as the K-shell vacancy is filled. This Kα photon may escape into another pixel or into an inactive region of the detector resulting in a measured energy less than

that of the incident electron by 1.74 keV — these events are known as "escape events". The fluorescence photon may also be detected separately from the incident photon resulting in spurious 1.74 keV events — these are known as "fluorescence events". Escape photons occur with a probability of approximately 2% while fluorescence events occur with a probability somewhat less than 1% relative to detection near the actual energy. For a continuum source, the effect of escape events is not generally noticeable but an underestimate of the probability of fluorescence events may result in spurious detection of a Kα emission line.

The *ASCA* observatory, like most orbiting X-ray observatories, can easily generate more useful data than can be telemetered to the ground. For this reason, significant data processing occurs on board the spacecraft. For example, rather than sending to the ground the signal from every pixel of every exposure, all but the signals from the 3×3 areas in which events occur are discarded. In the "bright" observing mode, the total pulse height is computed on board the spacecraft and only this total pulse height is telemetered. In the "faint" observing mode, the pulse height from each of the nine pixels is telemetered and event classification and the signal summation occurs off-line.

A.3 Data Screening

To reduce the background from the various sources, data taken during times of high background and event types which are likely to be background are rejected off-line. The standard screening criteria are listed below. The default parameter values suggested by the *ASCA* Guest Observer Facility are as follows:

- bright earth angle — from the spacecraft, the angle between the day side of the earth and the source. A light leak on the SIS detectors allows contamination from UV and optical photons when the instruments are pointed near the bright earth. The standard criterion rejects SIS0 data taken when this angle is less than 30° and SIS1 data taken when this angle is less than 20° (the light leak is slightly worse in SIS0).

- elevation angle — from the spacecraft, the angle between the earth (day or night side) and the source. At low elevation angle, sources are viewed through the earth's outer atmosphere which may scatter and absorb X-rays. Furthermore, the detectors operate while the source is occulted by the earth and those data are rejected through this criterion. The standard criterion rejects data taken when this angle is less than 10°.

- cut off rigidity — a function of position in the earth's magnetic field which describes the minimum momentum of a cosmic ray capable of penetrating to that point. The standard criterion rejects data taken when the spacecraft is at a position such that the cut off rigidity is greater than 6 GeV/c.

- radiation belt monitor — the count rate in a small PIN diode sensitive to cosmic rays. The standard criterion rejects data taken when this count rate was greater than 275 counts/s.

- events above threshold — the number of events detected in a single CCD exposure frame. If a large number of apparent X-ray events are detected in a single frame, it is likely that the CCDs are detecting UV and optical light rather than X-rays. The standard criterion rejects frames with more than 100 events.

- event grade — the event grade as explained in Section A.2.1. In standard analysis, only events of grade 0, 2, 3, and 4 were retained.

Data from defective "hot" and "flickering" pixels, which produce many spurious events are also screened out by rejecting data from pixels with an unusually large number of events. The observation was done in a mixture of both the faint and bright modes. Rather than analyze these two data modes separately, we used data that had been converted from the faint mode to the bright mode using the same algorithms as are applied on board the spacecraft during bright mode observing.

Appendix B

C code for the Spectral Simulation

Included below are portions of the C code which formed the spectral simulation program of this work. The intention here is not to distribute working code but rather, to illustrate in detail the mechanics of the simulation algorithm.

From the XSTAR output, the bremsstrahlung continuum emissivity and the recombination continuum emissivity as a function of $\zeta \equiv \log \xi$ are read into the array `rccems`, the fluorescence and recombination line emissivities as a function of ζ are read into the array `rcem` and the opacities as a function of ζ are read into `opakc`. The line emission in `rcem` is added to the continuum in `rccems`. The emission in `rccems` is combined with the Thompson continuum to produce `emfxm` which is the emission function such that when `emfxn` is multiplied by n^2, the volume emissivity j_ν is obtained. The opacities are converted to a value which, when multiplied by n becomes the optical depth through a grid element.

The program loops over the three dimensions of the Cartesian grid moving along lines parallel to the line of sight. At each Cartesian grid point, the hydrogen atom density is determined by mapping from a spherical grid containing the mass densities. The `hunt` routine from Press et al. (1992) is used for table lookup. Emission is calculated from cells which are both visible to the observer during eclipse and illuminated by the compact X-ray source. Cells which are not illuminated by the compact X-ray source are assumed to have the lowest ionization parameter from the XSTAR table for purposes of calculating absorption through them. The variable `s` is used so that

where absorption occurs through several adjacent unilluminated cells, the absorption in each of the 5000 continuum energy bins is not computed in each cell. Instead, the column density is stored in s until the end of the unilluminated region is reached, then absorption is applied to each of the 5000 continuum energy bins.

```
#define XMAX 101  /* limits and origin of the cartesian grid */
#define YMAX 101
#define ZMAX  51
#define XORI  50
#define YORI  50
#define ZORI   0
#define EV_ANG        12398.54      /* wvlen (A) of a 1 eV photon */
#define M_PROTON      1.672e-24     /* Proton Mass  */
#define NCN   5000     /*continuum bins */
#define NNNL  3900     /*number of lines */
#define ZONES   100     /*number of zones (log xi values) in xstar table*/
#define LUM    1e38            /* Luminosity unit */

  int method,absorb,wind_model;
  float l_x,cak_psi,cak_beta,hyb_r1,hyb_h,cak_vratio;
  static float sph_rho[I_MAX][J_MAX][K_MAX];
  static float n_p[ZMAX][YMAX][XMAX], zeta[ZMAX][YMAX][XMAX];
  static float logn_p[ZMAX][YMAX][XMAX],comp_eff[ZMAX][YMAX][XMAX];
  static float comp_coef, r0, theta0, phi0;
  static float tab_zeta[ZONES],rccems[ZONES][NCN],opakc[ZONES][NCN];
  static float emfxn[ZONES][NCN],opfxn[ZONES][NCN];
  static float dem[ZONES],rcem[ZONES][NNNL],elin[NNNL];
  float epi[NCN],t[ZONES],xpx,xnx;
  float sum_rccems[NCN], row_sum_rccems[NCN];
  float dv, em, runit, unit_vol;
  float line_energy_ev, contin_bin_width_ev;
  float inc_cont[NCN], comp_cont[NCN], luminosity_e[NCN];
  float comp_frac,em_sum[ZONES],s;
  int i,j,k,ic,jc,kc,emission;
  int kz,m,n,xi_out_range_count;

  /* l_x = source luminosity in (10^38 ergs/sec)            */
  /* opfxn = optical depth function of a grid length (cm^3) */
  /* emfxn = emission function (cm^3*ergs/sec/erg)          */
  /* xpx= XSTAR proton density (/cm^3)                      */
  /* zeta=log(ionization parameter)                         */
  /* opakc=continuum opacities at XSTAR density (/cm)       */
  /* rccems= specific emissivities at XSTAR density( erg /cm**3 /s /erg)*/
  /* rcem=line emissivities at XSTAR density (/cm**3 /s)    */
  /* elin=line wavelengths (A)                              */
```

```
  /* epi=continuum energies (ev)                                  */
  /* runit = cartesian grid spacing in cm                         */
  /* unit_vol = volume of grid element runit^3                    */

  /* read XSTAR output */
  read_xstout(tab_zeta,t,&xpx,&xnx,opakc,rccems,rcem,elin,epi);

  /* add lines to XSTAR continuum */
  for(n=0;n<NNNL;n++) {        /* add lines to recomb contin */
    line_energy_ev=EV_ANG / elin[n];
    hunt(epi-1,NCN,line_energy_ev,&m);
    contin_bin_width_ev=epi[m]-epi[m-1];
    for(kz=0;kz<ZONES;kz++) {
      rccems[kz][m-1]+=rcem[kz][n]
*line_energy_ev/contin_bin_width_ev;
    }
  }

  /* calculate emission function (emfxn) for minimum  */
  /* computation get incident spectrum & add Compton  */
  ispec(inc_cont,epi);
  comp_coef=E_P*SIGMA_THOMP/4/PI;
  for(kz=0;kz<ZONES;kz++)
    for(m=0;m<NCN;m++) {
      emfxn[kz][m]=rccems[kz][m]/xpx/xpx;
      emfxn[kz][m]+=inc_cont[m]*pow(10.0,tab_zeta[kz])*comp_coef;
    }

  /* Compute properties of 3D grid */
  runit=r[I_MAX-1]/(ZMAX-1);
  unit_vol=runit*runit*runit;

  /*adjust opacity function for minimum */
  /*computation within spatial grid     */
  for(kz=0;kz<ZONES;kz++)
    for(m=0;m<NCN;m++)
      opfxn[kz][m]=opakc[kz][m]*runit/xpx;

  /* Add up and absorb spectra over entire grid */

  /* intialize some things */
  for(m=0;m<NCN;m++)
    sum_rccems[m]=0;
  for(kz=0;kz<ZONES;kz++)
    dem[kz]=0;
  /* now loop over the grid */
  for(kc=0;kc<ZMAX;kc++) {    /* loop over columns parallel */
    for(jc=0;jc<YMAX;jc++) {  /* to the line of sight       */
```

```
      for(m=0;m<NCN;m++)      /* initialize */
        row_sum_rccems[m]=0;
      emission=FALSE;
      s=0;

      for(ic=XMAX-1;ic>=0;ic--) { /* go along line of sight */
sph_conv(ic, jc, kc, &r0, &theta0, &phi0, runit);
hunt(r-1,I_MAX,r0,&i);          /* map the spherical coordinates */
hunt(theta-1,J_MAX,theta0,&j);  /* (r[i],theta[j],phi[k] to the  */
hunt(phi-1,K_MAX,phi0,&k);      /* rectilinear grid with spacing */
i--;j--;k--;                    /* runit indexed by (ic,jc,kc)   */

if( i<0 || i>=I_MAX-1 ) {   /* if outside the hydro simulation */
  n_p[kc][jc][ic]=NO_N;
  logn_p[kc][jc][ic]=NO_LOG_N;
  comp_eff[kc][jc][ic]=NO_COMP_EFF;
  zeta[kc][jc][ic]=NO_ZETA;
}

else {                    /* if inside the hydro simulation */
  n_p[kc][jc][ic]=sph_rho[i][j][k]*P_M/M_PROTON;
  logn_p[kc][jc][ic]=log10(n_p[kc][jc][ic]);

  if(illuminated(kc,jc,ic,runit)) {  /* if illuminated */
    if(s>0) {   /* apply absorption through any previous dark path */
      if(absorb)
for(m=0;m<NCN;m++)
  row_sum_rccems[m]*=exp(-opakc[kz][ZONES-1]*s);
      s=0;
    }
    zeta[kc][jc][ic]=           /* compute quantities */
      log10(l_x/n_p[kc][jc][ic]/dist_sq(kc,jc,ic,runit))
      +log10(LUM);
    comp_eff[kc][jc][ic]=sqr(n_p[kc][jc][ic])
      *pow(10.0,zeta[kc][jc][ic]);

    if (visible(kc,jc,ic,runit)) {
      emission=TRUE;
      hunt(tab_zeta-1,ZONES,zeta[kc][jc][ic],&kz);
      if(kz==0 || kz==ZONES) { /*if ouside of tabulated zeta range*/
xi_out_range_count++;
printf("Zeta=%f (out of range) in cell ic=%i jc=%i kc=%i.\n"
       ,zeta[kc][jc][ic],ic,jc,kc);
      }
      if(!kz==0) kz--;
      dem[kz]+=sqr(n_p[kc][jc][ic]/xpx);  /* diff emis measure */
      for(m=0;m<NCN;m++) {      /* absorb & accumulate spectra */
```

```
if(absorb)
  row_sum_rccems[m]
    *=exp(-opfxn[kz][m]*n_p[kc][jc][ic]);
row_sum_rccems[m]+= emfxn[kz][m]*sqr(n_p[kc][jc][ic]);
      }
    }
  }
  else {          /* if not illuminated */
    if(emission)
      s+=n_p[kc][jc][ic];
    comp_eff[kc][jc][ic]=NO_COMP_EFF;
    zeta[kc][jc][ic]=NO_ZETA;
  }
}
      }
      if(s>0) {   /* apply absorption through any previous dark path */
if(absorb)
  for(m=0;m<NCN;m++)
    row_sum_rccems[m]*=exp(-opfxn[kz][ZONES-1]*s);
s=0;
      }
      if(emission) for(m=0;m<NCN;m++)
sum_rccems[m]+=row_sum_rccems[m];
    }
  }
  if(xi_out_range_count>0)
    printf("Xi out of tabulated range in %i cells.\n",xi_out_range_count);

  for (m=0;m<NCN;m++)            /* Normalize total spectrum: result is */
    sum_rccems[m]/=LUM/unit_vol; /* in 10^38 ergs/s/erg                 */
```

Bibliography

Abbott, D. C., 1982, *ApJ*, **259**, 282

Anders, E. & N., G., 1989, *Geochimica et Cosmochimica Acta* **53**, 197

Angelini, L., White, N. E., & Stella, L., 1991, *ApJ*, **371**, 332

Arnaud, K. A., 1995, *The File Format for XSPEC Table Models*, Office of Guest Investigator Programs Memo OGIP/92-009, NASA Goddard Space Flight Center Laboratory for High Energy Astrophysics

Arnaud, K. A., 1996, in G. Jacoby & J. Barnes (eds.), *Astronomical Data Analysis Software and Systems V*, Vol. 101, p. 17, ASP Conf. Series

Aschenbach, B., 1988, Appl. Opt. **27**, 1404

Becker, R. H., Pravdo, S. H., Rothschild, R. E., Boldt, E. A., Holt, S. S., Serlemitsos, P. J., & Swank, J. H., 1978, *ApJ*, **221**, 912

Blondin, J. M., 1994, *ApJ*, **435**, 756

Blondin, J. M. & Woo, J. W., 1995, *ApJ*, **445**, 889

Bonnet-Bidaud, J. M. & Van Der Klis, M., 1981, *A&A*, **97**, 134

Buff, J. & McCray, R., 1974, *ApJ*, **189**, 147

Castor, J. I., Abbott, D. C., & Klein, R. I., 1975, *ApJ*, **195**, 157

Clark, G. W., Minato, J. R., & Mi, G., 1988, *ApJ*, **324**, 974

Clark, G. W., Remillard, R. A., & Woo, J. W., 1997, *ApJ*, **474**, L111

Cooke, B. A. e., 1978, *MNRAS*, **182**, 489

Davidson, K. & Netzer, H., 1979, *Rev. Mod. Phys.* **51**, 715

Davison, P. J. N., 1977, *MNRAS*, **179**, 15P

Day, C. S. R., Tennant, A. F., & Fabian, A. C., 1988, *MNRAS*, **231**, 69

Dickey, J. M. & Lockman, F. J., 1990, *ARA&A*, **28**, 215

Eggleton, P. P., 1983, *ApJ*, **268**, 368+

Ferland, G. J. & Rees, M. J., 1988, *ApJ*, **332**, 141

Fishman, G. J. e. a., 1994, *ApJS*, **92**, 229

Gendreau, Keith, C., 1995, *Ph.D. thesis*, Massachusetts Institute of Technology

Gerend, D. & Boynton, P. E., 1976, *ApJ*, **209**, 562

Giacconi, R., Gursky, H., Kellogg, E., Schreier, E., & Tananbaum, H., 1971, *ApJ*, **167**, L67

Gruber, D. E. & Rothschild, R. E., 1984, *ApJ*, **283**, 546

Hammerschlag-Hensberg, G., Kallman, T. R., & Howarth, I. D., 1984, *ApJ*, **283**, 249

Harmon, B. A., e. a., 1992, in AIP Conf. Proc. 280, Compton Gamma-Ray Observatory, ed. M. Friedlander,N. Gehrels, & D. J. Macomb, p. 314, St. Louis, MO

Hatchett, S., Buff, J., & McCray, R., 1976, *ApJ*, **206**, 847

Hatchett, S. & McCray, R., 1977, *ApJ*, **211**, 552

Hayashida, K., Inoue, H., Koyama, K., Awaki, H., & Takano, S., 1989, *PASJ*, **41**, 373

Heemskerk, M. H. M. & Van Paradijs, J., 1989, *A&A*, **223**, 154

Howarth, I. D., 1982, *MNRAS*, **198**, 289

Hutchings, J. B., Crampton, D., Cowley, A. P., & Osmer, P. S., 1977, *ApJ*, **217**, 186

Ilovaisky, S. A., Chevalier, C., Motch, C., Pakull, M., Van Paradijs, J., & Lub, J., 1984, *A&A*, **140**, 251

Iping, R. C. & Petterson, J. A., 1990, *A&A*, **239**, 221

Jahoda, K., Swank, J. H., Giles, A. B., Stark, M. J., Strohmayer, T., Zhang, W., & Morgan, E., 1996, in EUV, X-ray and Gamma-ray Instrumentation for X-ray Astronomy VII, ed. O. H. W. Siegmund and M. A. Grummin, SPIE, 2808, 59

Kahabka, P. & Pietsch, W., 1996, *A&A*, **312**, 919

Kallman, T. R. & McCray, R., 1982, *ApJS*, **50**, 263

Katz, J. I., 1973, Nature Phys. Sci. **246**, 87

Khruzina, T. & Cherepashchuk, A., 1987, *Soviet Astronomy* **31**, 180

Kudritzki, R. P., Pauldrach, A., Puls, J., & Abbott, D. C., 1989, *A&A*, **219**, 205

Leahy, D. A., Darbro, W., Elsner, R. F., Weisskopf, M. C., Kahn, S., Sutherland, P. G., & Grindlay, J. E., 1983, *ApJ*, **266**, 160

Leong, C., Kellogg, E., Gursky, H., Tannanbaum, H., & Giacconni, R., 1971, *ApJ*, **170**, L67

Levine, A., Rappaport, S., Deeter, J. E., Boynton, P. E., & Nagase, F., 1993, *ApJ*, **410**, 328

Levine, A. M., Bradt, H., Cui, W., Jernigan, J. G., Morgan, E. H., Remillard, R., Shirey, R. E., & Smith, D. A., 1996, *ApJ*, **469**, L33

Levine, A. M. & Jernigan, J. G., 1982, *ApJ*, **262**, 294

Lewis, W., Rappaport, S., Levine, A., & Nagase, F., 1992, *ApJ*, **389**, 665

Liller, W., 1973, *ApJ*, **184**, L37

Lucke, R., Yentis, D., Friedman, H., Fritz, G., & Shulman, S., 1976, *ApJ*, **206**, L25

Makino, F. & the ASTRO-C team, 1987, Ap. Lett. Comm. **25**, 223

Morrison, R. & McCammon, D., 1983, *ApJ*, **270**, 119

Morton, C. D., 1967, *ApJ*, **150**, 535

Nagase, F., Zylstra, G., Sonobe, T., Kotani, T., Inoue, H., & Woo, J., 1994, *ApJ*, **436**, L1

Netzer, H., 1996, *ApJ*, **473**, 781

Ohashi, T., Ebisawa, K., Fukazawa, Y., Hiyoshi, K., Horii, M., Ikebe, Y., Ikeda, H., Inoue, H., Ishida, M., Ishisaki, Y., Ishizuka, T., Kamijo, S., Kaneda, H., Kohmura, Y., Makishima, K., Mihara, T., Tashiro, M., Murakami, T., Shoumura, R., Tanaka, Y., Ueda, Y., Taguchi, K., Tsuru, T., & Takeshima, T., 1996, *PASJ*, **48**, 157

Orr, A., Yaqoob, T., Parmar, A. N., Piro, L., White, N. E., & Grandi, P., 1998, *A&A*, **337**, 685

Osterbrock, D. E., 1989, *Astrophysics of Gaseous Nebulae and Active Galactic Nuclei*, University Science Books, Mill Valley, CA

Pagel, B. E. J. & Tautvaišienė, G., 1998, *MNRAS*, **299**, 535

Pauldrach, A., Puls, J., & Kudritzki, R. P., 1986, *A&A*, **164**, 86

Pfeffermann, E. e. a., 1987, SPIE **733**, 519

Press, W. H., Teukolsky, S. A., Vetterling, W. T., & Flannery, B. P., 1992, *Numerical Recipes in C, 2nd ed.*, Cambridge Universiy Press

Price, R. E., Groves, D. J., Rodrigues, R. M., Seward, F. D., Swift, C. D., & Toor, A., 1971, *ApJ*, **168**, L7

Priedhorsky, W. C. & Holt, S. S., 1987, Space Science Reviews **45**, 291

Primini, F., Rappaport, S., & Joss, P. C., 1977, *ApJ*, **217**, 543

Pringle, J. E., 1973, *Nature Phys. Sci.* **243**, 90

Pringle, J. E., 1996, *MNRAS*, **281**, 357

Reynolds, A. P., Hilditch, R. W., Bell, S. A., & Hill, G., 1993, *MNRAS*, **261**, 337

Rolleston, W., Dufton, P., Fitzsimmons, A., Howarth, I., & Irwin, M., 1993, *A&A*, **277**, 10

Russell, S. C. & Bessell, M. S., 1989, *ApJS*, **70**, 865

Russell, S. C. & Dopita, M. A., 1990, *ApJS*, **74**, 93

Sato, N., Hayakawa, S., Nagase, F., Masai, K., Dotani, T., Inoue, H., Makino, F., Makishima, K., & Ohashi, T., 1986, *PASJ*, **38**, 731

Schreier, E., Levinson, R., Gursky, H., Kellogg, E., Tananbaum, H., & Giacconni, R., 1972, *ApJ*, **172**, L79

Serlemitsos, P. J., Jalota, L., Soong, Y., Kunieda, H., Tawara, Y., Tsusaka, Y., Suzuki, H., Sakima, Y., Yamazaki, T., Yoshioka, H., Furuzawa, A., Yamashita, K., Awaki, H., Itoh, M., Ogasaka, Y., Honda, H., & Uchibori, Y., 1995, *PASJ*, **47**, 105

Stahle, C. K., Ebisawa, K., Kelley, R. L., Mukai, K., & White, N. E., 1997, in *ASCA Conference on X-ray Imaging and Spectroscopy of Cosmic Hot Plasmas*, p. 495

Stanimirovic, S., Staveley-Smith, L., Dickey, J. M., Sault, R. J., & Snowden, S. L., 1998, *MNRAS*, , accepted

Stromgren, B., 1939, *ApJ*, **89**, 529

Tanaka, Y., Inoue, H., & Holt, S. S., 1994, *PASJ*, **46**, L37

Tarter, C. B. & Salpeter, E. E., 1969, *ApJ*, **156**, 953

Tarter, C. B., Tucker, W. H., & Salpeter, E. E., 1969, *ApJ*, **156**, 943

Tjemkes, S. A., van Paradijs, J., & Zuiderwijk, E. J., 1986, *A&A*, **154**, 77

Toor, A. & Seward, F. D., 1974, *AJ*, **79**, 995

Trümper, J., 1983, Adv. Space Res. **2**, 241

Tuohy, I. R. & Rapley, C. G., 1975, *ApJ*, **198**, L69

Turner, M. J. L. e. a., 1989, *PASJ*, **41**, 345

van Paradijs, J. & Zuiderwijk, E., 1977, *A&A*, **61**, L19

Webster, B. L., Martin, W. L., Feast, M. W., & Andrews, P. J., 1972, Nature, Phys. Sci. **240**, 183

Westerlund, B., 1997, *The Magellanic Clouds*, Cambridge University Press

Whitlock, L. & Lochner, J. C., 1994, *ApJ*, **437**, 841

Woo, J. W., Clark, G. W., Blondin, J. M., Kallman, T. R., & Nagase, F., 1995a, *ApJ*, **445**, 896

Woo, J. W., Clark, G. W., & Levine, A. M., 1995b, *ApJ*, **449**, 880

Woo, Jonathan, W., 1993, *Ph.D. thesis*, Massachusetts Institute of Technology

Zhang, S. N., Robinson, C. R., Wilson, R. B., Harmon, B. A., Scott, D. M., & Remillard, R., 1996, *IAU Circ.* 6468